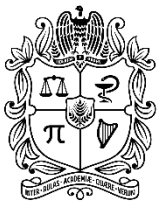

UNIVERSIDAD
NACIONAL
DE COLOMBIA

NANOPARTICLES ENHANCED SOLVENT DEASPHALTING (*e*-SDA) AND CATALYTIC CRACKING OXIDATION OF PITCH

Juan David Guzmán Calle

Universidad Nacional de Colombia
Facultad de Minas, Departamento de Procesos y Energía.
Medellín, Colombia
2020

NANOPARTICLES ENHANCED SOLVENT DEASPHALTING (*e*-SDA) AND CATALYTIC CRACKING OXIDATION OF PITCH

Juan David Guzmán Calle

Thesis presented as a partial requirement to qualify for the degree of:

Master's in engineering – Petroleum Engineering

Director:
Ph.D., M.Sc., Chemical Engineer, Farid Bernardo Cortés Correa.

Line of research:
Heavy and extra-heavy oil on-site upgrading
Research group:
Fenómenos de Superficie – Michael Polanyi

Universidad Nacional de Colombia
Facultad de Minas, Departamento de Procesos y Energía.
Medellín, Colombia
2020

Acknowledgments

To my supervisor Farid B. Cortés Correa and Professor Camilo Andrés Franco Ariza for their support, guidance and patience.

Special thanks to all the members of the research group Fenómenos de Superficie – Michael Polanyi, of the Facultad de Minas of Universidad Nacional de Colombia.

Special acknowledge to Ministerio de Ciencia Tecnología e Innovación (Minciencias), Fondo Nacional de Financiamiento para la Ciencia, la Tecnología y la Innovación, Fondo Francisco José de Caldas and Universidad Nacional de Colombia for their technical, and financial support provided by 017-2018 agreement.

To each person who supports and contributes to the development of this work.

Abstract

The energy landscape and the technical alternatives to supply the growing energy demand have made the oil and gas industry focus on heavy and extra-heavy oils. However, the production, transportation, and refining processes for this kind of hydrocarbon bring significant technological challenges. In this scenario, the enhanced solvent de-asphalting (*e*-SDA) process was proposed as highly innovative nanotechnology for improving the deasphalted oil (DAO) quality and catalytic conversion of the pitch. There was proven that the presence of nanoparticles generates DAO samples with lower asphaltene and sulfur content, higher °API and distillable fraction, and expected viscosity values than those obtained with the traditional solvent deasphalting process (SDA). The catalytic decomposition of the pitch or residue there was also potentiated by the presence of nanoparticles optimized with this purpose, reducing the temperature at which this process occurs and producing more gases helpful in generating energy or for being used in enhanced oil recovery methods.

Keywords: heavy oil, SDA, *e*-SDA, DAO, nanoparticles, asphaltenes, catalytic oxidation, simplex-centroid mixture design.

DESARROLLO DE UN PROCESO DE DESASFALTADO CON SOLVENTES MEJORADO CON NANOPARTÍCULAS (*e*-SDA) Y DESCOMPOSICIÓN CATALÍTICA DEL PITCH

Resumen

El panorama energético mundial y diferentes alternativas técnicas existentes para abastecer la creciente demanda de energía han hecho que en la industria del petróleo y el gas se dirija la atención a los crudos pesados y extrapesados. Sin embargo, los procesos de producción, transporte y refinación de este tipo de hidrocarburo presentan importantes desafíos tecnológicos. En este escenario, el proceso de desasfaltado con solventes mejorado con nanotecnología (*e*-SDA) se propuso como una alternativa altamente innovadora para mejorar la calidad del crudo desasfaltado (DAO) y los procesos de conversión catalítica del pitch. Se comprobó que la presencia de nanopartículas genera DAO con menor contenido de asfaltenos y azufre, mayor ºAPI y fracción destilable, y valores de viscosidad esperados más bajos que los obtenidos con el proceso tradicional de desasfaltado por solventes (SDA). La descomposición catalítica del pitch, o residuo, también fue potenciada por la presencia de nanopartículas optimizadas con este fin, reduciendo la temperatura a la que ocurre este proceso y produciendo una mayor cantidad de gases útiles para generar energía o para ser utilizados en métodos de recuperación mejorada de petróleo.

Palabras clave: crudo pesado, SDA, *e*-SDA, DAO, nanopartículas, asfaltenos, oxidación catalítica, diseño de mezclas simple con centroide.

Content

Abstract *4*
Resumen *5*
List of Figures *8*
List of Tables *11*
Introduction *13*
1. An enhanced-solvent deasphalting process (e-SDA): Effect of inclusion of SiO_2 nanoparticles in the quality of deasphalted oil *15*
1.1. Introduction 16
1.2. Material and methods 18
1.2.1. Materials and chemicals 18
1.2.2. DAO separation and characterization 19
1.3. Modelling 19
1.4. Results 20
1.4.1. Solvent to oil ratio effects 20
1.4.2. Temperature effects 26
1.4.3. Effect of the type of solvent 28
1.4.4. Effects of nanoparticle dosage 30
1.5. Partial conclusions 34
2. Effect of the nanoparticle's chemical nature on DAO quality and catalytic oxidation of pitch *35*
2.1. Materials and methods 36
2.1.1. Materials 36
2.1.2. Methods 36
2.1.2.1. Nanoparticles characterization 36
2.1.2.2. *n*-C_7 asphaltene extraction 37
2.1.2.3. Completely deasphalted oil extraction 37
2.1.2.4. Equilibrium adsorption isotherms 37
2.1.2.5. DAO separation and characterization 38
2.1.2.6. *n*-C_7 asphaltene and pitch oxidation in the absence and presence of nanoparticles 38
2.2. Modeling 38
2.2.1. Adsorption isotherm with the solid-liquid equilibrium (SLE) model 38
2.2.2. Estimation of activation energy (OFW) 39
2.3. Results 40
2.3.1. Commercial nanoparticles characterization 40
2.3.2. Completely deasphalted oil 40
2.3.3. *n*-C_7 asphaltene adsorption 42
2.3.4. DAO yield and quality 44
2.3.5. *n*-C_7 asphaltenes catalytic oxidation 48
2.3.6. Pitch catalytic oxidation 51
2.4. Partial conclusions 53
3. Improvement of the catalytic properties of selected support through a simplex-centroid mixture design *54*
3.1. Materials and methods 54
3.1.1. Materials 55
3.1.2. Methods 55
3.1.2.1. Nanoparticles functionalization 55

3.1.2.2. Nanoparticles characterization 55
3.2. Modeling. Simplex-centroid mixture design 55
3.3. Results 58
3.3.1. Functionalized nanoparticles characterization 58
3.3.2. *n*-C_7 asphaltene adsorption 58
3.3.3. DAO yield and quality 60
3.3.4. *n*-C_7 asphaltenes and pitch catalytic oxidation 64
3.3.5. Optimization of NiO and PdO dosage 69
3.4. Partial conclusions 70
4. Optimized nanoparticles and their impact on DAO quality and catalytic decomposition of the pitch under isothermal conditions 71
4.1. Materials and methods 71
4.1.1. Materials 71
4.1.2. Methods 72
4.1.2.1. *n*-C_7 asphaltene and pitch isothermal oxidation in the absence and presence of nanoparticles 72
4.1.2.2. Evaluation of the produced gases in the catalytic oxidation process 72
4.1.2.3. Nanoparticles regeneration 72
4.2. Modeling. Estimation of isothermal activation energy 73
4.3. Results 73
4.3.1. Optimized nanoparticles characterization 73
4.3.2. *n*-C_7 asphaltenes adsorption and DAO yield and quality 74
4.3.3. *n*-C_7 asphaltenes and pitch catalytic decomposition 77
4.3.4. *n*-C_7 asphaltenes and pitch isothermal catalytic decomposition and gaseous products 80
4.4. Partial conclusions 86
5. Conclusions and recommendations 88
5.1. Conclusions 88
5.2. Recommendations 88
6. Publications and awards 89
6.1. Scientific papers 89
6.2. Oral presentations and posters 89
6.3. Awards 89
Bibliography 90

List of Figures

Figure 1. Schematic diagram of the *e*-SDA process. The red box corresponds to studied part of proposed process in this paper. 18
Figure 2. Effect of the solvent to oil ratio in (a) DAO and (b) pitch yields for the SDA and *e*-SDA processes using SiO_2 nanoparticles at a dosage of 5 wt%, 25°C and *n*-heptane as the solvent. 21
Figure 3. Effect of solvent to oil ratio on DAO quality related to (a) asphaltene (b) sulfur content and (c) API gravity for the SDA and *e*-SDA processes using SiO_2 nanoparticles at a dosage of 5 wt%, 25°C and *n*-heptane as the solvent. 23
Figure 4. Viscosity and shear stress as a function of shear rate for (a) crude oil and DAO after SDA and *e*-SDA with SOR values of (b) 4, (c) 8 and d) 12 at 25°C with a fixed dosage of SiO_2 nanoparticles 5 wt% and *n*-heptane as the solvent. 26
Figure 5. Viscosity and shear stress of the DAO as a function of shear rate for the SDA and *e*-SDA processes at 70°C using a SiO_2 nanoparticles dosage of 5 wt% and an SOR of 8 with *n*-heptane as the solvent. 28
Figure 6. Viscosity and shear stress of the DAO as a function of shear rate for the SDA and *e*-SDA processes at 25°C using SiO_2 nanoparticles at a dosage of 5 wt% and an SOR of 8 with n-pentane as the solvent. 30
Figure 7. Effect of the SiO_2 nanoparticles dosage in (a) DAO and (b) pitch yields for the *e*-SDA process at SOR value of 8, at 25°C and using *n*-heptane as the solvent. 31
Figure 8. Effect of SiO_2 nanoparticles dosage in DAO quality related to (a) asphaltene and (b) sulfur content and (c) API gravity for the *e*-SDA processes at SOR value of 8, at 25°C and using *n*-heptane as a solvent. 32
Figure 9. Viscosity and shear stress as a function of shear rate for SiO_2 nanoparticles dosages of (a) 2.5 and (b) 10 wt% at SOR = 8, 25°C and using *n*-heptane as the solvent. 33
Figure 10. SARA fractions for c-DAO obtained with a SOR of 40 of n-heptane. 41
Figure 11. Viscosity as a function of shear stress for c-DAO obtained with a SOR of 40 of n-heptane. 41
Figure 12. Adsorption isotherms of n-C_7 asphaltenes onto Si7, Si200, Al and Ce nanoparticles at 25 °C expressed in (a) mg/m^2 and (b) g/g. 43
Figure 13. DAO and pitch yields for the SDA and e-SDA processes for Si7, Si200, Al and Ce at dosages of 5 wt% and n-heptane as the solvent with a SOR of 8 at 25°C. 45
Figure 14. DAO yield (wt%) for the e-SDA process carried out with Si7, Si200, Al and Ce vs. q_m (g/g) parameter for estimated SLE model and linear adjustment. 45
Figure 15. SARA fractions and sulfur content for the SDA and e-SDA processes using Si7, Si200, Al and Ce at 5 wt% and n-heptane as the solvent with a SOR of 8 at 25°C. 46
Figure 16. DAO API gravity and Conradson carbon residue for the SDA and e-SDA processes using Si7, Si200, Al and Ce at 5 wt% and n-heptane as the solvent with a SOR of 8 at 25°C. 47
Figure 17. Viscosity as a function of shear stress for the SDA and e-SDA processes using Si7, Si200, Al, Ce at dosages of 5 wt% and n-heptane as the solvent with a SOR of 8 at 25°C. 48
Figure 18. (a) Rate of mass loss and (b) conversion for the n-C_7 asphaltenes as a function of temperature in the absence and the presence of Si7, Si200, Al and Ce nanoparticles with the

airflow rate of 100 mL/min, the heating rate of 10°C/min and n-C_7 asphaltene loading 0.2 mg/m^2. 50
Figure 19. Activation energies estimated through the OFW method for catalytic oxidation of n-C_7 asphaltenes in the absence and presence of Si, Si200, Al and Ce. 51
Figure 20. (a) Rate of mass loss and (b) conversion of the pitch for the SDA and e-SDA processes carried out with Si7, Si200, Al and Ce nanoparticles with the airflow rate of 100 mL/min and the heating rate of 10°C/min. 52
Figure 21. Activation energies evaluated for thermal cracking of pitch for the SDA and e-SDA processes carried out with Si7, Si200, Al and Ce nanoparticles. 53
Figure 22. Simplex-centroid mixture design with Si7, nickel and palladium. 57
Figure 23. Adsorption isotherms of n-C_7 asphaltenes onto SiNi5, SiNi10, SiPd5, SiPd10, SiNi3.3Pd3.3 and SiNi5Pd5 nanoparticles at 25 °C expressed in (a) g/g and (b) mg/m^2. 60
Figure 24. DAO and pitch yields for the e-SDA process for SiNi5, SiPd5, SiNi10, SiPd10, SiNi3.3Pd3.3 and SiNi5Pd5 at dosages of 5 wt% and n-heptane as the solvent with a SOR of 8 at 25°C. 61
Figure 25. SARA fractions and sulfur content for the e-SDA process using SiNi5, SiPd5, SiNi10, SiPd10, SiNi3.3Pd3.3 and SiNi5Pd5 at dosages of 5 wt% and n-heptane as the solvent with a SOR of 8 at 25°C. 62
Figure 26. DAO API gravity and carbon Conradson residue the e-SDA process using SiNi5, SiPd5, SiNi10, SiPd10, SiNi3.3Pd3.3 and SiNi5Pd5 at dosages of 5 wt% and n-heptane as the solvent with a SOR of 8 at 25°C. 63
Figure 27. Viscosity as a function of shear rate for the e-SDA process using SiNi5, SiPd5, SiNi10, SiPd10, SiNi3.3Pd3.3 and SiNi5Pd5 at dosages of 5 wt% and n-heptane as the solvent with a SOR of 8 at 25°C. 64
Figure 28. (a) Rate of mass loss and (b) conversion for n-C_7 asphaltenes as a function of temperature in the presence of SiNi5, SiNi10, SiPd5, SiPd10, SiNi3.3Pd3.3 and SiNi5Pd5 nanoparticles with the airflow rate of 100 mL/min, the heating rate of 10°C/min and n-C_7 asphaltene loading 0.2 mg/m^2. 66
Figure 29. Activation energies evaluated for thermal cracking of n-C_7 asphaltenes in the absence and presence of SiNi5, SiNi10, SiPd5, SiPd10, SiNi3.3Pd3.3 and SiNi5Pd5. 67
Figure 30. (a) Rate of mass loss and (b) pitch conversion for e-SDA process carried out with SiNi5, SiPd5, SiNi10, SiPd10, SiNi3.3Pd3.3 and SiNi5Pd5 nanoparticles with the airflow rate of 100 mL/min and the heating rate of 10°C/min. 68
Figure 31. Activation energies estimated for thermal cracking of the pitch for SDA and e-SDA process carried out with SiNi5, SiNi10, SiPd5, SiPd10, SiNi3.3Pd3.3 and SiNi5Pd5 nanoparticles. 69
Figure 32. Contour plot for the expected temperature values at the beginning of the oxidation process. 70
Figure 33. Contour plot for the expected values of S_{BET} according to the proposed SCMD. 74
Figure 34. Adsorption isotherms of n-C_7 asphaltenes in SiNi3.2Pd5.5 expressed in (a) g/g and (b) mg/m^2. 75
Figure 35. Contour plot for the expected values of (a) DAO yield (%) and DAO quality determined through (b) asphaltene content (%), (c) API gravity and (d) viscosity (cP). 77
Figure 36. Mass loss and conversion rate for n-C_7 asphaltenes as a function of temperature in the presence of SiNi3.2Pd5.5 nanoparticles with the airflow rate of 100 mL/min, the heating rate of 10°C/min and n-C_7 asphaltene loading 0.2 mg/m^2. 78

Figure 37. Rate of mass loss and conversion of the pitch for e-SDA process as a function of temperature in the presence of SiNi3.2Pd5.5 nanoparticles with the airflow rate of 100 mL/min, the heating rate of 10°C/min and n-C_7 asphaltene loading 0.2 mg/m^2. 79
Figure 38. Activation energies evaluated for thermal cracking of n-C_7 asphaltenes and pitch for e-SDA process carried out with SiNi3.2Pd5.5 nanoparticles in cycles from 1 and 5..... 79
Figure 39. Isothermal conversion for catalytic oxidation of n-C_7 asphaltenes in the absence (390 °C) and presence (190 °C) of Si7, SiNi5Pd5 and SiNi3.2Pd5.5 at cycles 1 and 5. Airflow rate = 100 mL/min and n-C_7 loading 0.2 mg/m^2. 81
Figure 40. Evolution profiles of gaseous products during catalytic oxidation under isothermal conditions of n-C_7 asphaltenes in the absence (390 °C) and presence (190 °C) of Si7, SiNi5Pd5 and SiNi3.2Pd5.5 at cycle 1 and 5. Airflow rate = 100 mL/min and n-C_7 loading 0.2 mg/m^2. 82
Figure 41. Isothermal conversion for catalytic oxidation of pitch in the absence (390 °C) and presence (340 °C) of Si7, SiNi5Pd5 and SiNi3.2Pd5.5 at cycles 1 and 5. Airflow rate = 100 mL/min. 83
Figure 42. Evolution profiles of gaseous products during catalytic oxidation under isothermal conditions of SDA pitch in the absence (390 °C) and presence (340 °C) of Si7, SiNi5Pd5 and SiNi3.2Pd5.5 at cycles 1 and 5. Airflow rate = 100 mL/min. 84
Figure 43. Arrhenius plot for the isothermal model of catalytic and thermal oxidation of a) n-C_7 asphaltene and b) pitch. All in the presence and absence of Si7, SiNi5Pd5 and SiNi3.2Pd5.5 (cycles 1 and 5). 85

List of Tables

Table 1. Ostwald-de Waele estimated parameters for rheological experiments on crude oil and DAO after SDA and e-SDA with SOR values of 4, 8 and 12 at 25°C with a fixed dosage of SiO_2 nanoparticles 5 wt% and n-heptane as the solvent. 26
Table 2. Yield and quality of the DAO after the SDA and e-SDA processes at 70°C using a SiO_2 nanoparticles dosage of 5 wt% and an SOR of 8 with n-heptane as the solvent. 27
Table 3. Ostwald-de Waele estimated parameters from rheological experiments for DAO after the SDA and e-SDA processes with an SOR of 8 at 70°C using SiO_2 nanoparticles and n-heptane as the solvent. 28
Table 4. Yield and quality of the DAO after the SDA and e-SDA processes at 25°C using SiO_2 nanoparticles at a dosage of 5 wt% and an SOR of 8 with n-pentane as the solvent. 29
Table 5. Ostwald-de Waele estimated parameters from rheological experiments for the DAO after the SDA and e-SDA processes with an SOR of 8 at 25°C using SiO_2 nanoparticles at a dosage of 5 wt% and an SOR of 8 with n-pentane as the solvent. 30
Table 6. Ostwald-de Waele estimated parameters for rheological experiments on DAO after e-SDA with SiO_2 nanoparticles dosage of 2.5 and 10 wt% at SOR = 8, 25°C and using n-heptane as the solvent. 34
Table 7. Properties of EHO sample 36
Table 8. Measured values of hydrodynamic diameter and surface area (S_{BET}) for Si7, Si200, Al and Ce nanoparticles. 40
Table 9. Oswald-de Waele estimated parameters for rheological experiments onto c-DAO obtained with a SOR of 40 of n-heptane. 42
Table 10. Estimated values of the SLE model parameters for the adsorption isotherms of n-C_7 asphaltenes onto Si7, Si200, Al and Ce nanoparticles at 25 °C. 44
Table 11. Oswald-de Waele estimated parameters for rheological experiments for the SDA and e-SDA processes using Si7, Si200, Al, Ce at 5 wt% and n-heptane as the solvent with a SOR of 8 at 25°C. 48
Table 12. Nomenclature and mass fraction of prepared nanoparticles composed by silica support (SiO_2) of 7 nm with NiO and PdO. 57
Table 13. Hydrodynamic diameter, surface area and the crystal size of prepared nanoparticles composed by silica support (SiO_2) of 7 nm with NiO and PdO. 58
Table 14. Estimated values of the SLE model parameters for the adsorption isotherms of n-C_7 asphaltenes onto functionalized nanoparticles 60
Table 15. Oswald-de Waele estimated parameters for rheological experiments for the e-SDA process using SiNi5, SiPd5, SiNi10, SiPd10, SiNi3.3Pd3.3 and SiNi5Pd5 at dosages of 5 wt% and n-heptane as the solvent with a SOR of 8 at 25°C. 64
Table 16. Estimated values of the SLE model parameters for the adsorption isotherms of n-C_7 asphaltenes onto SiNi3.2Pd5.5. 75
Table 17. DAO yield and quality of DAO obtained by e-SDA process with SiNi3.2Pd5.5 nanoparticles on 5 consecutive cycles of regeneration. 76

Table 18. Estimated effective isothermal energy ($E_{\alpha.isoT}$) for catalytic oxidation of n-C_7 asphaltene and pitch. All in the presence and absence of Si7, SiNi5Pd5 and SiNi3.2Pd5.5 (cycles 1 and 5). 85

Introduction

The actual energetic world outlook considers the hydrocarbon industry to supply more than 50 % of the total world energy demand by 2040 [1, 2]. Precisely, this fact, combined with the percentual distribution of the whole world's oil reserves, with 46.7 % of conventional oil, 32.0 of oil sands/bitumen, 21.3 % of heavy and extra-heavy oil [3], shows the importance of focus technology developments into making more viable this kind of fluids. In the same line, some data reinforces the importance of heavy and extra heavy oil on the energetic matrix, establishing that by meanwhile in 2013, for each barrel of extra-heavy oil produced, more than four barrels of conventional oil were extracted [4]. However, it's expected by 2035 that this proportion will change, and by every three barrels of conventional oils, approximately five barrels of extra-heavy oil will be produced [4].

Heavy oils (HO) and extra-heavy oils (EHO) reservoirs can be found in a lot of places around the world in countries like Canadá, Venezuela and even Colombia [5-8]. The characteristic of these types of crude oil, related to their low API gravity and viscosity values [9], bring significant technological challenges associated with their production, transportation and refining [9-11]. Some of these difficulties are linked to asphaltenes, the most polar compounds in the crude oil, which causes their self-association and formation of large aggregates [12, 13]. Asphaltenes can be found in high concentrations in HO and EHO, reaching values of almost 60 wt% [14-16]. Increments of asphaltene content in 15 wt% to 20 wt% can multiplicate by 30 the expected viscosity for crude oil [17, 18]. This situation can be explained by the asphaltene tendency to favor forming a viscoelastic network [17-22], and high sulfur concentrations with strong C-S and C=S bonds [23, 24].

There are mainly two groups of technologies for upgrading HO and EHO and reducing their viscosity: in-situ [25-36] and on-site [37-51]. The first group of technologies consists of injecting hot fluids into the reservoir [28-36, 52-66] or generating in situ combustion [25-27] for heating the porous media and its fluids, improving their mobility conditions. This group of techniques can also cause problems like formation damage for asphaltene precipitation and changes in reservoir porosity, permeability and wettability [13, 66-68]. On-site technologies are carried out at the surface, and the reduction of HO and EHO viscosities are achieved through their dilutions with solvents and light hydrocarbons [38, 39] and solvent de-asphalting (SDA) [8, 69, 70].

SDA process is a physical process that separates the crude oil into two phases: the deasphalted oil (DAO) and the pitch or residue [69]. A paraffinic solvent is used to achieve the separation, and its effect in this process has been studied [69, 71-75]. There was also examined the impact of other involved variables like type of used solvent [69, 71-82], temperature [75, 83, 84], and solvent to oil ratio (SOR) [72, 74, 85-88] in the DAO yield and quality. Previously, the impact of adding adsorbent materials, of macrometric and micrometric sizes, to the SDA process was also evaluated [89-93]. In this sense, until this investigation, there hasn't been reported in the literature any work related to

the role of the nanomaterials in deasphalting processes and the separation efficiency of DAO and pitch, the improvement of the quality of the former and the catalytic oxidation of the latest.

In this sense, the enhanced solvent de-asphalting (*e*-SDA) process was developed, and the role of SiO_2 nanoparticles under different operative conditions was evaluated [70]. This technology proved the potential of nanoparticles in improving DAO quality despite the evaluated operation conditions. These results constitute an opportunity to keep assessing variables like the chemical nature of the used nanoparticle, the impact in the catalytic oxidation of the pitch and the produced gases. Hence, the main objective of this study is to develop the *e*-SDA process incorporating novel nanomaterials that improve DAO quality and potentiate the catalytic decomposition of pitch and the obtention of higher amounts of gaseous products. Thus, this document is divided into four main chapters that include: I) An Enhanced-Solvent Deasphalting Process (*e*-SDA): Effect of Inclusion of SiO_2 Nanoparticles in the Quality of Deasphalted Oil, II) the effect of the nanoparticles chemical nature into DAO quality and catalytic oxidation of pitch, III) the improvement of the catalytic properties of selected support through a simplex-centroid mixture design and IV) optimized nanoparticles and their impact on DAO quality and catalytic decomposition of the pitch under isothermal conditions.

1. An enhanced-solvent deasphalting process (*e*-SDA): Effect of inclusion of SiO_2 nanoparticles in the quality of deasphalted oil

Abstract

In this work, the effect of nanoparticles in de-asphalting heavy oil and extra-heavy oil process at laboratory-scale based on the conventional solvent deasphalting process was studied and named enhanced-solvent deasphalting *e*-SDA process. This work evaluated the effect of the nanoparticles of SiO_2 in the separation efficiency based on de-asphalted oil (DAO) fraction quality compared to the conventional process of deasphalting (SDA). Different effects have been assessed such as solvent to oil ratio, operating temperatures, type of solvent and SiO_2 nanoparticles dosage. The DAO quality was based on the asphaltene and sulfur contents, API gravity, distillable fraction and rheological properties. The improvement of the process from the use of nanoparticles was confirmed with important reductions in the asphaltene and sulfur contents in the DAO of up to 24% and 23%, respectively, in comparison with the SDA process. Also, the API gravity can be increased by approximately 14% with the *e*-SDA process. The rheological properties of the DAO were improved by the inclusion of nanoparticles showing reductions in the viscosities of the DAO greater than 50% in comparison with the conventional process. These results lead to the conclusion that the *e*-SDA process improves the DAO quality when compared with the typical de-asphalting process.

Keywords
Heavy Oil, SDA, *e*-SDA, DAO, Nanoparticles, Asphaltene, Rheology.

1.1. Introduction

Growth in global energy demand of approximately 50% is expected by the year 2040, reaching approximately 400 millions of barrels of oil equivalent per day (mboe/d) [94]. Because of this growth, nonconventional sources of hydrocarbons, such as heavy oil (HO) and extra-heavy oil (EHO), with nearly 70% of world oil reserves [95], of which EHO reserves correspond to 32% of the global oil reserves [96], have much potential.

HO and EHO are characterized by high specific gravities and high viscosities [9]. According to the American Petroleum Institute (API) gravity, HO is defined by having an API gravity between 10° and 22.3° [9]. EHO has an API gravity less than 10º and a viscosity at reservoir conditions higher than 10000 cP [8, 9, 97]. HO and EHO reservoirs are widely distributed throughout the world in countries such as Venezuela, Canada and Colombia [5-8], imposing several technological challenges in their production, transportation and refining in these countries [9-11]. One of the main characteristics of HO and EHO is the high concentration of high molecular weight asphaltenes that are complex and highly polar compounds with large amounts of heteroatoms containing O, N and S, as well as metals such as Ni, Fe and V [98-101]. These heteroatoms and their location in the asphaltene structure, cause these molecules to be the most polar constituents in crude oil, leading to their self-association and formation of large asphaltic flocs [12, 13]. For example, for HO and EHO, in which asphaltenes are in high concentrations [15, 16], the viscosity increases due to the significant influence of these molecules on the rheology resulting from the formation of a viscoelastic network [17-20]. Also, high concentrations of asphaltenes in HO and EHO that contain elevated concentrations of sulfur with strong C-S and C=S bonds drastically increase the viscosity [23, 24].

Technologies for viscosity reduction and/or upgrading of HO and EHO have been classified as in situ [25-36] and *on-site* [37-51] which are mainly focused on subsurface and surface processes, respectively. In situ upgrading techniques such as in situ combustion (ISC) [25-27], thermal cracking and its catalytic variations [32-36], as well as all technologies assisted by nanocatalysts [28-31], are technologies that operate at high temperatures and require considerable amounts of fuel and/or steam/gases, thereby limiting their utilization [52-54]. Other thermal methods commonly used for viscosity reduction (but without an upgrading process) are based on the fluids injected into the reservoir such as the steam-assisted gravity drainage (SAGD) process [55, 56], hot water flooding and continuous or cyclic (*huff-n-puff)* steam injection [52, 54, 59, 60]. However, in these processes, the crude oil returns to its original viscosity when the temperature of the crude oil decreases [57, 58]. Other nonthermal techniques for viscosity reduction have been used in reservoirs including injection of diluents (naphtha and light crude oils) [61-63] and CO_2 injection in enhanced oil recovery (EOR) processes [64-66], among others. Nevertheless, these techniques could initiate the destabilization of the asphaltenes, which in some cases, leads to formation damage due to their precipitation/deposition in the pore throats, reducing porosity and permeability and affecting reservoir wettability [13, 66-68]. Also, these techniques for the reduction of HO and EHO viscosities require continuous injections into the reservoir making this an expensive process due to the use of large volumes of diluents.

Because of these adverse factors, technologies that could be applied at the wellhead would be an efficient alternative to the current technologies. Several techniques have been used for HO and EHO viscosity reduction at the surface, such as dilution with solvents and light hydrocarbons [38, 39] or solvent de-asphalting (SDA) [8]. SDA is one of these technologies wich is often used by the oil & gas industry for *on-site* upgrading. It is considered to be a viable option because operating costs can be reduced by the recovering and recycling of the solvents [69]. SDA is an economical process to remove concentrated asphaltene or pitch, the dirtiest part of HO and EHO [69] and has been widely studied since the first attemps to separe or distilling oils in 1920s [102, 103]. Since then many efforts have been made to understand this process, the effect of the variables present involved, and how to improve it [88, 104-107]. SDA is a physical process in which there is a separation of two phases, the deasphalted oil (DAO) and the residue or pitch [69]. The DAO is removed from the HO or EHO by solvent extraction using paraffinic hydrocarbons in which there is no chemical reaction between the crude oil feed and the paraffinic solvent [69, 71-75]. Researchers have evaluated the effects of the chemical nature of the solvent [69, 71-82], temperature [75, 83, 84], operating pressure [76-78, 83, 108, 109] and solvent to oil ratio [72, 74, 85-88] on the yield of DAO and/or pitch, as well as the DAO quality in some studies. Improvements of the SDA through the addition of macro- and microadsorbent materials have been reported in the literature, showing improvement in the DAO yield and quality [89, 90]. In some patents, the use of microscale solids such as clay, silica, alumina, and zeolite materials have been reported, reaching a higher quality of the DAO [92, 93]. Regarding Si -based materials, Ikematsu et al. [91] proposed an improved SDA process by using SiO_2 microparticles. The authors proposed the use of amorphous SiO_2 with preferably particle size between 0.5 and 1.0 μm and surface area of 100-800 m^2/g [91].

Nevertheless, there have not yet been studies reported in the scientific literature about the role of nanoparticles (NPs) and their impact on the separation efficiency of the SDA process. These nanomaterials may offer special advantages for the SDA process due to their high surface area to volume ratio and hence a large number of available active sites, making them capable of selectively adsorbing asphaltenes onto their surfaces and enhancing the removal of the asphaltenes [30, 110-116]. In previous studies [115, 117] our research group has found that silica nanoparticles have a high affinity for asphaltene molecules, which could impact the efficiency directly of the SDA process. Franco et al. [115] showed that silica – based nanoparticles adsorbed up to 5.5 mg/m^2 of asphaltenes in comparison with microparticulate silica. Therefore, this study focused on evaluating the effects of adding nanoparticles to a typical SDA process with the purpose of enhancing the quality of the DAO and optimizing this procedure using nanotechnology in a process designated enhanced solvent de-asphalting (*e*-SDA). Lee et al. [69] provided a typical SDA process scheme that includes a solvent extractor, DAO/solvent separator and pitch stripper. The SDA process involves injecting an alkane into the crude oil to disrupt and to disperse its components causing the polar components to precipitate [8]. The present paper is the first step for proposing the *e*-SDA technology shown in Figure 1. The experimental tests carried out at laboratory-scale lead to the proposed *e*-SDA process to include the cyclic addition and recuperation of nanoparticles and the catalytic conversion of the

pitch for energy production. The *e*-SDA process produces a DAO having enhanced quality and CO_2 that could be used in the EOR process [64, 65].

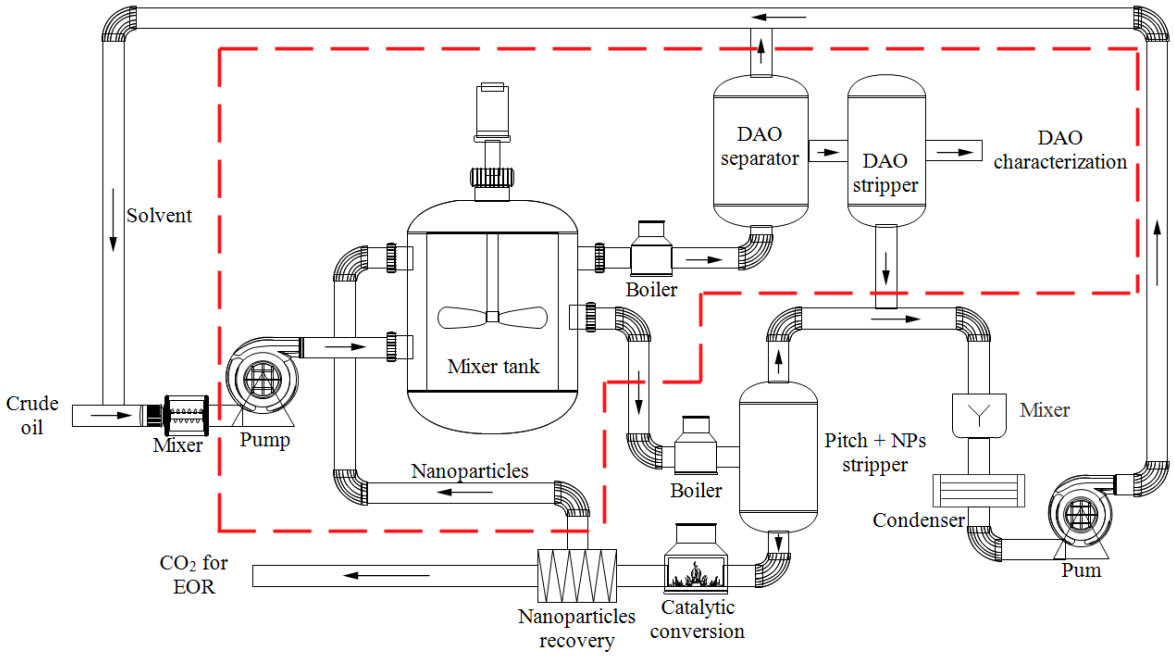

Figure 1. Schematic diagram of the *e*-SDA process. The red box corresponds to studied part of proposed process in this paper.

In this study laboratory-scale experimentation was made where the DAO and pitch yields are presented while focusing on the DAO quality by evaluating its asphaltene and sulfur contents, API gravity, distillable fraction and rheological properties. The rheological properties were described using a power law model commonly employed for this type of fluids.

1.2. Material and methods

1.2.1. Materials and chemicals

A Colombian extra-heavy crude oil obtained from a reservoir located in the department of Meta in Colombia's central region was used in these experiments. This EHO of 6.4°API had a content of asphaltenes and sulfur of 20.3 and 4.5 wt%, respectively. Its distillable fraction was approximately of 56% until 750ºC. Two different paraffinic solvents were used in the deasphalting process: *n*-heptane (99%, Sigma-Aldrich, St. Louis, MO) and *n*-pentane (99 %, Panreac, Barcelona, Spain). In this sense, the commercial fumed silica (SiO_2) nanoparticles (mean particle size of 7 nm and a surface area "S_{BET}" of 389 m^2/g) that were used to enhance the SDA process were obtained from Sigma-Aldrich (St. Louis, U.S.).

1.2.2. DAO separation and characterization

The experimental procedure begins with the addition of the paraffinic solvents to the oil at a defined solvent to oil mass ratio (SOR) for the SDA process. For the *e*-SDA process, an identical test was made using SiO_2 nanoparticles at different dosages of 2.5, 5.0 and 10 wt% of the crude oil mass based on the maximum amount of asphaltenes that can be adsorbed by the nanoparticles [117], such that the asphaltenes adsorbed onto the nanoparticles can be decanted in the separation facilities of the *e*-SAD process. For this, the selected amount of nanoparticles was premixed with selected solvent and sonicated at 25°C for 1 h. The mixture was stirred at 300 rpm for 2 h at 25°C. At this point, the precipitation of the pitch was achieved, and this was separated from the DAO by filtration with an 8 µm Whatman filter paper. At the end of the experiment, the solvent was separated from the DAO, and the solvent loss was calculated.

The DAO and pitch weight were determined to establish the SDA and *e*-SDA yields. On quality, the asphaltene and sulfur contents in the DAO fractions were determined, as well as their API gravities, rheological properties, and distillable fractions. The remaining asphaltenes in the DAO are a critical parameter because these are one of the responsible of the high viscosity values [12, 13, 17-20], just as the sulfur content and their bonds with carbon [23, 24]. In this sense, DAO asphaltene content was determined by extraction using an excess amount of *n*-heptane according to a standard procedure having a measured deviation of ± 0.01% that was described in previous studies [30, 113]. The sulfur content of the DAO and its API gravity were measured according to the procedures established by ASTM D-7220-12 [118] and ASTM D-1298-12 [119], respectively. The sulfur content was determined with an error in measurements of ± 0.01%, and those of the API gravity measurements were within ± 0.02°. DAO rheological measurements were conducted using a Kinexus rotational rheometer C-VOR 200 (Malvern Instruments, Worcestershire, UK), with a Peltier cell to maintain temperature control. The standard plate to plate geometry with a GAP of 300 microns was used. Rheological data were fitted to the model specified below. Finally, for each sample, the distillable fraction of the DAO was determined by gas chromatography following the ASTM D-7169-11 procedure [120], using an Agilent 7890A gas chromatograph (Agilent Technologies, Santa Clara, US). The analytical tests for the DAO quality determinations were repeated three times.

It is worth noting that different factors were assessed in the tests: SOR values of 4, 8 and 12; temperatures of 25 and 70ºC; type of solvent (*n*-pentane or *n*-heptane) and nanoparticles dosage. The experimental base scenario used an SOR = 8 using a dosage of 5 wt% of nanoparticles in the crude oil mass and *n*-heptane at 25ºC.

1.3. Modelling

The Ostwald-de Waele model was used to fit the experimental data. This model is determined by the following mathematical expression [121, 122]:

Equation 1. $$\mu = K\gamma^{n-1}$$

where, μ (cP) represents viscosity, γ (s^{-1}) is the shear rate, n (dimensionless) is called power-law index in which n <1 correspond to a shear-thinning non-Newtonian liquid or pseudo-plastic fluids, n >1 is characteristic of a shear-thickening non-Newtonian fluid, and finally n =1 is typical of Newtonian fluids [121, 122]. The K ($cP \cdot s^{n-1}$) parameter is called the consistency coefficient. It is associated with the viscosity at a shear rate of 1 s^{-1}. On this parameter, it can be noticed that when n is equal to 1, (a Newtonian fluid) this parameter has units of cP and can be interpreted as the fluid viscosity independent of shear rate. For determining the goodness of fit of the employed model, the nonlinear chi-square (χ^2) analysis and root-mean-square error (RMSE %) were used [123].

1.4. Results

1.4.1. Solvent to oil ratio effects

In this section, the results of solvent to oil ratio (SOR) effect on the DAO yield and the quality of SDA and *e*-SDA processes are presented. Figure 2 shows the DAO and pitch yields for both processes using *n*-heptane at a nanoparticles dosage of 5 wt% and a fixed temperature of 25°C. Increasing the SOR reduces the DAO yield (Figure 2a) and consequently increases the pitch yield (Figure 2b). These results are in agreement with those reported by several authors [72, 74, 85-88] in which this behavior is explained by the solvating power of solvent [74]. To further understand this phenomenon, it is necessary to consider resins in addition to asphaltenes that are responsible for considerable changes in the solvent power [74]. As the SOR increases, more resins are solubilized by the solvent and these are unable to act as peptizing (or interfacial) agents of asphaltenes [124-127] leading to their aggregation and precipitation [74, 124-127]. Hence, as the SOR increased, the pitch yield increased while the DAO yield decreased proportionally [72, 75].

On the other hand, the *e*-SDA process using SiO_2 nanoparticles has considerable effects on the DAO and pitch yields compared with the SDA process. It is worth mentioning that the silica nanoparticles selectivity to asphaltenes due to the presence of acid centers such as hydroxyl silanol (Si-OH) on their surface [127-129] and their interaction with the polar groups of asphaltenes are expected. Also, the DAO yields in the *e*-SDA process are lower in comparison with traditional SDA, and consequently the pitch yields are larger in the *e*-SDA process (Figure 2b). This increase of pitch can be explained by the adsorption phenomena between the silica nanoparticles and asphaltenes that has been widely studied and is determined by the affinity between adsorbent (SiO_2 nanoparticles) and adsorbate (asphaltenes), the asphaltene self-association over the surface of the nanoparticles, and their maximum adsorption capacity [130]. Franco et al. [115] studied asphaltene adsorption in different nanoparticles and found that the process strongly depends on of the surface structure and chemistry of the nanomaterial. In this way, SiO_2 nanoparticles added to the deasphalting process adsorb asphaltenes on their surface and enhance their precipitation and separation from the crude oil matrix. However, the trend obtained by DAO and pitch yields over the wide range of SOR evaluated can be considered constant, as seen in Figure 2a, indicating that the amount of solvent needed for the de-asphalting process can be reduced significantly by the addition of nanoparticles.

Additionally, it has been demonstrated that nanoparticles impact the viscosity of oil by altering the aggregation system of asphaltenes [22, 131]. This may modify the efficiency of the deasphalting process by lowering the system viscosity, reducing the mass-transfer resistance between fractions and thereby increasing the asphaltene extraction efficiency [90].

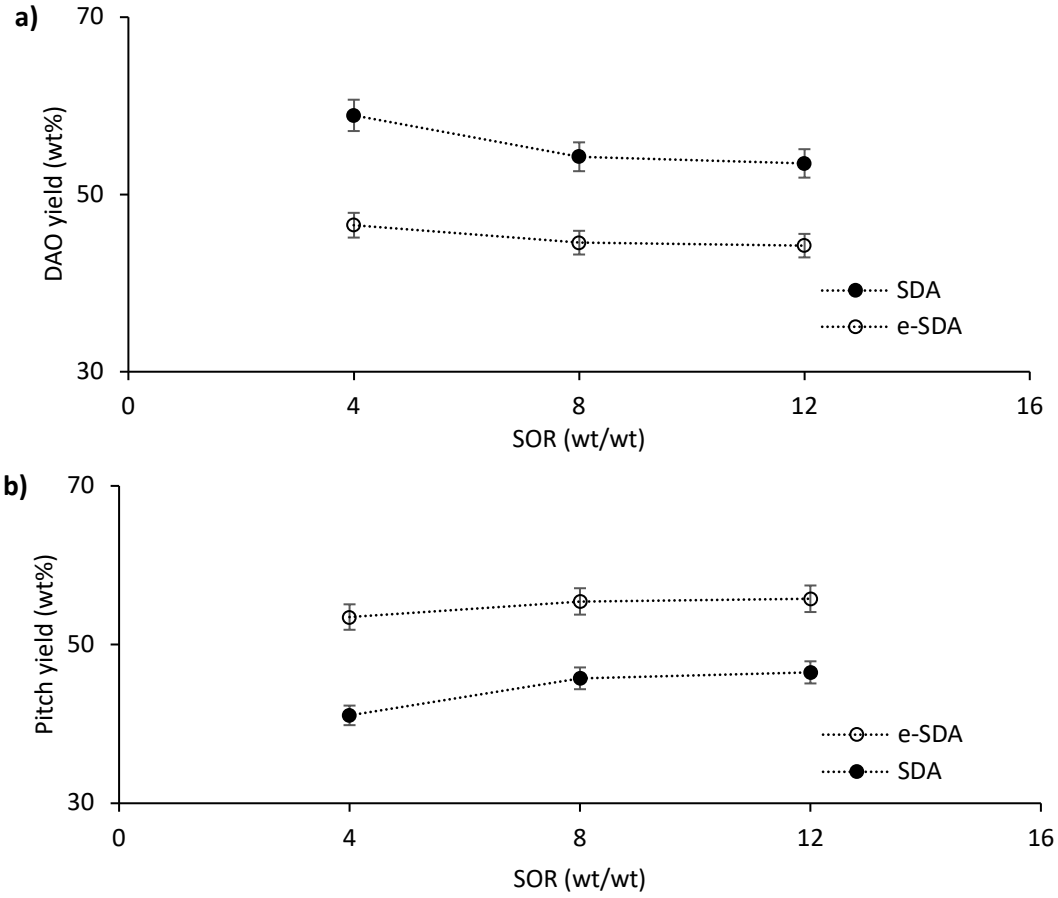

Figure 2. Effect of the solvent to oil ratio in (a) DAO and (b) pitch yields for the SDA and *e*-SDA processes using SiO_2 nanoparticles at a dosage of 5 wt%, 25°C and *n*-heptane as the solvent.

Figure 3 presents the DAO quality in three panels related to (a) asphaltene content, (b) sulfur content and (c) °API for both SDA and *e*-SDA processes. For the SDA process increasing the SOR decreased the asphaltene content in the DAO, as shown in Figure 3a. This situation can be explained because increasing the SOR leads to reducing the asphaltene solubility causing them to precipitate [74, 124-127]. For this reason, as the SOR increased, more asphaltenes were precipitated [76, 77] and therefore the DAO quality increased. These results are widely confirmed by previous studies that measured the content of asphaltene in DAO [69, 75, 78]. Regarding the sulfur content of the DAO, this is directly related to asphaltene content [75], which can be seen in Figure 3b. As the asphaltene content of the DAO decreased, the sulfur content decreased, showing the same trend as the asphaltene content as SOR increased. Thus, Figure 3(c) shows that increases of the SOR

increased the API gravity of the DAO. This result is consistent with the reductions in the asphaltene and sulfur contents [132].

The DAO quality was also affected by the addition of nanomaterials in the *e*-SDA process. As seen in Figure 3(a), the asphaltene content of the DAO was lower for all SOR values in comparison with the system without nanoparticles. This improvement in quality can be mainly explained by the interaction between the asphaltenes and the nanoparticles that remain in the pitch fraction, which also explains the sulfur content values of the *e*-SDA process that were clearly lower than those of the SDA process because of the direct relationship between the asphaltene and sulfur contents [75]. The sulfur content is nearly constant as the SOR increased and could be to O – and N – containing asphaltenes are more prone to get adsorbed on the silica nanoparticles than those containing sulfur [127, 129]. Additionally, Figure 3(c) shows that the *e*-SDA process improved the °API values of the DAO for all of the SOR values. This remarkable result is also related to the reduction of the DAO asphaltene content values in *e*-SDA versus the traditional SDA process [132]. This result can be contrasted with the simulated distillation results that show that the distillable fractions for all DAO samples (either SDA or *e*-SDA) were approximately 100% up to 750ºC.

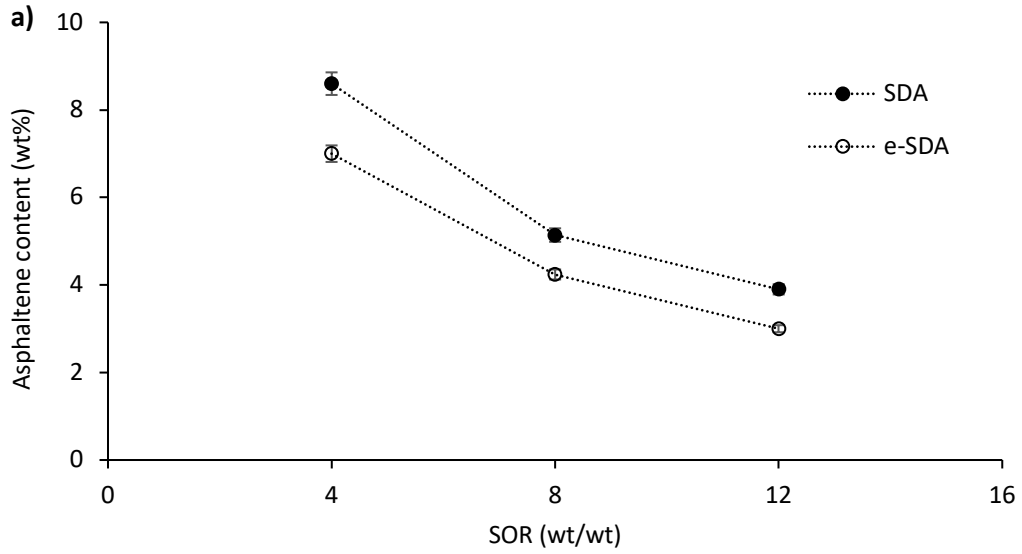

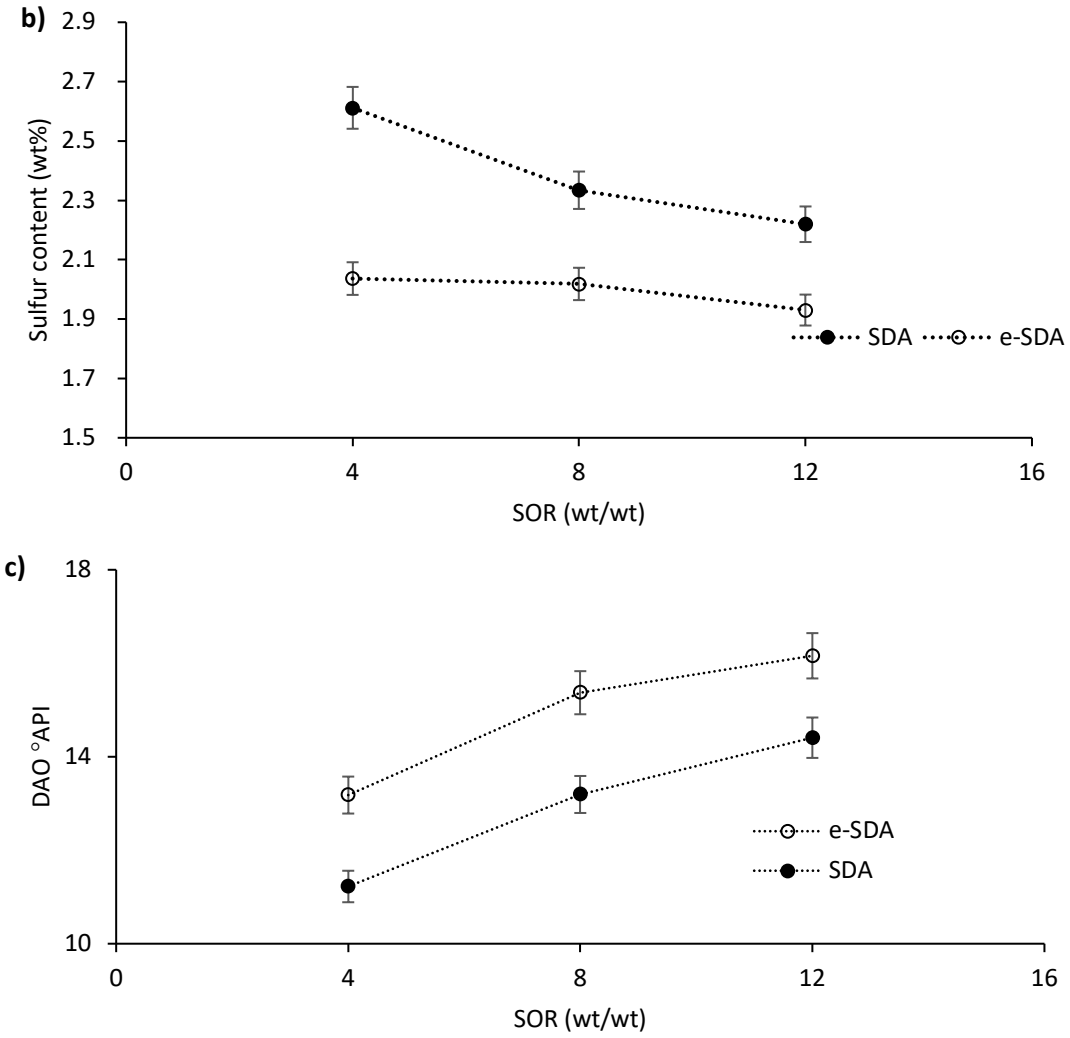

Figure 3. Effect of solvent to oil ratio on DAO quality related to (a) asphaltene (b) sulfur content and (c) API gravity for the SDA and *e*-SDA processes using SiO_2 nanoparticles at a dosage of 5 wt%, 25°C and *n*-heptane as the solvent.

Rheological measurements were conducted by triplicated to evaluate the DAO quality. Figure 4 shows the viscosity, shear stress and the fitting with the Oswald-de Waele model as a function of shear rate for (a) crude oil and for DAO obtained from tests made with SOR values of (b) 4, (c) 8 and (d) 12. The estimated parameters of the Oswald-de Waele model are summarized in Table 1. As shown in Figure 4(a), the crude oil had the expected shear-thinning behavior frequently known as pseudo-plastic behavior [122]. This is confirmed by the *n* parameter value in Table 1, which is clearly less than 1.

The DAO obtained from the SDA process with an SOR of 4 (Figure 4(b)) also exhibited a shear-thinning behavior. However, in this case, the n value is 0.906 and, being almost 1, had a nearly Newtonian behavior with a *K* value of 73321 $cP \cdot s^{n-1}$ that is related to the fluid viscosity at a shear rate value of 1 s^{-1}. For the same SOR = 4, the *e*-SDA process considerably improved the DAO

rheological properties as can be seen clearly from the results shown in Figure 4 and Table 1. The parameters of the Ostwald-de Waele model (*n* of 0.979 and *K* of 35522 cP·s^{n-1}) indicate an approximately Newtonian behavior with a viscosity of 35522 cP. The last parameter indicates that adding SiO_2 nanoparticles reduces expected viscosity of the DAO by more than 50%. For an SOR value of 8 in the SDA process (Figure 4(c)), the DAO rheological characteristics presented a similar trend with an approximately Newtonian behavior and viscosity of 19552 cP. For the same SOR, when the *e*-SDA process was conducted with SiO_2 nanoparticles, the rheological properties of the DAO were improved, having a viscosity of 11883 cP that indicates a viscosity reduction of 42% on the typical SDA process conducted without nanoparticles. The same performance was observed for the DAO with an SOR of 12 in which the viscosity was reduced from 10670 to 8504 cP in the SDA and *e*-SDA processes, respectively. These rheological results are interesting because these fluid properties determine the crude oil and DAO transporting conditions. In Figure 4 it is observed that the inclusion of SiO_2 nanoparticles significantly reduced the shear stress and the yield point in comparison with the SDA process in the absence of nanoparticles.

Finally, for the de-asphalting process conducted with and without nanoparticles, at all of the assessed SOR values, the estimated solvent losses were lower than 1.0 wt%.

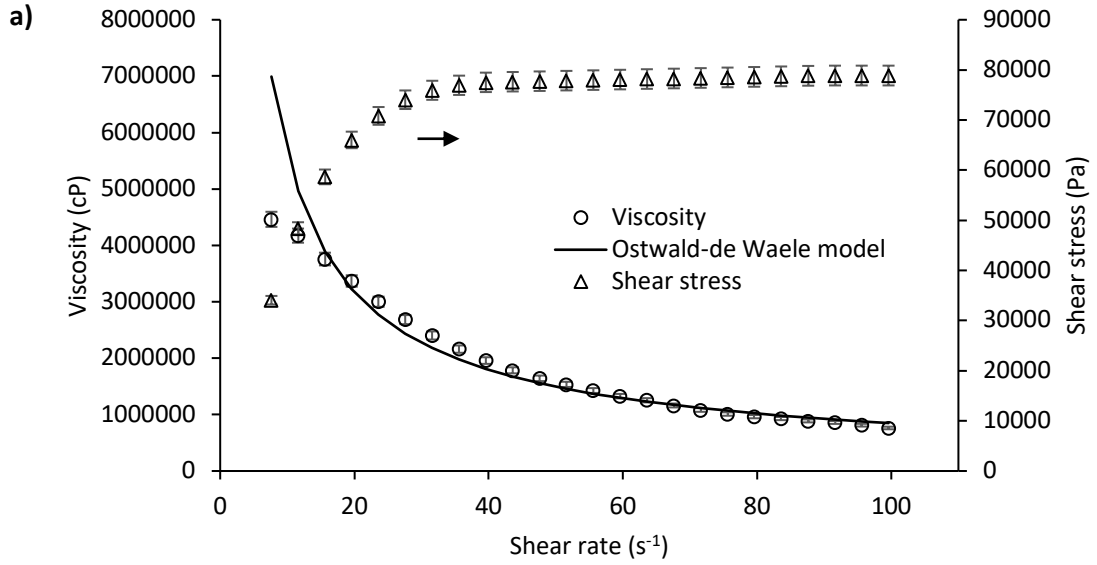

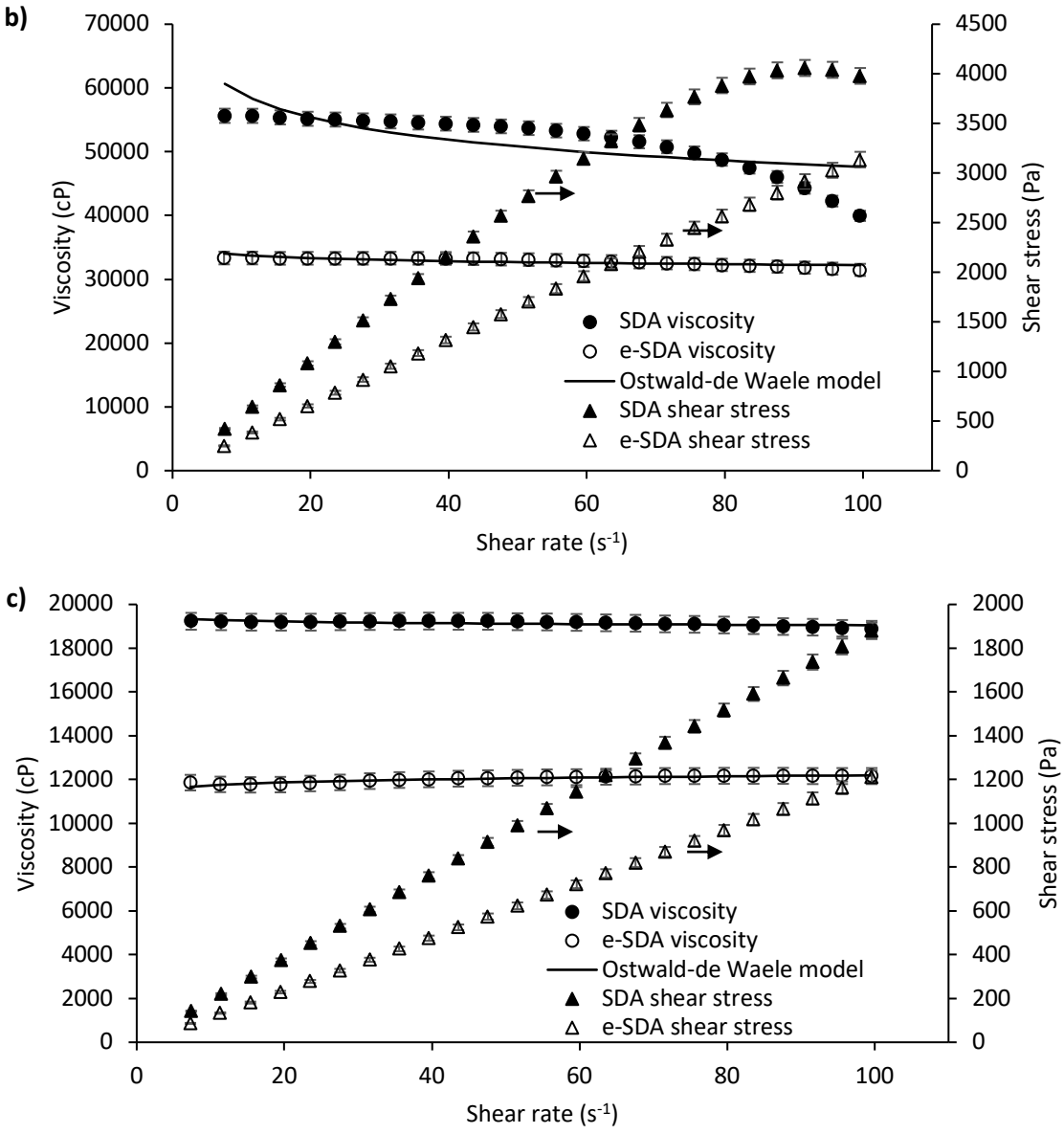
b)
Viscosity (cP)
Shear stress (Pa)
Shear rate (s-1)
SDA viscosity
e-SDA viscosity
Ostwald-de Waele model
SDA shear stress
e-SDA shear stress
c)
Viscosity (cP)
Shear stress (Pa)
Shear rate (s-1)
SDA viscosity
e-SDA viscosity
Ostwald-de Waele model
SDA shear stress
e-SDA shear stress

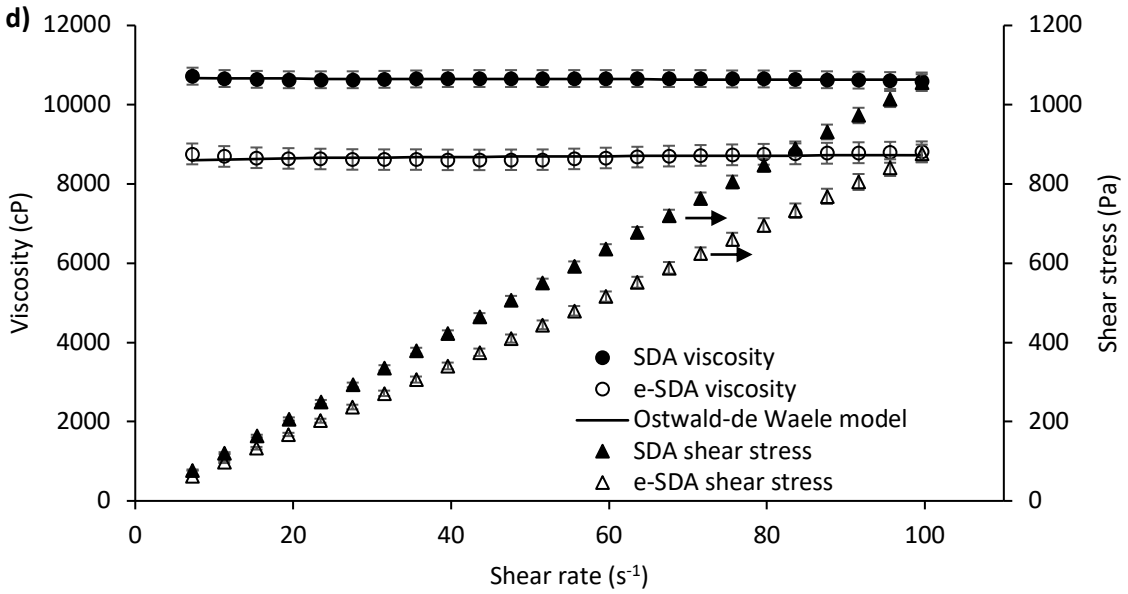

Figure 4. Viscosity and shear stress as a function of shear rate for (a) crude oil and DAO after SDA and *e*-SDA with SOR values of (b) 4, (c) 8 and d) 12 at 25°C with a fixed dosage of SiO_2 nanoparticles 5 wt% and *n*-heptane as the solvent.

Table 1. Ostwald-de Waele estimated parameters for rheological experiments on crude oil and DAO after SDA and *e*-SDA with SOR values of 4, 8 and 12 at 25°C with a fixed dosage of SiO_2 nanoparticles 5 wt% and n-heptane as the solvent.

Sample		*K* (cP·s^{n-1})	*n* (dimensionless)	RSME%	χ^2
Process	**SOR**				
Crude Oil	**0**	37051877	0.180	9.29	3.45
SDA	**4**	73321	0.906	6.20	2.37
	8	19552	0.994	0.44	0.18
	12	10670	0.999	0.18	0.08
***e*-SDA**	**4**	35522	0.979	1.15	0.48
	8	11883	1.017	0.40	0.14
	12	8504	1.006	0.70	0.29

1.4.2. Temperature effects

Procedures were conducted with *n*-heptane as the solvent at an SOR of 8 with a SiO_2 nanoparticles dosage of 5 wt% and a fixed temperature of 70°C to assess the temperature effects. The results are summarized in Table 2 and are in agreement with the literature reports, which found that within the range evaluated, increasing the temperature increases the pitch yield and reduces the DAO yield [75, 83, 84]. This can be seen for both the SDA and *e*-SDA processes and can be explained by increases in the differences in the solubility parameters and molar volumes between the solvent

and crude oil as temperature rises, leading to a larger region of immiscibility in a solvent - pitch – DAO system [75]. In this sense, increasing system temperature has a similar effect compared to that when the molecular weight of used solvent is decread. For the SDA, the DAO yield decreased from 54.3% at 25°C to 48.3% at 70°C. Increasing the temperature in the *e*-SDA process improved the asphaltene separation as indicated by a decrease of the DAO yield from 44.6% to 39.5%. This situation suggests that there is a synergistic effect between the nanoparticles and temperature that improved the DAO and pitch separation that is controlled by adsorption on the nanoparticles and the increased diffusion of asphaltenes through the feedstock to the pitch by increased thermal motion [90].

The temperature effects on DAO quality are shown in Table 2. For the SDA process, the temperature improved the DAO quality, showing that asphaltene content was reduced from 5.14% at 25°C to 3.43% at 70°C. This type of behavior was also noticed in sulfur content that was reduced from 2.33% at 25°C to 2.04% at 70°C. The DAO quality was especially related to the asphaltene content. It increased as the temperature is increased, as expected for the typical SDA process [75, 83, 84]. As noted above, the sulfur content and °API are also related to the asphaltene content, and this explains their behavior in this investigation [71, 75, 132]. For the *e*-SDA process, temperature plays the same role in improving DAO quality. The DAO asphaltene content was reduced from 4.24% at 25°C to 2.96% at 70°C. Consequently, the DAO sulfur content was also improved, decreasing from 2.02% to 1.56%. Table 2 shows that the physicochemical properties of the DAO were enhanced by the *e*-SDA process in comparison with the SDA process by increasing API gravity and by reducing both the asphaltene and sulfur contents at 70°C. Meanwhile, the solvent losses were also lower than 1.0 wt% in the processes conducted at 70°C.

Table 2. Yield and quality of the DAO after the SDA and *e*-SDA processes at 70°C using a SiO_2 nanoparticles dosage of 5 wt% and an SOR of 8 with *n*-heptane as the solvent.

Variable		Process	
		SDA	***e*-SDA**
Yield	**Pitch (%)**	51.7 ± 0.1	60.5 ± 0.1
	DAO (%)	48.3 ± 0.1	39.5 ± 0.1
DAO quality	**Asphaltene content (%)**	3.43 ± 0.01	2.96 ± 0.01
	Sulfur content (%)	2.04 ± 0.01	1.55 ± 0.01
	°API	14.39 ± 0.02	16.15 ± 0.02

Figure 5 shows the rheological properties of the DAO obtained from SDA and *e*-SDA processes at 70°C, and the estimated parameters for the Oswald-de Waele model are presented in Table 3. These results show that at 70°C, the DAO samples obtained from both processes exhibited approximately Newtonian behavior. For SDA, the Ostwald-de Waele estimated parameters were: n = 1.005 and hence K can be considered as sample viscosity equal to 18410 cP. These results from the SDA process at 70°C denote a marked improvement over those at 25°C (Table 1). The same type of response was

observed for the *e*-SDA process and can be noted in estimated parameters: n = 0.998 and K = 11699 cP. These results demonstrate that nanoparticles can improve the deasphalting process at 70°C by reducing the resulting DAO viscosity by approximately 37%.

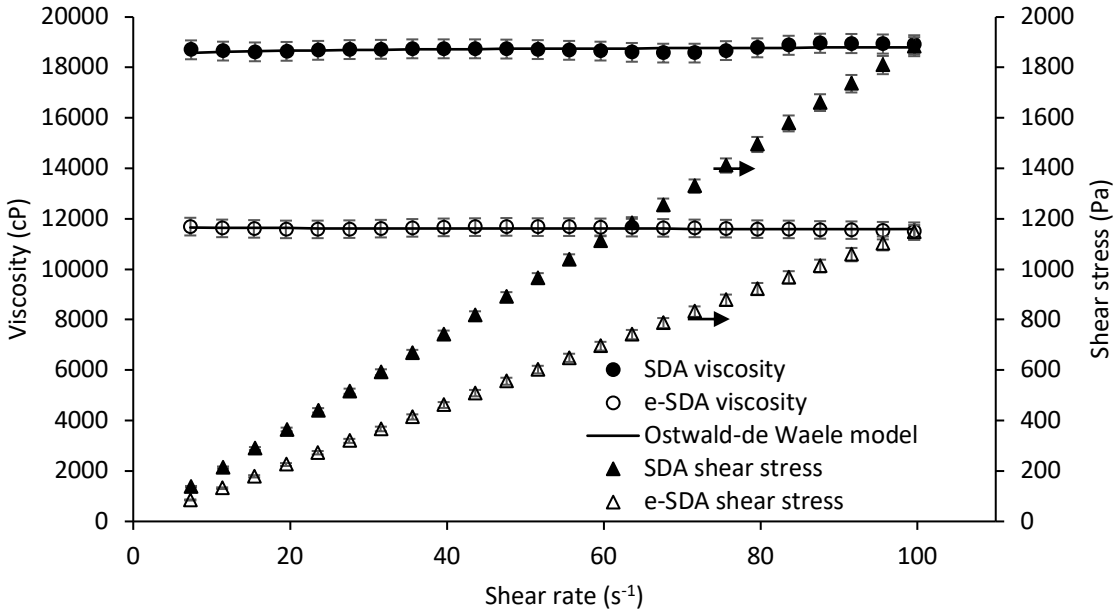

Figure 5. Viscosity and shear stress of the DAO as a function of shear rate for the SDA and *e*-SDA processes at 70°C using a SiO_2 nanoparticles dosage of 5 wt% and an SOR of 8 with *n*-heptane as the solvent.

Table 3. Ostwald-de Waele estimated parameters from rheological experiments for DAO after the SDA and *e*-SDA processes with an SOR of 8 at 70°C using SiO_2 nanoparticles and *n*-heptane as the solvent.

Parameter	SDA	*e*-SDA
***K* (cP·s^{n-1})**	18410	11699
***n* (dimensionless)**	1.005	0.998
RSME%	0.53	0.40
χ^2	0.19	0.17

1.4.3. Effect of the type of solvent

The solvent used in SDA and *e*-SDA processes has a high influence. Table 4 shows the DAO yield and quality from both processes when conducted with *n*-pentane and at 25°C a dosage of 5 wt% of SiO_2 nanoparticles. Comparing these results with those obtained when using *n*-heptane as the solvent (Figure 2), it is observed that reducing the carbon number of solvent reduced the DAO yield, and hence increased the pitch, or precipitated fraction yield [71-75, 77]. This is because increasing the molecular weight of the solvent allows it to solubilize heavier hydrocarbons [71, 77], as reflected in the solubility parameter of asphaltenes in different solvents [73]. This situation is similar in both the

SDA and *e*-SDA processes. The DAO quality also followed this same phenomenon, and reducing the solvent molecular weight increases the DAO quality [72, 74, 75]. For the SDA process, the DAO asphaltene content was reduced from 5.14% with *n*-heptane to 2.34% with *n*-pentane. The same trend occurred with sulfur content, which fell from 2.33% to 1.55%. Finally, the °API of the DAO improved considerably by increasing from 13.19 to 19.38 for *n*-heptane and *n*-pentane, respectively. This considerable improvement of the API gravity can be attributed to the resins and their influence on the de-asphalting process [74, 124-127] and how they precipitated in higher proportion when the solvent had a lower molecular weight [75].

The *e*-SDA process also exhibited improvements regarding the DAO quality as the molecular weight of solvent was reduced. The asphaltene content fell from 4.24% with *n*-heptane (Figure 2) to 2.01% with *n*-pentane (Table 4) and the same trend was observed for the sulfur content. On the DAO °API, it increased from 15.37 to 21.11 with the use of *n*-heptane and *n*-pentane, respectively. The solvent losses were also less than 1 wt%. In this sense, there seemed to be a synergetic effect on the DAO quality between the reduction of solvent molecular weight and the use of SiO_2 nanoparticles.

Table 4. Yield and quality of the DAO after the SDA and *e*-SDA processes at 25°C using SiO_2 nanoparticles at a dosage of 5 wt% and an SOR of 8 with *n*-pentane as the solvent.

Variable		Process	
		SDA	***e*-SDA**
Yield	**Pitch (%)**	56.1 ± 0.1	65.3 ± 0.1
	DAO (%)	43.9 ± 0.1	34.7 ± 0.1
DAO quality	**Asphaltene content (%)**	2.34 ± 0.01	2.01 ± 0.01
	Sulfur content (%)	1.55 ± 0.01	1.38 ± 0.01
	°API	19.38 ± 0.02	21.11 ± 0.02

Figure 6 and Table 5 summarize the rheological properties of DAO that were affected in several ways by the solvent used in the SDA and *e*-SDA processes. The results indicate nearly Newtonian behavior for the DAO obtained from both processes. These results were confirmed by the *n* parameters of Ostwald-de Waele models that equal 0.994 and 0.991, respectively. In this sense, the *K* values, interpreted as the viscosity, were 2500 cP for SDA and 2166 cP for *e*-SDA, i.e., a reduction in resultant DAO viscosity of approximately 14% occurred with the *e*-SDA process. This viscosity reduction that was exhibited when using nanoparticles could be attributed mainly to the resin fraction of the DAO that played a key role in the formation of the viscoelastic network that drastically increased the EHO viscosity [19, 22]. It is known that resins are adsorbed simultaneously with asphaltenes on the nanoparticles [117] implying that a higher amount of the resins could remain in the pitch fraction. Hence, nanoparticles may have a synergistic effect with the solvent employed, *n*-pentane in this case, by enhancing the amount of resins adsorbed and thereby inhibiting the formation of the viscoelastic network, which translates into lower energy demand for fluid transportation and processing.

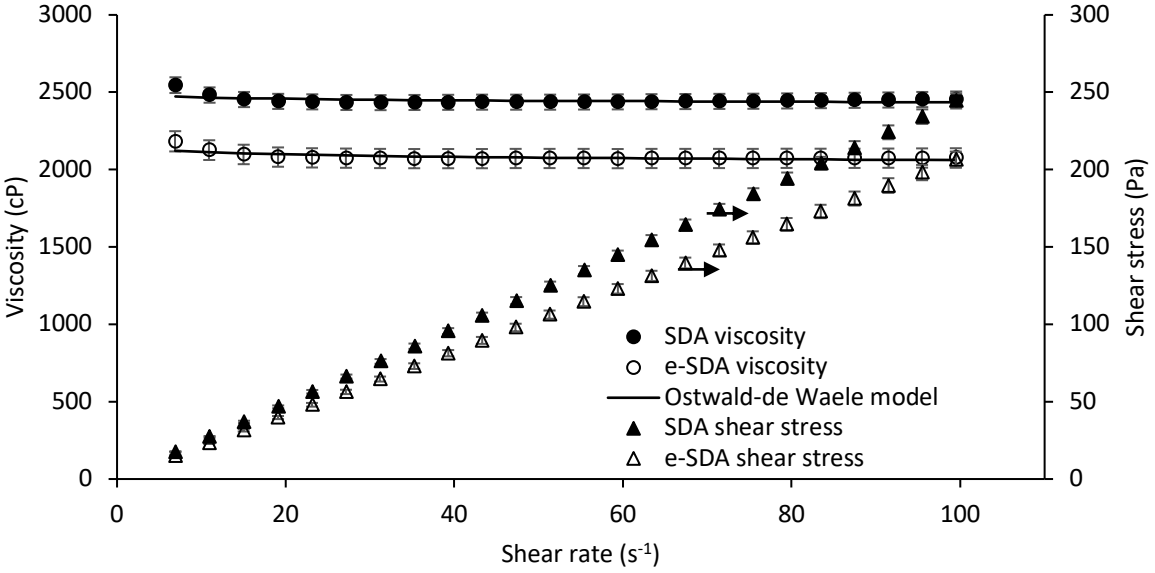

Figure 6. Viscosity and shear stress of the DAO as a function of shear rate for the SDA and *e*-SDA processes at 25°C using SiO_2 nanoparticles at a dosage of 5 wt% and an SOR of 8 with n-pentane as the solvent.

Table 5. Ostwald-de Waele estimated parameters from rheological experiments for the DAO after the SDA and e-SDA processes with an SOR of 8 at 25°C using SiO_2 nanoparticles at a dosage of 5 wt% and an SOR of 8 with n-pentane as the solvent.

Parameter	SDA	e-SDA
***K* (cP·s^{n-1})**	2500	2166
***n* (dimensionless)**	0.994	0.991
RSME%	0.69	0.68
χ^2	0.25	0.24

1.4.4. Effects of nanoparticle dosage

Using SiO_2 nanoparticles in the *e*-SDA process in dosages of 2.5 and 10 wt% of crude oil mass generated differences with the same process conducted with a fixed dosage of 5 wt%, in both DAO yield and quality. Figure 7 shows the yield of a) DAO and b) pitch as a function of the nanoparticles dosage. As can be noticed, increasing nanoparticles dosage decreases DAO yield and increases pitch yield. This behavior can be explained by the relation between adsorbate and adsorbent. Increasing the mass of the adsorbent, and hence the total surface area available for adsorption by mass unit, generates that larger amounts of asphaltenes that could be adsorbed on the nanoparticles surface. This situation leads that as SiO_2 nanoparticles dosage increase, more asphaltenes are adsorbed, and DAO yield decreases while pitch yield increases. These results are in agreeing with those reported by several authors [22, 130, 133-137], but considering the total mass of adsorbed asphaltenes instead of the relation between the mass of adsorbed asphaltenes and the mass of adsorbent.

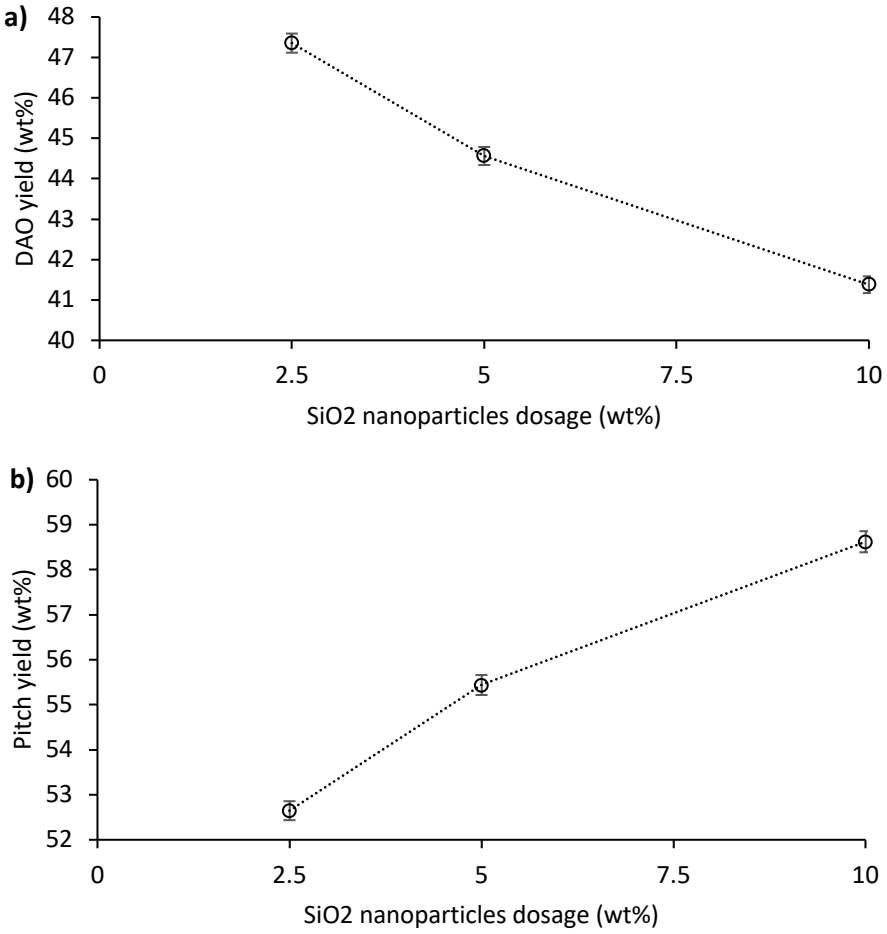

Figure 7. Effect of the SiO_2 nanoparticles dosage in (a) DAO and (b) pitch yields for the *e*-SDA process at SOR value of 8, at 25°C and using *n*-heptane as the solvent.

Figure 8 shows the DAO quality in three panels related to (a) asphaltene content, (b) sulfur content and (c) °API for *e*-SDA process at different SiO_2 nanoparticles dosage. The asphaltene content of the DAO reduces as nanoparticles dosage increases. This situation can be explained by the same situation abovementioned, increasing the total surface area for asphaltene adsorptions leads to their precipitation [22, 130, 133-137] and low the quantity of them present in the DAO. The sulfur content presents the same behavior and the explanation lays in the direct relation between asphaltene and sulfur content [75]. Additionally, Figure 8(c) shows that increasing nanoparticles dosage improved the °API values for the DAO. This result is also related to the reduction of DAO asphaltene content with the increment in nanoparticle dosage. Regarding the simulated distillation, results show that the distillable fractions for all DAO samples (at different nanoparticles dosage) were approximately 100% up to 750°C.

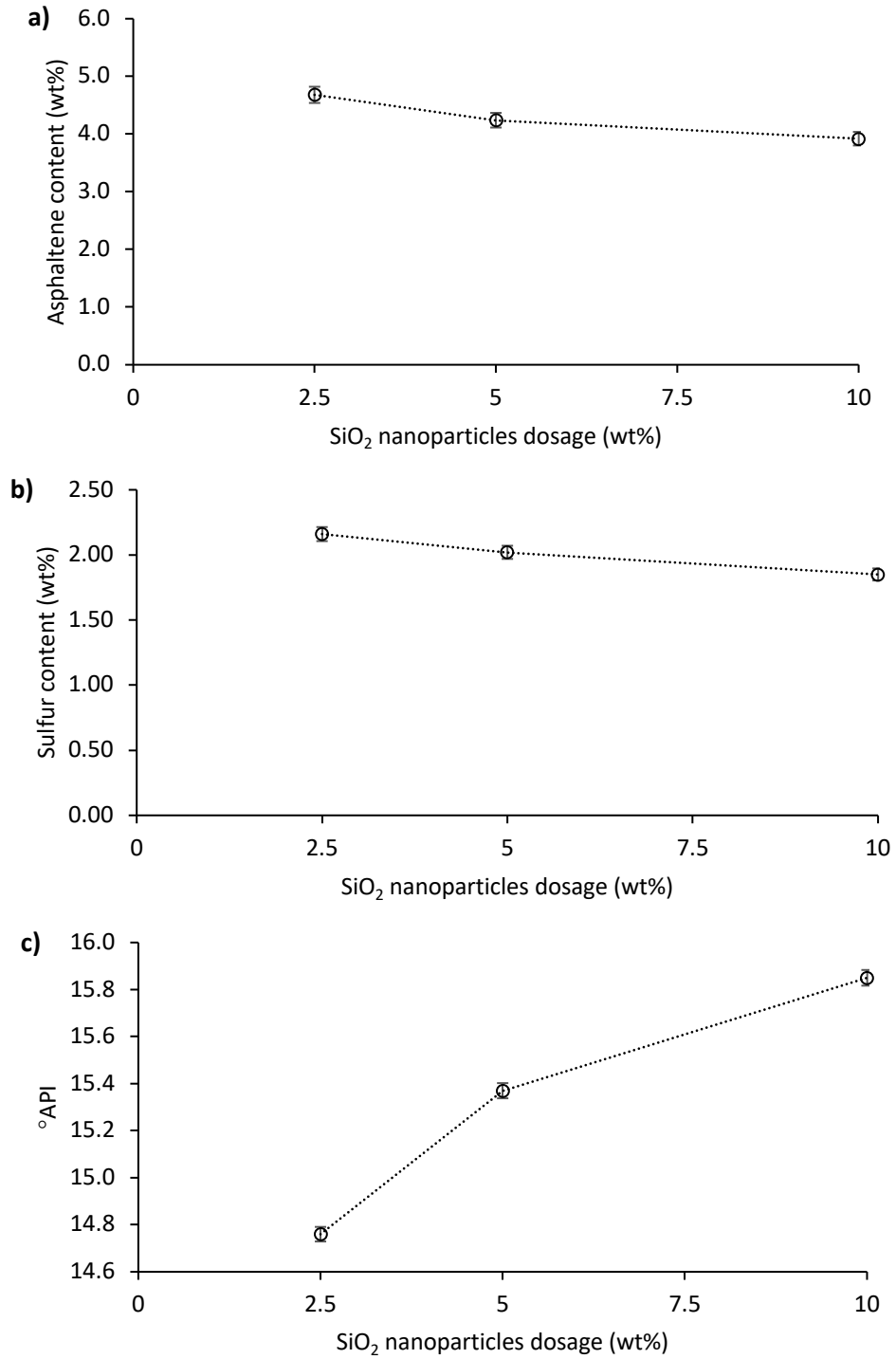

Figure 8. Effect of SiO_2 nanoparticles dosage in DAO quality related to (a) asphaltene and (b) sulfur content and (c) API gravity for the *e*-SDA processes at SOR value of 8, at 25°C and using *n*-heptane as a solvent.

Figure 9 and Table 6 summarizes the result of the rheological test carried out to the DAO obtained from *e*-SDA process with SiO_2 nanoparticles at dosages of 2.5 wt% and 10 wt%. Both DAO samples obtained with the 2.5 and 10 wt% dosages exhibited a Newtonian behavior. For a dosage of 2.5 wt%,

the *n* value is 1.001 and *K* value is 15802 cP·s^{n-1}. The last parameter indicates a viscosity of 15802 cP. For a SiO_2 nanoparticles dosage of 10 wt% the DAO shows *n* value equal to 0.996 and *K* value of 9982 cP·s^{n-1}, showing a viscosity of 9982 cP. It can be noticed that increasing nanoparticles dosage improves the rheological behavior of DAO considering these results and those obtained for a dosage of 5 wt%. Increasing the nanoparticles dosage from 2.5 to 5 wt% generates a viscosity reduction of 25% while raising the dosage from 5 to 10 wt% reduces the viscosity in 16%. Hence, a dosage of 5 wt% can be considered adequate as increasing in the DAO quality by rising nanoparticles dosage to 10 wt% are not as significative as those obtained when the dosage is increased from 2.5 to 5 wt%.

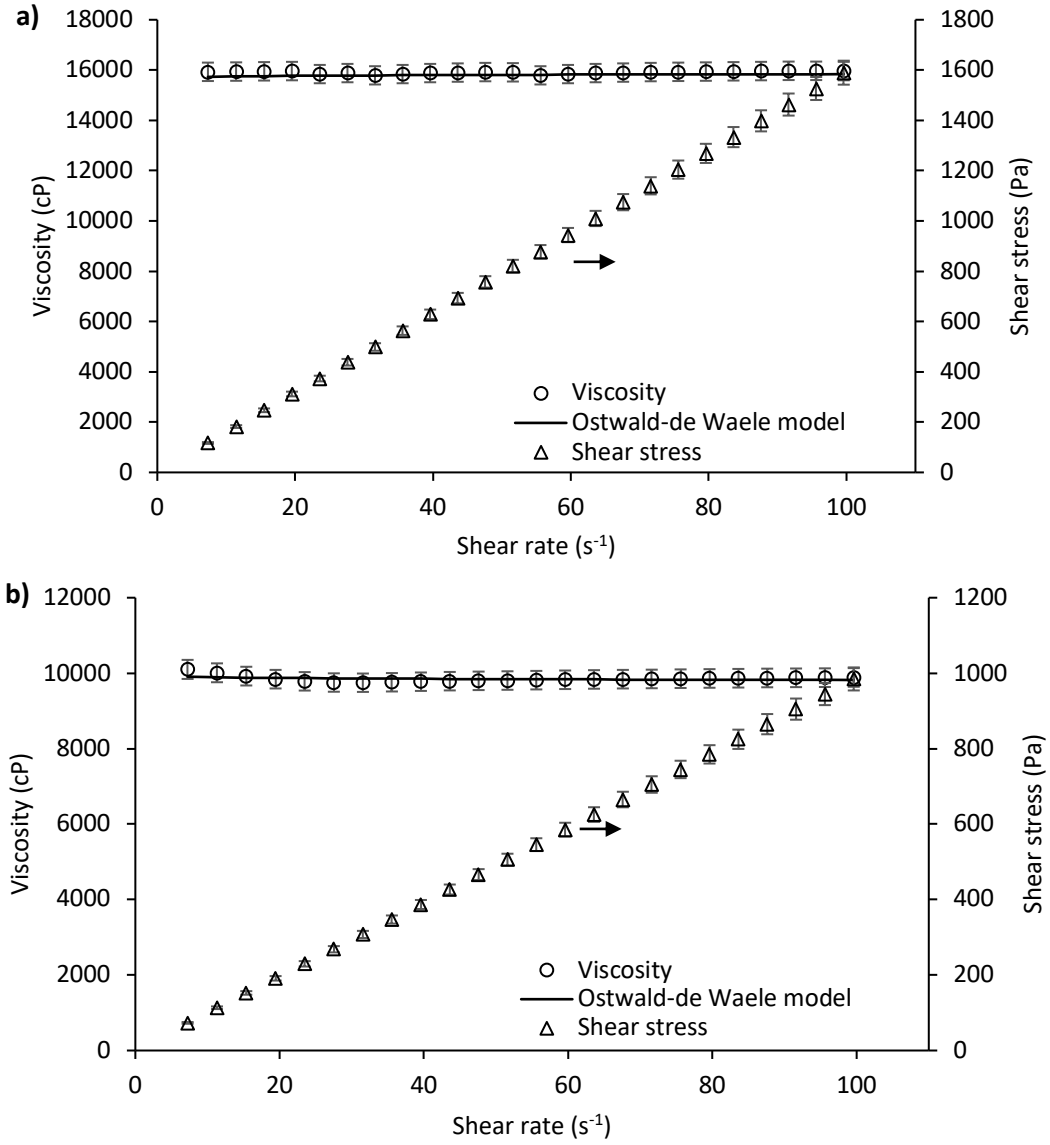

Figure 9. Viscosity and shear stress as a function of shear rate for SiO_2 nanoparticles dosages of (a) 2.5 and (b) 10 wt% at SOR = 8, 25°C and using *n*-heptane as the solvent.

Table 6. Ostwald-de Waele estimated parameters for rheological experiments on DAO after *e*-SDA with SiO_2 nanoparticles dosage of 2.5 and 10 wt% at SOR = 8, 25°C and using *n*-heptane as the solvent.

Nanoparticles dosage (wt%)	Parameter			
	K **(cP·s^{n-1})**	***n*** **(dimensionless)**	**RSME%**	**χ^2**
2.5	15802	1.001	0.58	0.19
10	9982	0.996	0.69	0.27

1.5. Partial conclusions

The efficiency of a typical SDA process was successfully increased at laboratory-scale conditions by the inclusion of nanoparticles in systems with different solvent to oil ratios, temperatures, types of solvent and dosage. It was found that the use of nanoparticles reduces the DAO yield in comparison with the traditional SDA process, resulting in a higher quality product. The reason is the adsorption phenomena of the asphaltenes and the nanoparticles and how the former are transferred from the DAO fraction to the pitch fraction. Regarding the DAO quality, the *e*-SDA process demonstrated to be a more suitable alternative regarding the asphaltene and sulfur contents, API gravity and rheological properties. The improvement of the rheological properties is desirable because this leads to savings of energy and transportation efforts when the DAO has lower viscosities.

Finally, it is worth noting that this study was focused on DAO quality in the *e*-SDA process and there is important in future investigations to assess the improvements of the catalytic thermal decomposition of the pitch when adding nanoparticles in the *e*-SDA process. This subject is important because of the energy costs involved in this process and its efficiency, considering that used solvent and nanoparticles are can be recycled. It is expected that this knowledge will provide a suitable alternative for the enhancement of heavy and extra-heavy oil processing operations, particularly as related to the transportation process.

2. Effect of the nanoparticle's chemical nature on DAO quality and catalytic oxidation of pitch

The solvent de-asphalting (SDA) process is one of the most used techniques in the oil & gas industry for on-site upgrading of heavy and extra-heavy oils [8, 69]. It consists of using paraffinic solvents for the physical separation of two phases, the deasphalted oil (DAO) and the pitch, considered a residue. Recently, there was proposed an enhanced solvent de-asphalting (*e*-SDA) process that uses nanotechnology to improve DAO quality [70]. This innovative technique has proven the effectiveness of silica nanoparticles in separating asphaltenes from DAO to pitch selectively. The above also allowed to obtain DAO samples with higher °API, lower asphaltene and sulfur content, and better rheological conditions than those obtained for the traditional SDA process. These results were obtained for all the evaluated operation conditions like solvent to oil ratio (SOR), type of solvent, temperature, and even nanoparticle dosage.

At this point, the developed *e*-SDA process had only proven nanoparticles' potential in obtaining improved-quality DAO samples despite the operation conditions [70]. It is necessary to delve into the interactions between nanomaterials and crude oil components, especially the asphaltenes. In this sense, this chapter assesses the adsorbent-adsorbant relationship between the couple nanoparticle-asphaltenes and its impact on DAO quality. To make it, a fully deasphalted oil was obtained and characterized, considering its properties as the best that a DAO sample can achieve. There were also selected three different chemical nature nanoparticles widely studied, like silica [30, 70, 114, 115, 138-147], alumina [113, 146, 148-150] and cerium [151-153]. The first one, was of two different sizes to deepen its effect on the *e*-SDA process. The obtained adsorption isotherms were fitted to the SLE model [154] to understand the adsorption affinity, the propensity of asphaltenes to be adsorbed in multiple layers onto the nanoparticle's surface and their maximum adsorption capacity. The last with significant implications for the DAO quality of the samples obtained with the *e*-SDA process.

On the other hand, in Figure 1 of chapter 1, there was a product of the *e*-SDA process that has not been yet studied: the pitch. Pitch is considered a low valuable residue. In the best scenarios is used as low-grade fuel, road-packing material, or to produce hydrogen and heat by gasification processes [69, 75, 155]. However, nanoparticles have also shown excellent behavior as catalysts of the asphaltenes [30, 139, 140, 150-152, 156] and resins [157], the main components of the pitch. Thus, this chapter also evaluated the nanoparticle role in enhancing the *n*-C_7 asphaltene catalytic oxidation process. Also, the oxidative decomposition of SDA obtained pitch was compared to those obtained in the presence of nanoparticles showing their potential. There was used the method followed by several authors and consisted of heating the samples from 30 °C to 700 °C [30, 112, 138-140].

2.1. Materials and methods

2.1.1. Materials

A Colombian extra-heavy crude oil (EHO) was used for the traditional and all the enhanced solvent deasphalting processes. Its properties are specified in Table 7. Commercial nanoparticles of fumed silica (SiO_2) of two different sizes (Sigma-Aldrich, St. Louis, MO, USA), alumina (Al_2O_3) (Petroraza SAS, Sabaneta, Colombia) and Ceria (CeO_2) (Nanostructured & Amorphous Materials, Houston, TX, USA) were used. *n*-heptane (99%, Sigma-Aldrich, St. Louis, MO, USA) was used for *n*-C_7 asphaltene extraction, SDA, and *e*-SDA processes. *n*-C_7 asphaltenes were dissolved in toluene (99.5%, Merk KGaA, Germany) for preparing a stock solution of 2000 mg/L for adsorption batch experiments.

Table 7. Properties of EHO sample

Property		Value
°API		6.32
Sulfur content (wt%)		3.91
Distillable fraction (wt%)		62.46
Conradson carbon residue (wt%)		37.54
SARA	Saturates (wt%)	14.26
	Aromatics (wt%)	24.38
	Resins (wt%)	47.80
	Asphaltenes (wt%)	13.56

2.1.2. Methods

2.1.2.1. Nanoparticles characterization

Commercial nanoparticles of different chemical nature were characterized through their hydrodynamic diameter (dp_{50DLS}), surface area (S_{BET}) and thermal stability. The first one was determined with dynamic light scattering (DLS) measurements. Nanoparticles were dispersed at various concentrations in deionized water using an ultrasonic bath. The measure was made until the size obtained was constant for low concentrations of nanoparticles in liquid to avoid aggregation. Finally, the hydrodynamic diameter was calculated using the Stokes-Einstein equation in a NanoPlus-3 from Micromeritics (Norcross, Georgia, USA) [158, 159].

On the other hand, the superficial area of the nanomaterials was measured according to the BET method [160, 161] using N_2 physisorption at -196°C using an Autosorb-1 from Quantachrome (Florida, USA). Finally, considering functionalized nanoparticles' application in enhanced solvent deasphalting processes, it is essential to evaluate their thermal stability through thermogravimetric analyses (TGA). These analyses were carried out with a TGA analyzer Q50 from TA Instruments, Inc.

(New Castle, DE, USA). The samples were dried overnight in a vacuum oven and then heated from 30°C to 700°C at a fixed heating rate of 10°C/min in an airflow constant of 100 mL/min

2.1.2.2. *n*-C_7 asphaltene extraction

Solid *n*-C_7 asphaltene was extracted from the crude oil by adding an excess amount of *n*-heptane following a standard procedure [30, 112]. Briefly, *n*-heptane in excess was added to the crude oil in a volume ratio of 40 to 1. The mixture was then sonicated for 2 h at room temperature (25°C) and stirred for 24 h at 300 rpm. The black precipitates formed at the bottom, and the precipitate fraction were filtered through an 8 µm Whatman filter paper and washed with *n*-heptane. These asphaltene samples were centrifuged at 5000 rpm for 15 min. The obtained cake was washed with *n*-heptane until the color of asphaltenes became shiny black, and the *n*-heptane passing through the filter kept its color. Finally, the asphaltenes were fined and homogenized using a mortar and left to dry in a vacuum oven at 25°C for 24 h.

2.1.2.3. Completely deasphalted oil extraction

Completely deasphalted oil (cDAO) was obtained by mixing EHO and *n*-heptane with a mass ratio of 40 to 1 [21]. The mixture was stirred at 300 rpm inside airtight vials at 25 °C for 24 h. The mixture was sonicated every 15 min to disperse the particles of precipitated asphaltenes. With this process, there was achieved *n*-C_7 asphaltene precipitation, and those were separated from cDAO through filtration with an 8 µm Whatman paper filter. At this point, heating the mixture at 65 °C allows the separation of used *n*-heptane. The cDAO is ready when its weight is equal to EHO oil weight minus the one for the extracted *n*-C_7 asphaltenes.

2.1.2.4. Equilibrium adsorption isotherms

Extracted *n*-C_7 asphaltenes were re-dissolved in toluene to prepare a stock solution with an initial concentration of 2000 mg/L. Solutions of *n*-C_7 asphaltenes with initial concentrations between 100 and 2000 mg/L were prepared by diluting the stock solution. Experimental batch-mode adsorption equilibrium was found with a fixed mass of nanoparticles added to model heavy oil solutions with initial asphaltene concentration (C_i) between 100 and 2000 mg/L. The ratio of nanoparticles to heavy oil solution was 100 mg to 10 mL. The different mixtures were stirred at 200 rpm at 25°C for 24 h seeking to ensure adsorption equilibrium. For all the samples, the nanoparticles containing adsorbed asphaltenes were separated from the mixture by centrifugation for 5 min at 4000 rpm using a Hermle Z 306 Universal Centrifuge (Labnet, NJ, USA), and the supernatant was decanted. The residual concentration of asphaltenes in the supernatant was measured at a wavelength of 295 nm using a Genesys 10S UV-vis spectrophotometer (Thermo Scientific, Waltham, MA, USA) [151]. Finally, the amount of n-C_7 asphaltene adsorbed q (mg/m^2) was estimated from the mass balance shown in Equation 2:

Equation 2. $$q = \frac{(C_i - C_E)}{(A \cdot M)}$$

Where, C_i (mg/L) is the initial concentration of *n*-C_7 asphaltenes in solution, while C_E (mg/L) is the equilibrium concentration of these, and A (m^2/g) is the measured surface area per unit mass of the nanoparticles. Worth mentioning that uncertainty of absorbance measurements implies a deviation of 0.05 mg/L and 0.001 mg/m^2 in the calculation of C_E and q, respectively.

2.1.2.5. DAO separation and characterization

The procedure followed to separate the DAO from the pitch was previously described in chapter 1, numeral 1.2.2. That section also detailed the methods used to determine the DAO sample's yield and quality through °API, asphaltene content, sulfur content, distillable fraction, Conradson carbon residue, and rheological behavior. Additionally, their SARA fractions were measured with a microdeasphalting technique using a TLX-FID/FDP Iatroscan MK6 (Iatron Laboratories Inc., Tokyo, Japan) coupled with thin layer chromatography following the IP 469 standard [162].

2.1.2.6. *n*-C_7 asphaltene and pitch oxidation in the absence and presence of nanoparticles

The nature of the proposed *e*-SDA process leads to a catalytic decomposition of the pitch in an oxidative atmosphere in the presence of air. Thus, the evaluation of catalytic oxidation was selected over other alternatives such as steam gasification and pyrolysis. The efficiency of nanomaterials in the reduction of the decomposition temperature of *n*-C_7 asphaltene has been widely assessed through thermogravimetric analyses [30, 112, 138-140]. The oxidation of *n*-C_7 asphaltenes in the absence and presence of nanoparticles was carried out using a Q50 TGA analyzer (TA Instruments, Inc., New Castle, DE, USA). The samples were heated from 30 °C to 700 °C with a constant airflow of 100 mL/min at three heating rates of 5, 10 and 20 °C/min. The sample mass was fixed at 5 mg to avoid diffusion limitations [112]. The adsorbed amount of *n*-C_7 asphaltenes onto selected nanoparticles was 0.2 mg/m^2. However, this relation between adsorbent and adsorbant can't be kept for the pitch evaluation. It can be explained by the *e*-SDA process carried out with a fixed 5 wt% of evaluated nanoparticles and its mass ratio regarding pitch, depending on the quantity of this produced.

2.2. Modeling

2.2.1. Adsorption isotherm with the solid-liquid equilibrium (SLE) model

To model the adsorption phenomena between the support nanoparticles and the functionalized ones, the solid-liquid equilibrium model (SLE) was selected. This model is based on a theoretical explanation of the adsorption of self-associated asphaltenes on solid surfaces [154], based on the theory of association proposed by Talu and Maunier [163]. The following equations describe the SLE model:

Equation 3. $$C_E = \frac{\Psi H}{1-K\Psi} e^{\left(\frac{\Psi}{q_m \cdot A}\right)}$$

with

Equation 4. $$\Psi = \frac{-1+\sqrt{1+4K\cdot\xi}}{2K}$$

Equation 5. $$\xi = \left(\frac{q_m \cdot q}{q_m - q}\right)$$

Where q (mg/m^2) is the amount of n-C_7 asphaltene adsorbed, q_m (mg/m^2) is the maximum adsorption capacity, A (m^2/mg) is the measured S_{BET} per unit mass of nanoparticles and C_E (mg/g) is the equilibrium concentration of n-C_7 asphaltenes in the solution. K (g/g) is the reaction constant related to the degree of association between the n-C_7 asphaltenes on the surfaces of the nanoparticles, and H (mg/g) is Henry's law constant linked to the preference of n-C_7 asphaltenes for being in the liquid phase or the adsorbed phase [154]. The correlation coefficient (R^2) and the root-mean-square error (RMSE%) were used to estimate the goodness of fit with the Solver feature in Excel Professional Plus 2019 [164, 165]. Both were used in the following sections.

2.2.2. Estimation of activation energy (OFW)

The Ozawa-Flynn-Wall method (OFW) can estimate the effective activation energies [166, 167], assuming that for a constant reaction conversion, the reaction rate is a function of the temperature and the state as can be seen in Equation 6. This procedure uses the data obtained after TGA experiments performed at different heating rates.

Equation 6. $$\frac{d\alpha}{dt} = K_\alpha \exp\left(-\frac{E_{\alpha OFW}}{RT}\right) f(\alpha)$$

Where, K_α (1/s) is the pre-exponential factor, $E_{\alpha OFW}$ (kJ/mol) is the effective activation energy for a constant conversion, R (J/mol·K) is the ideal gas constant, T (K) is the reaction temperature, and α is the reaction conversion described by Equation 7.

Equation 7. $$\alpha = \frac{m_0 - m_T}{m_0 - m_f}$$

with m_0 as the initial mass of the sample; m_f the final mass of the sample and m_T the mass at a given temperature. When the heating rate is defined as $\beta = dT/dt$ and integrating can be obtained the Equation 8. Finally, the effective activation energy can be estimated from the slope of the linear fit from the plot of log (β) against 1/T using the Doyle approximation [168], as described in Equation 9 [169]:

Equation 8. $$g(\alpha) = \int_0^{\alpha} \frac{d\alpha}{f(\alpha)} = \int_0^{T} \frac{K_\alpha \exp(-E_\alpha/RT)}{\beta} dT$$

Equation 9. $$log(\beta) = log\left(\frac{K_\alpha E_\alpha}{Rg(\alpha)}\right) - 2.315 - 0.4567\frac{E_\alpha}{RT}$$

2.3. Results

2.3.1. Commercial nanoparticles characterization

Three nanoparticles of different chemical nature were used: fumed silica of 7 nm (Si7) and 200 nm (Si200), alumina (Al) of 35 nm and cerium (Ce) of 20 nm, according to the producer's reported particle size. The measured properties of these nanoparticles are presented in Table 8. It can be noticed that Si7 and Si200 have the highest surface area (S_{BET}), followed by Al and Ce nanoparticles. Also, the particle diameter increased in the mentioned order except for Si200, which showed the most oversized hydrodynamic diameter (dp_{50DLS}). According to TGA analysis, all commercial nanoparticles are thermally stable and didn't present mass losses until 700 °C. By the nature of the *e*-SDA process that uses a fixed wt% of nanoparticles, it seems clear that to higher S_{BET}, the greater the available surface to asphaltene adsorption and separation. It is worth mentioning that the Si7 nanoparticle of chapter 1 was the same used in this section and below with approximately the same S_{BET}.

Table 8. Measured values of hydrodynamic diameter and surface area (S_{BET}) for Si7, Si200, Al and Ce nanoparticles.

Nanoparticle	dp_{50DLS} ± 1 (nm)	S_{BET} ± 0.5 (m^2/g)
Si7	12	387.9
Si200	207	184.2
Al	39	122.0
Ce	21	68.2

2.3.2. Completely deasphalted oil

Following the previously described methodology, a completely deasphalted oil (c-DAO) was obtained. It is essential to know its properties because an ideal deasphalting process should lead to the complete extraction of *n*-C_7 asphaltene, which would be the pitch's main component. Thus, the remaining crude oil components (saturates, aromatics and resins) should be the *c*-DAO. In this sense, the key to the total separation of the *n*-C_7 asphaltenes was the excess of *n*-heptane used at a SOR of 40, which guarantees the precipitation of these and their separation of resins and the rest of the crude oil components [21]. After this procedure, the obtained *c*-DAO yield was the sum of the saturates, aromatics and resins with a value of 86.44 wt%. Hence, the pitch yield was equal to crude oil *n*-C_7 asphaltene content, with 13.56 wt%.

Regarding *c*-DAO quality, Figure 10 presents its SARA fractions. It can be noticed that these fractions are approximately equivalent to those observed for crude oil, resizing considering the extracted *n*-C_7 asphaltenes. The sulfur content was determined as 1.09 wt%. This result is coherent with the present amount of resins, which can have this element nearly in the same proportion of *n*-C_7 asphaltenes [170, 171]. In this sense, the Conradson carbon residue showed the same behavior with a value of 2.77 wt%, and the distillable fraction was 97.23 wt% [170], while the °API measured was 20.93. Finally, Figure 11 and Table 9 reported that the expected viscosity for *c*-DAO was 4 315 cP with a nearly Newtonian behavior [121, 122]. These results are coherent with those reported by Taborda et al. [21], who extracted the DAO for heavy oil. They found that crude oil viscosity values, higher than 100 000 cP and exhibiting a non-Newtonian behavior, reduced to around 3 000 cP independent of the shear rate.

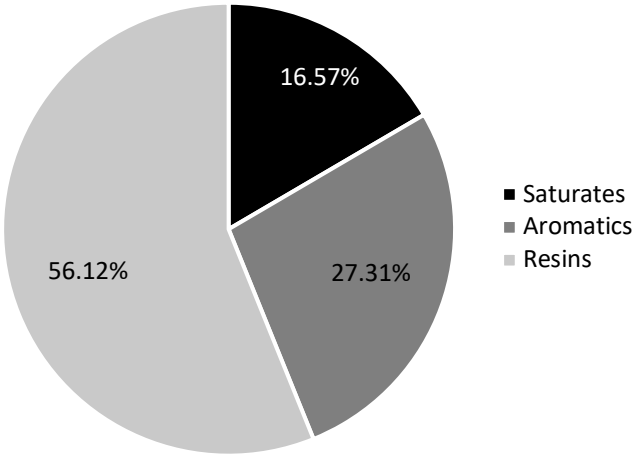

Figure 10. SARA fractions for *c*-DAO obtained with a SOR of 40 of *n*-heptane.

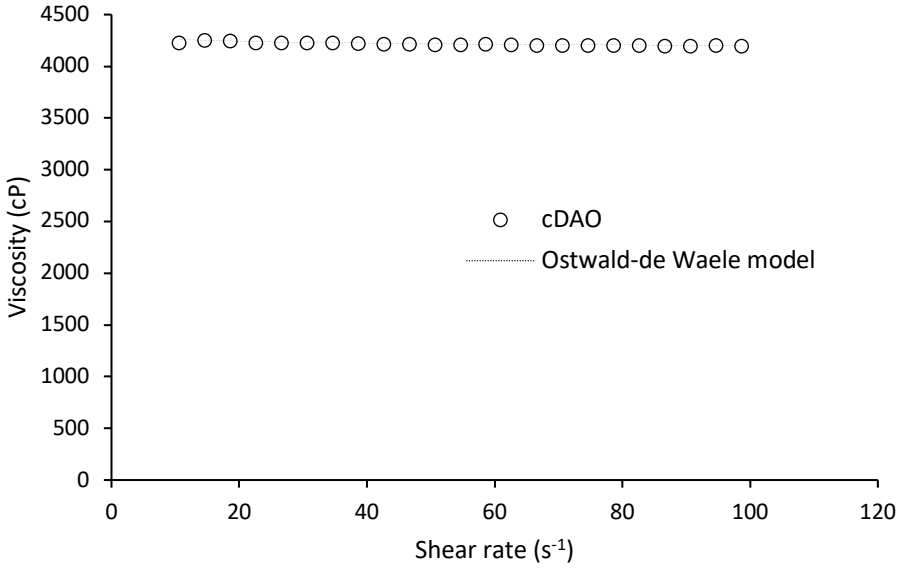

Figure 11. Viscosity as a function of shear stress for *c*-DAO obtained with a SOR of 40 of *n*-heptane.

Table 9. Oswald-de Waele estimated parameters for rheological experiments onto *c*-DAO obtained with a SOR of 40 of *n*-heptane.

Sample	$K \pm 20$ (cP·s^{n-1})	$n \pm 0.003$ (dimensionless)	R^2	RSME%
cDAO	4 315	0.994	0.985	6.2

2.3.3. *n*-C_7 asphaltene adsorption

The nature of the proposed *e*-SDA processes and its primary objective of improving DAO quality are directly related to reductions in its asphaltene content [70]. Hence, silica [30, 70, 114, 115, 138-147], alumina [113, 146, 148-150] and cerium [151-153] nanoparticles were chosen because their behavior in asphaltenes adsorption has been widely studied in the literature. For silica, two different particle sizes were evaluated to estimate their impact on the *e*-SDA process. Thus, support nanoparticles were assessed through their asphaltene adsorption capacity and properties. Figure 12 presents the experimental data of adsorption isotherms of *n*-C_7 asphaltenes onto Si7, Si200, Al and Ce nanoparticles with the fit to the SLE model.

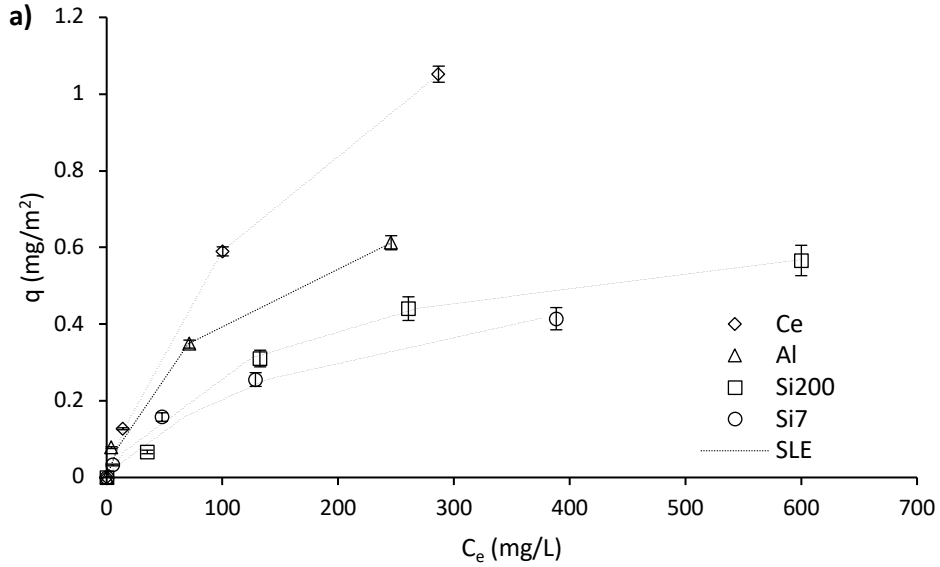

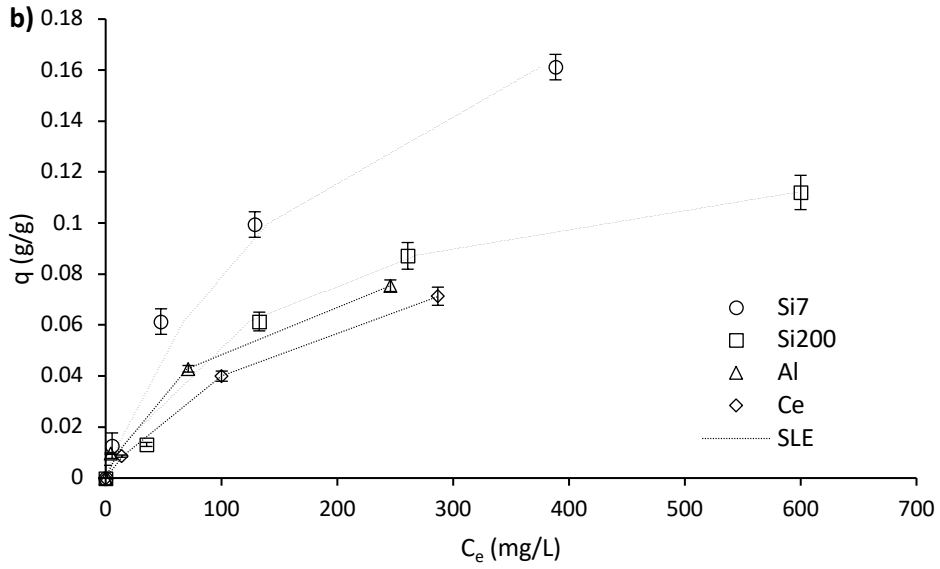

Figure 12. Adsorption isotherms of *n*-C_7 asphaltenes onto Si7, Si200, Al and Ce nanoparticles at 25 °C expressed in (a) mg/m^2 and (b) g/g.

The obtained adsorption isotherms are type Ib [172] and decrease following the order Ce > Al > Si200 > Si7 in mg/m^2. The measured asphaltene adsorption points were consistent with the results published by other authors [30, 70, 113-115, 138-153]. Nonetheless, as previously mentioned in chapter 1, the *e*-SDA process is carried out with a fixed wt% of nanoparticles related to oil mass [70]. For this reason, it would make more sense to compare the different selected nanoparticles in g/g, as presented in panel b of Figure 12. Thus, the *n*-C_7 asphaltene adsorption decreases in the order Si7 > Si200 > Al > Ce due to their specific surface areas.

These results were corroborated with the obtained parameter of the SLE model presented in Table 10. The value of *H* increased in the order Si7 < Al < Si200 < Ce, indicating that the adsorption affinity was higher for Si7 nanoparticles. This result was significant, but not as much as the observed values of q_m, which is related to the maximum asphaltene adsorption capacity of the nanoparticles [154]. This capacity would surely be the most important property for selecting the best commercial nanoparticle, considering that asphaltene adsorption capacity leads to obtaining better DAO samples, as seen below. In this sense, q_m decreased in the order Si7 > Si200 > Ce > Al. This observation was also noticed by the estimated q_m parameter of the SLE model for silica and alumina nanoparticles in Montoya et al. [154], despite that part of the work toked experimental data reported in the literature with different *n*-C_7 asphaltene sources. The obtained results also agree with those reported by Madhi and colleagues [146], which concluded that silica nanoparticles could adsorb more asphaltenes than alumina nanoparticles. Related to cerium nanoparticles, the obtained q_m parameter is coherent with others reported in the literature and is smaller than observed for silica nanoparticles [152]. At this point, Si7 nanoparticles presented the best result in maximum *n*-C_7 asphaltene adsorption affinity and capacity (g/g). These results can be explained by the presence of Si-OH functional groups on the surface of this material and their interactions with the functional

groups present in the asphaltene structure [30, 134]. Finally, the observed difference between Si7 and Si200 can be attributed to the fact that smaller particle sizes propitiate a greater extent of the dispersion degree of the material [150].

Table 10. Estimated values of the SLE model parameters for the adsorption isotherms of *n*-C_7 asphaltenes onto Si7, Si200, Al and Ce nanoparticles at 25 °C.

Nanomaterial	H ± 0.02 (mg/g)	K ± 0.08 (g/g) x 10^{-3}	q_m ± 0.01 (g/g)	R^2	RSME%
Si7	0.92	4.38	0.43	0.994	1.5
Si200	1.17	0.44	0.23	0.998	1.3
Al	1.05	0.01	0.18	0.999	0.4
Ce	1.85	5.42	0.21	0.999	0.1

2.3.4. DAO yield and quality

This section presents the effect of the nanoparticle chemical nature on the DAO yield and quality in the *e*-SDA process. Figure 13 shows DAO and pitch yields for SDA and *e*-SDA processes using *n*-heptane with a SOR of 8 and nanoparticle dosage of 5 wt% at 25°C for Si7, Si200, Al and Ce. It can be noticed that the SDA process obtained the highest DAO yield and, therefore, the lowest pitch yield. The presented results were consistent with the observed in chapter 1 [70] and obey the adsorption phenomena between all evaluated nanoparticles and the *n*-C_7 asphaltenes that improve their separation from the DAO to the pitch. There can also be noticed for the *e*-SDA process that DAO yield decreased in the order Al > Ce > Si200 > Si7, which is the same order as the increasing pitch yield. These results can be explained in Figure 14, which plots the q_m parameter of adsorption isotherms versus DAO yield with a great linear fit, evidencing the inverse relationship between them. In this sense, DAO yield for the *e*-SDA process carried out with different nanoparticles' chemical nature is explained better by the maximum asphaltene adsorption capacity of these than their adsorption affinity, related to the *H* parameter.

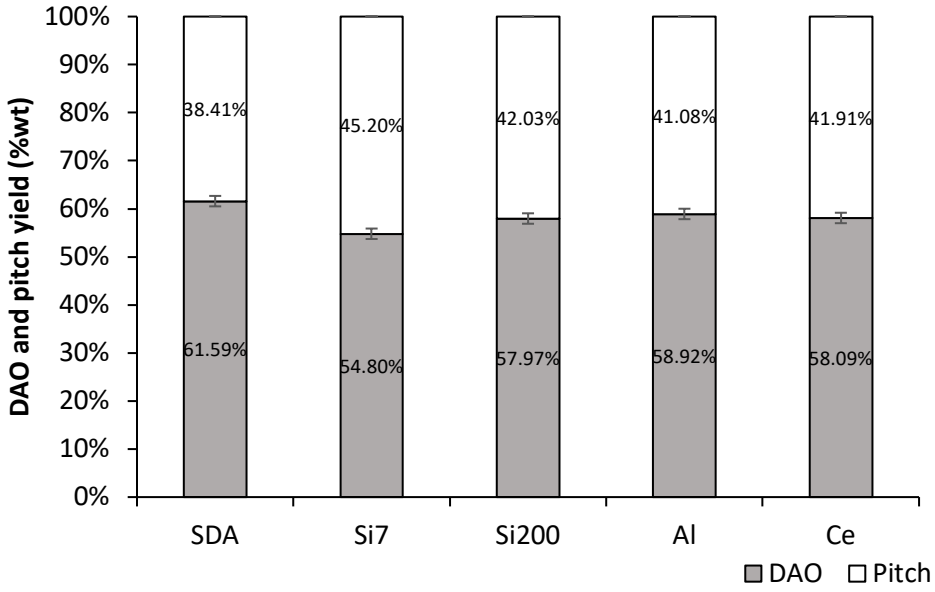

Figure 13. DAO and pitch yields for the SDA and *e*-SDA processes for Si7, Si200, Al and Ce at dosages of 5 wt% and *n*-heptane as the solvent with a SOR of 8 at 25°C.

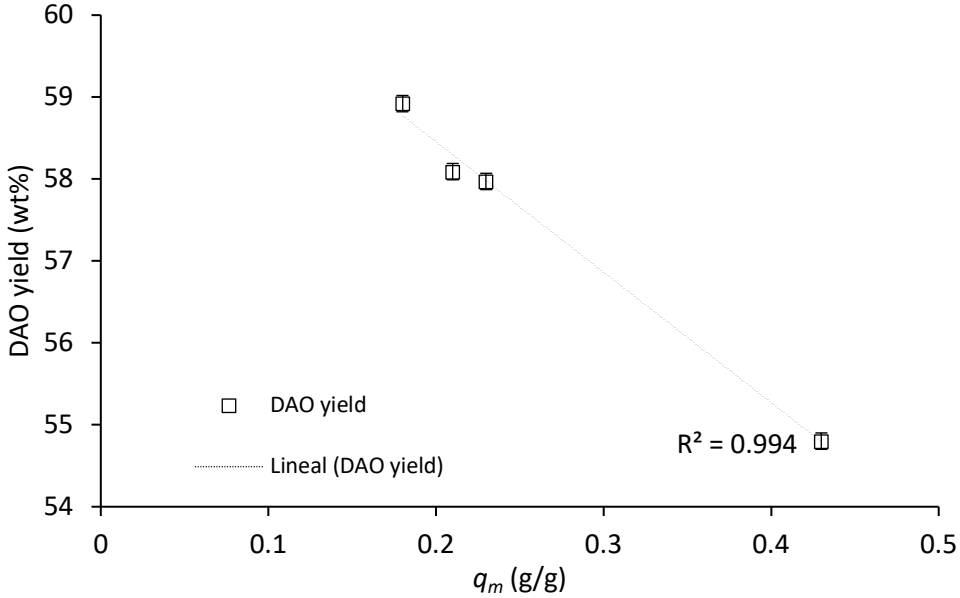

Figure 14. DAO yield (wt%) for the *e*-SDA process carried out with Si7, Si200, Al and Ce vs. q_m (g/g) parameter for estimated SLE model and linear adjustment.

Regarding DAO quality, there were measured to the different DAO samples their SARA fractions, API gravity, sulfur content, rheological behavior, distillable fraction and the Conradson carbon residue. Figure 15 presents the obtained SARA fractions for the SDA and *e*-SDA processes carried out with different chemical nature nanoparticles. It can be noticed that the wt% of saturates and aromatic compounds are approximately constant for all samples. The same results were obtained for resins that constituted about 66 wt% of DAO samples, which can be explained by the solvating power of

n-heptane [44], which solubilizes the resins and make them unable to peptize the asphaltenes [124-127]. In this way, solubilized resins pass to the DAO. This situation also leads to asphaltene aggregation and precipitation [74, 124-127]. The asphaltene content can be 25 % smaller in the processes carried out with nanoparticles than in the SDA process [70]. For used nanoparticles, the obtained DAO asphaltene content decreased in order Al > Ce > Si200 > Si7, in agreement with the observed relationship between q_m parameter and DAO yield. However, it is crucial to clarify that the difference between the asphaltene wt% for the last three nanoparticles wasn't significant. In this sense, considering the relationship between the asphaltene and sulfur content [75], while the former was reduced, the latter also did so in a similar proportion [70, 75].

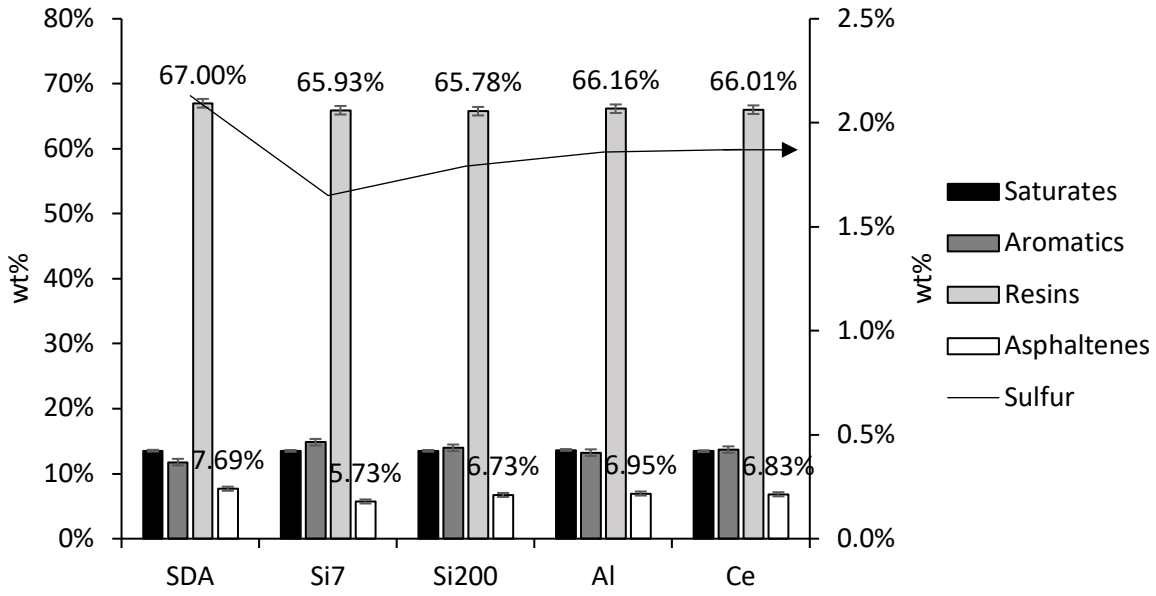

Figure 15. SARA fractions and sulfur content for the SDA and *e*-SDA processes using Si7, Si200, Al and Ce at 5 wt% and *n*-heptane as the solvent with a SOR of 8 at 25°C.

Figure 16 shows the behavior of API gravity and Conradson carbon residue for the DAO samples obtained in the absence and presence of nanomaterials. The measured °API for Si7 was the highest, 20% above than observed for the SDA process. This value is the closest to the maximum possible °API corresponding to *c*-DAO, reaching 75.8 % of its value, and is more than twice the °API of the used EHO. These results agree with the previously reported [70]. For all nanoparticles used in the *e*-SDA process, the °API values increase compared to traditional deasphalting methods. They do it following the same previously described trend. Figure 16 shows that the Conradson carbon content of DAO samples has the same inverse order of q_m parameter shown by the asphaltene wt%. These results make sense as the asphaltenes are responsible for the Conradson carbon content, and the literature has reported this type of relationship between these two elements [173].

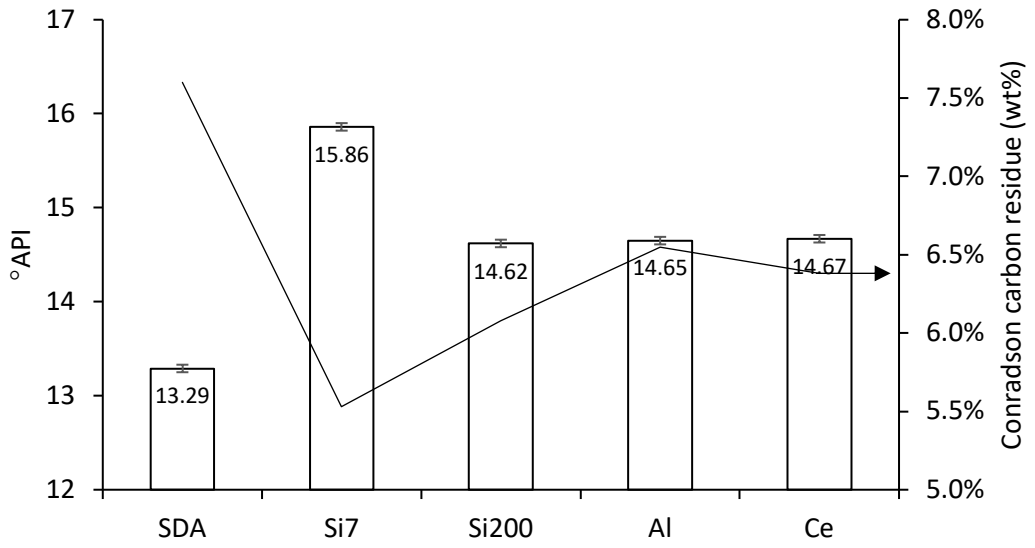

Figure 16. DAO API gravity and Conradson carbon residue for the SDA and *e*-SDA processes using Si7, Si200, Al and Ce at 5 wt% and *n*-heptane as the solvent with a SOR of 8 at 25°C.

The last component evaluated to determine the DAO quality was the rheological behavior. Figure 17 presents the viscosity measurements and the fitting with the Oswald-de-Waele model for different shear rates. Table 11 shows the estimated parameters of the mentioned model. It can be noticed for all samples that the value of the *n* parameter is close to 1, allowing all to present a nearly Newtonian behavior [121, 122]. With this result, the value of the parameter *K* can be considered as the expected viscosity. For all deasphalting processes, the viscosity is considerably smaller than previously observed for crude oil. There also can be noticed that all *e*-SDA processes showed smaller viscosity values than the traditional process. Si7 showed the minimum viscosity value, having 37.5% of the observed viscosity for the SDA process, and is the closest to the viscosity of the *c*-DAO. It is worth mentioning that the behavior of the obtained viscosities for all samples is coherent with their asphaltene and sulfur content [17, 18, 23, 24, 174]. It can be easily noticed that Si7 nanoparticles enhance most of the DAO quality obtained with the *e*-SDA process in agreement with *n*-C_7 adsorption results.

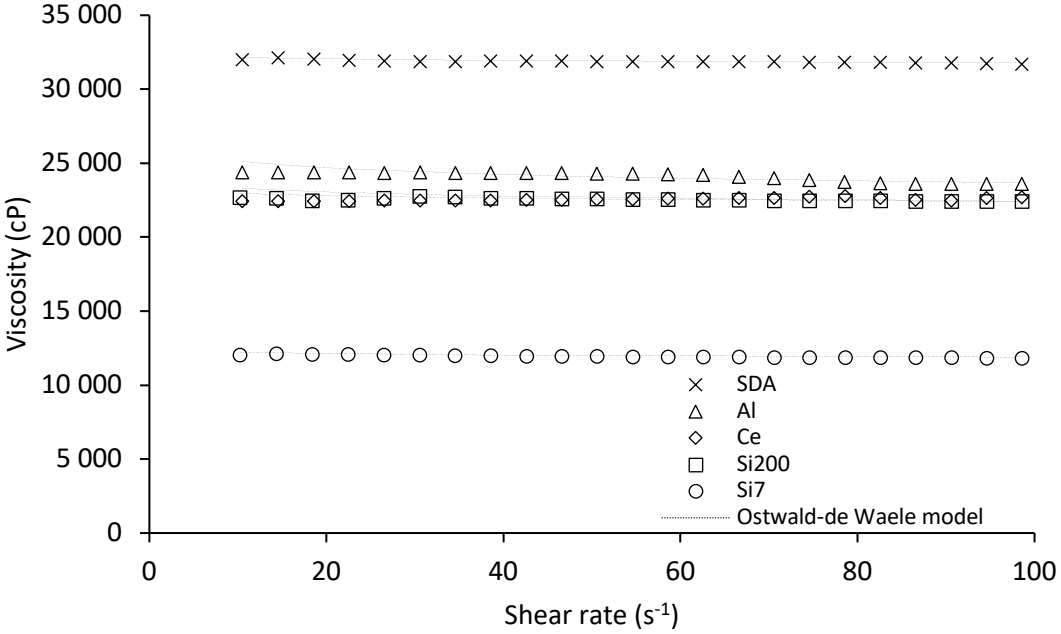

Figure 17. Viscosity as a function of shear stress for the SDA and *e*-SDA processes using Si7, Si200, Al, Ce at dosages of 5 wt% and *n*-heptane as the solvent with a SOR of 8 at 25°C.

Table 11. Oswald-de Waele estimated parameters for rheological experiments for the SDA and *e*-SDA processes using Si7, Si200, Al, Ce at 5 wt% and *n*-heptane as the solvent with a SOR of 8 at 25°C.

Nanomaterial	$K \pm 80$ (cP·s^{n-1})	$n \pm 0.003$ (dimensionless)	R^2	RSME%
SDA	32 470	0.995	0.971	7.6
Si7	12 504	0.988	0.991	1.1
Si200	23 493	0.989	0.986	2.7
Al	26 662	0.973	0.983	2.1
Ce	24 216	0.983	0.989	2.8

2.3.5. *n*-C_7 asphaltenes catalytic oxidation

After evaluating *n*-C_7 asphaltenes' adsorption onto different chemical nature commercial nanoparticles and analyzing their behavior with the SLE model, the catalytic oxidation of the adsorbed *n*-C_7 asphaltenes was carried out. These tests were made in an air atmosphere fixing the asphaltene load for every sample at 0.2 mg/m^{2,} and there were used 5 mg of sample mass to avoid the limitations associated with mass transfer [139, 150, 156]. Figure 18 presents the rate of mass loss and conversion (α) of *n*-C_7 asphaltenes in the absence and presence of commercial nanoparticles. At this point, it is convenient to divide the analysis into three different regions: at the highest temperatures there is located the high-temperature region (HTR) between 451 - 700 °C, the mid-temperature region (MTR), that falls between 251 °C and 450 °C, and the low-temperature

region (LTR) with a maximum value of 250 °C and beginning in 200 °C [30, 139]. Hence, the *n*-C_7 asphaltene conversion starts at approximately 380 °C and the oxidation to form gaseous products was complete at 570°C. There also can be noticed a maximum rate of mass loss nearly to 460 °C, located in the HTR. This value indicates the temperature of *n*-C_7 asphaltene decomposition, and the presence of one only peak reveals that this process mainly occurs in one step.

Figure 18 shows a reduction in the temperature of the beginning of the *n*-C_7 asphaltene decomposition catalytic oxidation for all commercial nanoparticles. For Si7 nanoparticles, the decomposition process begins at 200°C in the LTR and ends in the HTR, passing through the MDR. The peak in the mass loss rate is located in the MDR at 407 °C. These results agree with those reported by Franco et al. [30], which also observed that the *n*-C_7 asphaltene decomposition process temperature passes from the HTR to MTR in the presence of commercial silica nanoparticles. Thus, Si200 nanoparticles generate a similar reduction in the temperature of the *n*-C_7 asphaltene decomposition, but the process begins at 410 °C. Al and Ce nanoparticles showed a similar decrease in the temperature of the peak of the mass loss, located at 334 °C and 325 °C, respectively, just as reported in the literature [140, 150-152].

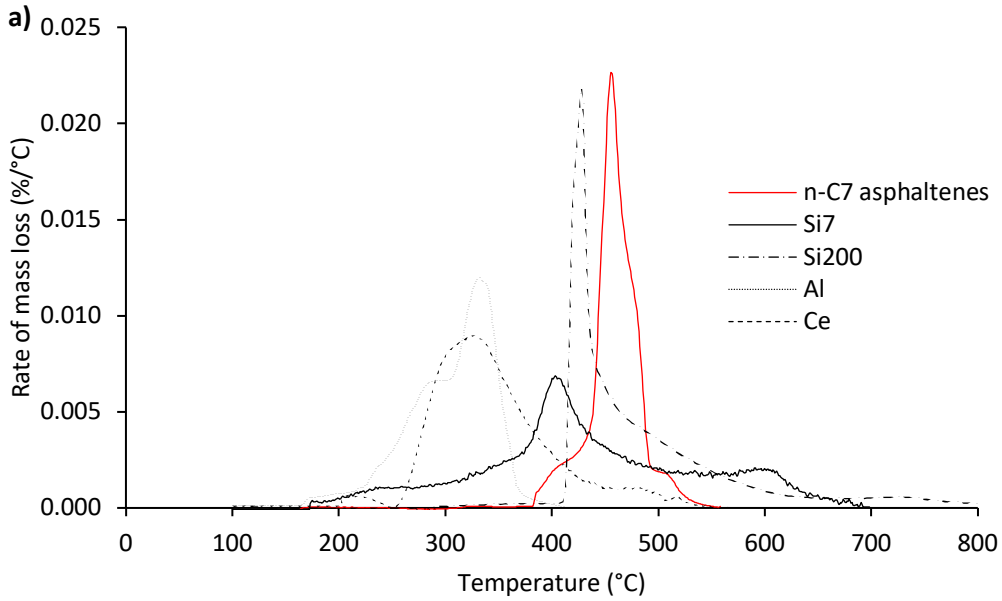

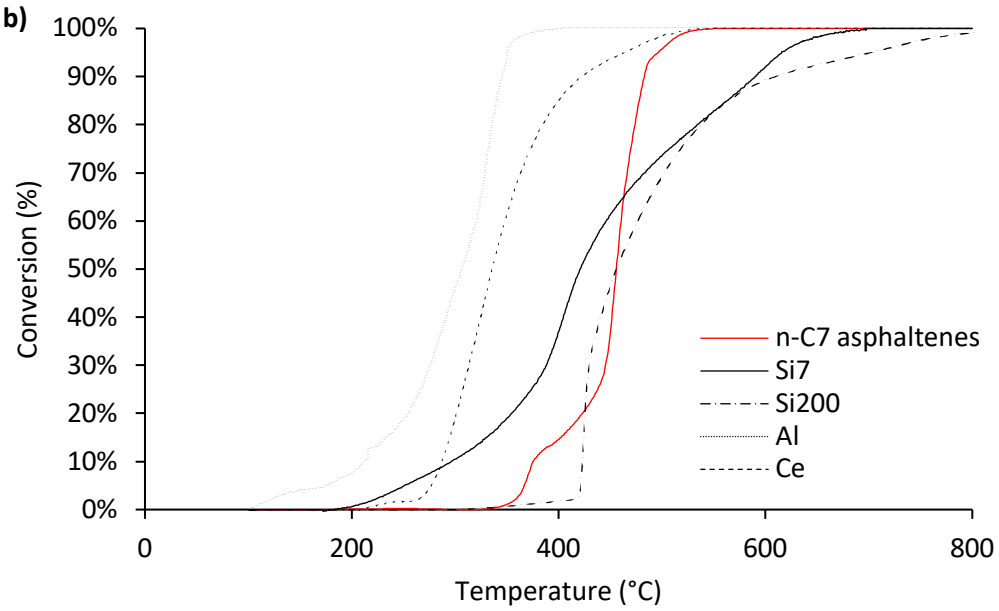

Figure 18. (a) Rate of mass loss and (b) conversion for the *n*-C_7 asphaltenes as a function of temperature in the absence and the presence of Si7, Si200, Al and Ce nanoparticles with the airflow rate of 100 mL/min, the heating rate of 10°C/min and *n*-C_7 asphaltene loading 0.2 mg/m^2.

The previously described OFW method was used to calculate the activation energies of *n*-C_7 asphaltenes extracted from the used cruel oil in the absence and presence of the commercial nanoparticles Si7, Si200, Al and Ce [166, 167]. These results are presented in Figure 19. The *n*-C_7 asphaltenes show the typically observed decreasing behavior of the $E_{\alpha OFW}$ as conversion increased. For the evaluated commercial nanoparticles, the activation energy rises while conversion increases. Si7 and Si200 presented a similar trend and magnitudes for the $E_{\alpha OFW}$ attributed to their similar chemical nature. On the other hand, the silica nanoparticles showed higher activation energy values for all conversion percentages, than those observed for Al and Ce nanoparticles. Precisely, the behavior of alumina and cerium nanoparticles was similar for conversion values below 60%. Above this value, Al presented higher activation energies. All these results agree with those reported in the literature, in which can be noticed that *n*-C_7 asphaltenes adsorbed onto nanoparticles of these chemical nature presented the same behavior, showing for Al and Ce the lowest values for $E_{\alpha OFW}$ at all conversion percentages [139, 140, 148, 150, 151].

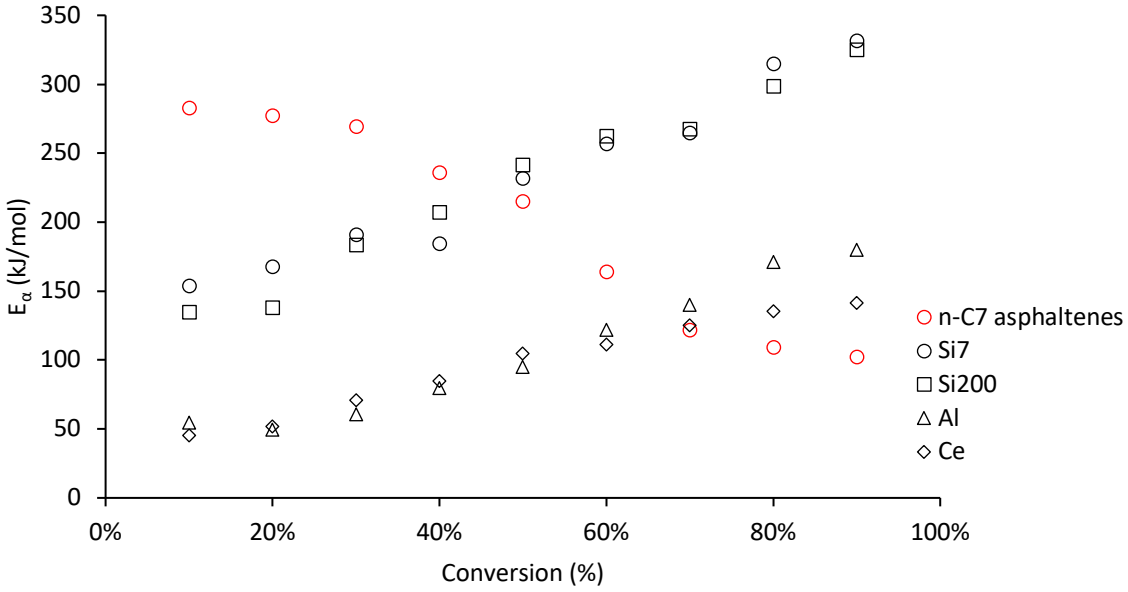

Figure 19. Activation energies estimated through the OFW method for catalytic oxidation of *n*-C_7 asphaltenes in the absence and presence of Si, Si200, Al and Ce.

2.3.6. Pitch catalytic oxidation

Figure 20 presents the rate of mass loss and the conversion for the obtained pitch in the absence and presence of Si7, Si200, Al and Ce nanoparticles. Can be noticed a big difference between the behavior of the catalytic decomposition of pitch and the previously described for *n*-C_7 adsorbed asphaltenes. The first difference between these processes lies in their proportion of nanoparticles. For the *n*-C_7 asphaltene catalyst, their load was fixed at 0.2 mg/m^2 for all evaluated nanomaterials. In the *e*-SDA process carried out using Si7, the pitch load for the oxidation process was near 24 mg/m^2. This value can be easily calculated from pitch yield, nanomaterial surface area and their dosage of 5 wt% against EHO. If we compare concerning mass, there were 77.9 mg of *n*-C_7 asphaltenes for each gram of Si7 in the oxidation process, while there were 8 941 mg of the pitch for each gram of this nanoparticle. With Si200, Al and Ce, a similar situation arose, contributing to the explanation of catalytic behavior for all *e*-SDA pitch samples, and the less notorious difference with SDA pitch, unlike the results of *n*-C_7 asphaltenes oxidation.

Considering the SARA fractions of used EHO and those measured for all DAO samples can be inferred that pitch is composed mainly of *n*-C_7 asphaltene and resins [70]. Hence, its catalytic decomposition should behave like that. In this sense, the SDA pitch oxidation process's obtained result agrees with those reported by other authors [157]. Increasing resins proportion in the mixture with *n*-C_7 asphaltenes raises its oxidative decomposition temperature. For SDA pitch, this temperature can be found nearly to 490 °C, while for *n*-C_7 asphaltenes was 460 °C. For the *e*-SDA process Figure 20 shows that the pitch oxidative decomposition temperature follows the order Ce < Al < Si7 < S200. The reduction for this temperature generated by Si7 compared to the SDA pitch was 4 % and 13 % for Ce, while for *n*-C_7 asphaltene oxidation these values were 11.6 % and 27.8 %, respectively. As

abovementioned, these results agree with the expected due to the high load of pitch onto nanoparticles and the mixture of *n*-C_7 asphaltenes and resins in the catalytic oxidation process. Similarly, in Figure 21, the SDA pitch activation energy ($E_{\alpha OFW}$) presents the behavior of this type of mixture [157]. For the *e*-SDA process, both silica nanoparticles EαOFW are higher than those observed for Al and Ce in all conversion percentages.

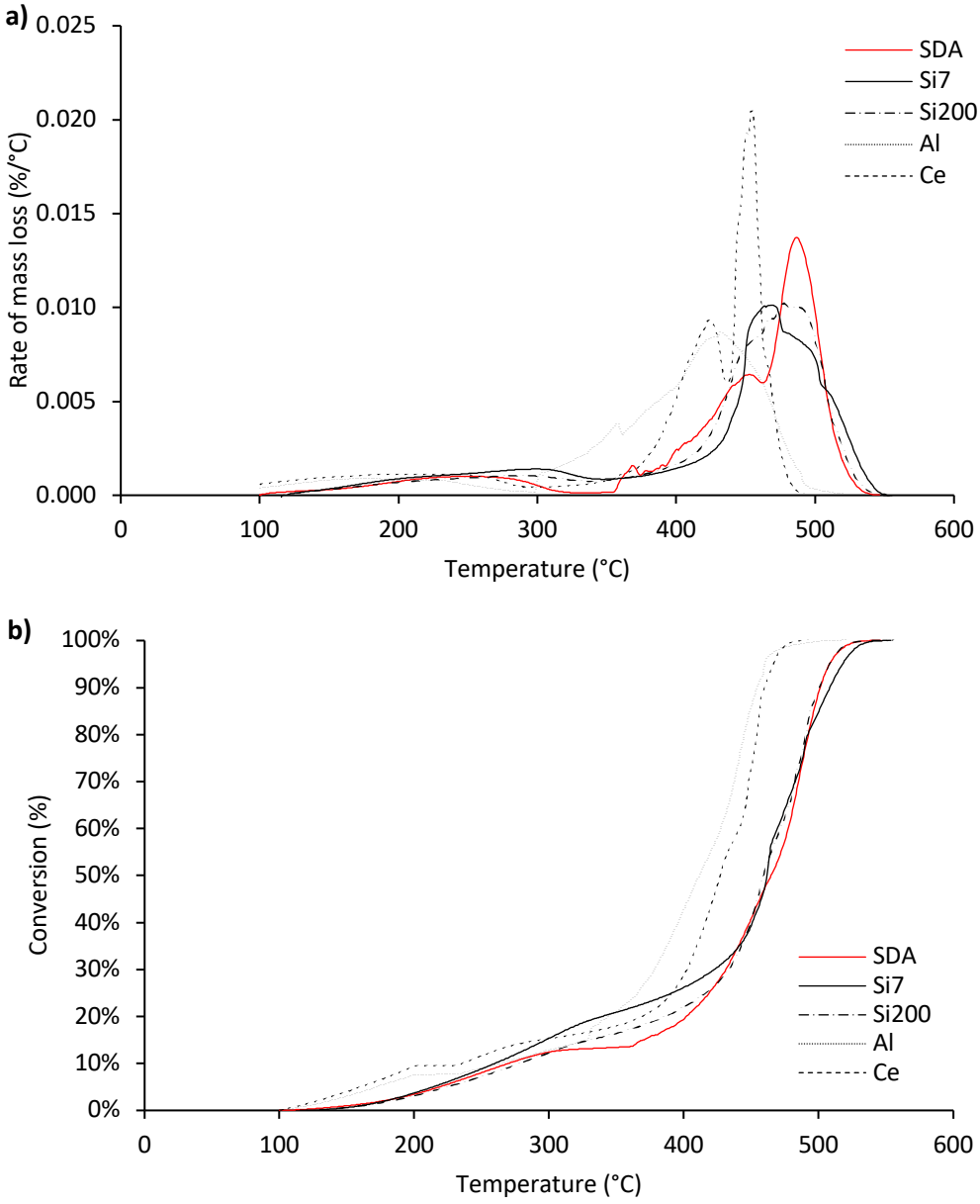

Figure 20. (a) Rate of mass loss and (b) conversion of the pitch for the SDA and *e*-SDA processes carried out with Si7, Si200, Al and Ce nanoparticles with the airflow rate of 100 mL/min and the heating rate of 10°C/min.

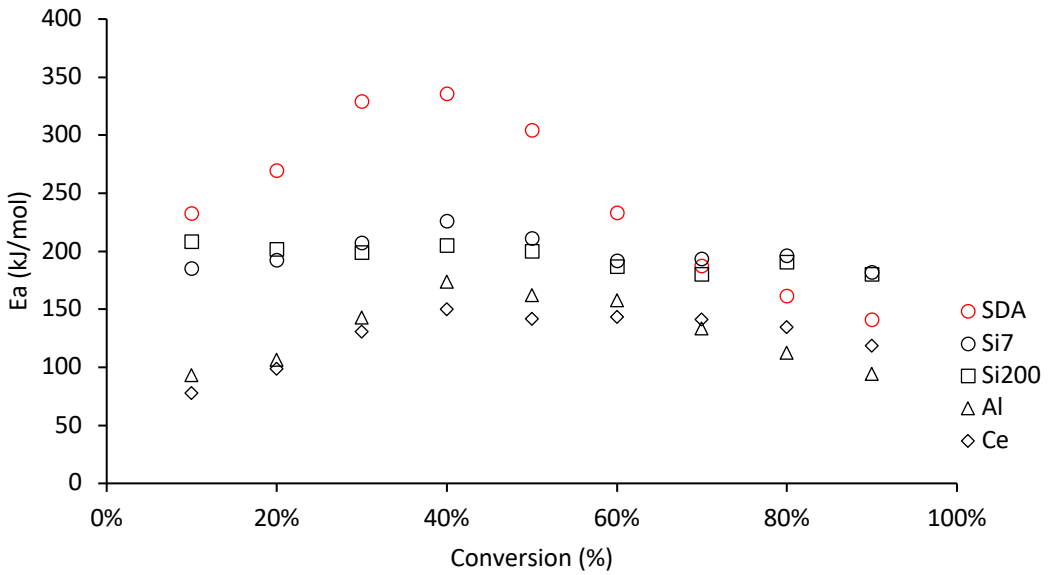

Figure 21. Activation energies evaluated for thermal cracking of pitch for the SDA and *e*-SDA processes carried out with Si7, Si200, Al and Ce nanoparticles.

2.4. Partial conclusions

The asphaltene adsorption properties were evaluated for four different commercial nanoparticles of three different chemical natures. There was found that silica nanoparticles of 7 nm (Si7) presented the highest adsorption affinity. This material also showed the biggest value for the maximum adsorption capacity of asphaltenes fitted through the SLE model. These results were coherent with the obtained for the yield and quality of the DAO produced by the *e*-SDA process. For these, asphaltene and sulfur content, °API, distillable fraction and expected viscosity were improved following the q_m parameter Si7 > Si200 > Ce > Al. It is worth mentioning that for the SDA DAO, the °API reached 63.3% of the maximum value of this property, the 20.93 °API measured for the *c*-DAO, while for Si7 *e*-SDA DAO this percentage was 75.8%.

Regarding the catalytic oxidation of *n*-C_7 asphaltenes and pitch, there was found that nanoparticles have a significant role in this process. There was found that *n*-C_7 asphaltene oxidative decomposition beginning can reduce from 460 °C to 325 °C and 334 °C in the presence of Ce and Al. These differences were less notorious in those obtained for the pitch. The main reason lies in the difference in the dosages used for evaluating *n*-C_7 asphaltene catalytic oxidation, fixed at 0.2 mg/m^2. For the obtained pitch with Si7, this proportion was 24 mg/m^2 due to the used wt% of nanoparticles for all *e*-SDA processes [70]. Despite this, all evaluated materials reduced the temperature of catalytic oxidation of pitch. Considering this, Si7 was selected as the best material for its performance in terms of DAO quality, and its catalytic properties will be potentiated with metal oxide functionalization.

3. Improvement of the catalytic properties of selected support through a simplex-centroid mixture design

Previously there were presented the result of asphaltene adsorption and its catalytic conversion for different nanoparticles' chemical nature, like silica (Si7 y Si200), alumina (Al) and cerium (Ce). All this to find the nanoparticle with the best adsorption conditions for *n*-C_7 asphaltenes extracted from used crude oil. There was found that Si7 presented the greatest adsorption affinity for these compounds, represented in the smaller *H* parameter [154]. This nanomaterial also showed the biggest q_m parameter, which gives us an idea of the maximum *n*-C_7 asphaltene adsorption capacity [154]. Precisely, as abovementioned, there was found a direct relationship between this parameter and DAO yield, the same trend as with asphaltene content directly related with sulfur content and, therefore, with the DAO rheological properties, just as Conradson carbon content [17, 18, 23, 24, 70, 75, 173, 174]. In fact, there was observed that DAO °API tendency follows the same trend, and the DAO obtained with the *e*-SDA process carried out with Si7 nanoparticles presents a higher quality.

n-C_7 asphaltene and pitch catalytic oxidation there were also evaluated. It can be found that nanoparticles can enhance both processes, being the selected Si7 as those with the highest possibilities for improvements. In the literature, can be found functionalization process carried out on different chemical nature nanoparticles for improving their catalytic properties, especially for in-situ upgrading applications [30, 138-140, 148, 151, 175]. In this kind of research, a low dosage of the metal oxides was used in the synthesis process, typically a maximum of 2 wt%. However, for on-site applications, especially those in the refinery, the metal load of catalyst can be superior to 20 wt% [176-184]. Some of these catalysts have been optimized, obtaining metal loads superior to 10 wt% [176, 178, 181, 183, 184]. For all this, Si7 nanoparticles were selected as support for the functionalization process following the percentages established in the described simplex-centroid mixture design (SCMD) shown in Figure 22 to potentiate its catalytic properties.

The results showed an improvement in the *n*-C_7 asphaltene adsorption properties of Si7 with NiO and PdO functionalization. As expected, the obtained DAO samples also presented upgrading in their quality. However, the most remarkable results were observed for reducing the catalytic oxidation temperature of *n*-C_7 asphaltene as the response value for the proposed SCMD. It can be noticed that the best results were those shown by bimetallic nanoparticles. The statistical analysis predicts the best dosage of metal oxides to improve *n*-C_7 asphaltenes and pitch catalytic oxidation.

3.1. Materials and methods

All the materials and methods described in chapter 2 were used and applied in this chapter. This includes Si7 nanoparticles selected as the support for the functionalization process and the EHO for *n*-C_7 asphaltene extraction and for carrying on the different deasphalting processes. The same for

the employed methods for nanoparticle characterization, *n*-C_7 asphaltene extraction, obtaining equilibrium adsorption isotherms, DAO separation and characterization and for evaluating the catalytic oxidation of *n*-C_7 asphaltene and pitch. The only materials and methods detailed in this section are those that were used and have not been previously specified.

3.1.1. Materials

Salt precursors of $Pd(NO_3)_2 \cdot 2H_2O$ and $NiCl_2 \cdot 6H_2O$ (Merck KGaA, Darmstadt, Germany) and distilled water were used to functionalize nanoparticles. *n*-heptane (99%, Sigma-Aldrich, St. Louis, MO, USA) was used for carrying on SDA and *e*-SDA processes. *n*-C_7 asphaltenes were dissolved in toluene (99.5%, Merk KGaA, Germany) for preparing a stock solution of 2000 mg/L for adsorption batch experiments.

3.1.2. Methods

3.1.2.1. Nanoparticles functionalization

Si7 nanoparticles, selected by their adsorption properties, will be functionalized with NiO and PdO according to a three-component simplex centroid mixture design (SCMD) of experiments. The SCMD is usually used to study a mixture of different components over a determined response variable [185]. In this case, there was used to determine the optimal dosages of used metal that minimize the oxidation temperature of *n*-C_7 asphaltenes. The maximum Ni and Pd dosages were set to 10% of the mass fraction.

For the functionalization, Si7 nanoparticles were dried at 120°C for 2 h. An aqueous solution of nickel chloride ($NiCl_2 \cdot 6H_2O$) and/or palladium nitrate ($Pd(NO_3)_2 \cdot 2H_2O$) is employed using the incipient wetness technique [148, 164, 186]. The obtained composite nanoparticles were dried for 6 h at 120°C, and the obtained solid was calcinated at 450°C for 6 h [139].

3.1.2.2. Nanoparticles characterization

Besides the previously described procedures, the crystallite size of the nanoparticles was measured through the Scherrer equation. To make it, XRD patterns were recorded with an X'Pert PRO MDP X-ray diffractometer from PANalytical (Almelo, the Netherlands) using Cu Kα radiation operating at 60 kV and 40 mA with a θ/2θ goniometer.

3.2. Modeling. Simplex-centroid mixture design

In this section, there are presented the Simplex-centroid mixture design. The SLE model [154] and the Ozawa-Flynn-Wall method (OFW) [166, 167] were used, as explained in chapter 2.

The optimal mixture of Ni, Pd and selected support was found to minimize the initial temperature of conversion of the asphaltenes through a design of experiments. A simplex-centroid mixture design (SCMD) was run using the Minitab software (version 19, Minitab, LLC, PA, USA). Silica, nickel, and palladium mass fraction were variated into determined limits. In this sense, the SCMD was used to predict the response of the asphaltene catalytic oxidation according to the variability of the mass components of functionalized nanoparticles. The proportion used for each component must satisfy the following restriction [185, 187]:

Equation 10. $$\sum_{i=1}^{n_c} x_i = x_1 + x_2 + \cdots + x_{n_c} = 1 \qquad x_i \geq 0$$

Where, the n_c parameter is related to the number of components in the mixture, and x_i establishes the proportion of each *i* component. For this mixture design n_c = 3 and the components were x_1 = Si, x_2 = Ni and x_3 = Pd. Thus, the limits selected for each compound are:

Equation 11. $$0.9 \leq Si \leq 1.0$$

Equation 12. $$0 \leq Ni \leq 0.1$$

Equation 13. $$0 \leq Pd \leq 0.1$$

A cubic model special model was selected according to the selected SCMD attending Equation 10. Precisely, the regression model equations are as follows:

Equation 14. $$\alpha_m = \beta_1 x'_1 + \beta_2 x'_2 + \beta_3 x'_3 + \beta_{12} x'_1 x'_2 + \beta_{13} x'_1 x'_3 + + \beta_{23} x'_2 x'_3 + + \beta_{123} x'_1 x'_2 x'_3$$

Equation 15. $$x'_i = \frac{x_i - L_i}{1 - L}$$

Where α_m is the temperature of the beginning of the oxidative conversion process of asphaltenes, βi, βij and βijk are the coefficients of the linear terms, the binary mixtures of nonadditive components, and the ternary mixture of nonadditive components, respectively. Additionally, in Equation 15, L_i is the lower limit for each component, *L* is the sum of the lower boundaries and x'_i is a pseudo-component of x_i and is used because of the restrictions mentioned in Equation 11 to 13. Figure 22 shows the SCMD for Si7, nickel and palladium and Table 12 shows the used terminology for the synthesized nanoparticles and the nominal mass of their components.

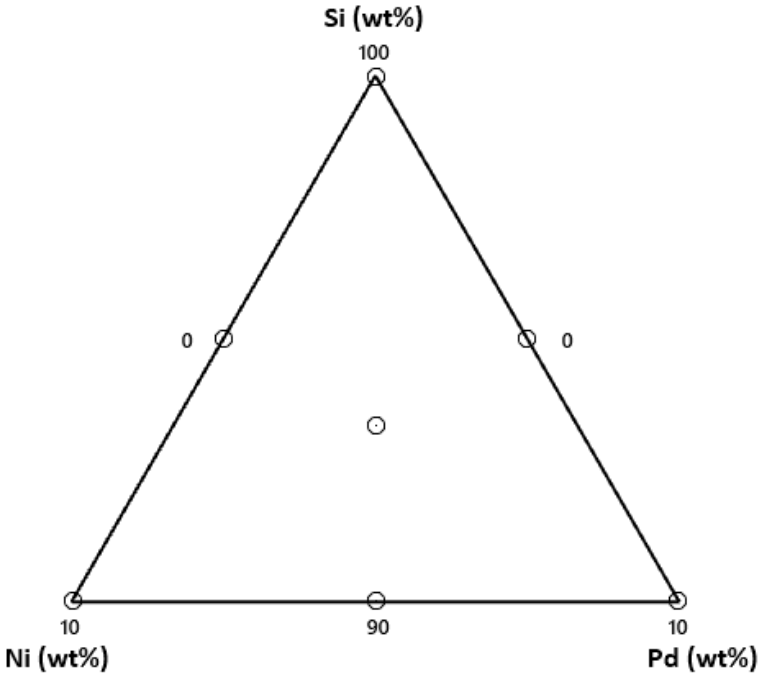

Figure 22. Simplex-centroid mixture design with Si7, nickel and palladium.

Table 12. Nomenclature and mass fraction of prepared nanoparticles composed by silica support (SiO_2) of 7 nm with NiO and PdO.

Nanomaterial	Nominal oxides	Nominal mass fraction (%)
SiO_2	SiO_2	100.0
SiNi5	SiO_2	95.0
	NiO	5.0
SiNi10	SiO_2	90.0
	NiO	10.0
SiPd5	SiO_2	95.0
	PdO	5.0
SiPd10	SiO_2	90.0
	PdO	10.0
SiNi5Pd5	SiO_2	90.0
	NiO	5.0
	PdO	5.0
SiNi3.3Pd3.3	SiO_2	93.3
	NiO	3.3
	PdO	3.3

3.3. Results

3.3.1. Functionalized nanoparticles characterization

Table 13 summarizes the characteristics of functionalized nanoparticles with Si7 as support. There was measured their hydrodynamic diameter determined with DLS (dp_{50}), superficial area (S_{BET}) and crystal size ($dp_{Crystallite}$). The hydrodynamic diameter revealed that nickel monometallic synthesized nanoparticles showed more significant values than palladium ones. These results agree with those reported by other authors who studied nickel functionalization over different supports and who measured their hydrodynamic diameter by DLS [188-191]. They also found that rising the Ni dosage in the functionalization process propitiates higher values for this property than particle size found through other techniques such as SEM, TEM and XPR. For palladium, a similar situation has been reported but in less proportion [192]. These results agree with the measured dp_{50}, which rises as increasing the dosage of monometallic oxides. S_{BET} was reduced for the greater dosages of NiO or PdO, but not in the same proportion if considering the total metal oxide mass in the bimetallic nanoparticles. The explanation of this situation can be found in the $dp_{Crystallite}$. It can be noticed that it increases as the metal oxide on the supported nanoparticle increases, but for bimetallic nanoparticles the crystal size is smaller than for monometallic samples. This behavior is associated with the used metals, which avoid sintering processes generating a less heterogeneous surface due to the high dispersion of these crystals in the support [139, 140, 152, 159]. According to TGA analysis, all functionalized nanoparticles are thermally stable and didn't present mass losses until 700 °C.

Table 13. Hydrodynamic diameter, surface area and the crystal size of prepared nanoparticles composed by silica support (SiO_2) of 7 nm with NiO and PdO.

Nanomaterial	dp_{50DLS} ± 1 (nm)	S_{BET} ± 0.5 (m^2/g)	$dp_{Crystallite}$ ± 0.2 (nm)	
			NiO	PdO
SiNi5	41	267.1	7.3	-
SiPd5	18	306.4	-	4.3
SiNi10	52	260.7	8.1	-
SiPd10	21	303.8	-	5.2
SiNi3.3Pd3.3	23	311.7	3.6	2.3
SiNi5Pd5	27	293.6	4.1	2.9

3.3.2. *n*-C_7 asphaltene adsorption

The obtained adsorption isotherms for all functionalized nanoparticles included in the SCMD are presented in Figure 23 with the fit of the SLE model. It can be noticed that bimetallic and palladium monometallic-based nanoparticles present type Ib adsorption isotherms [172]. Other authors have reported this kind of isotherms for silica-based nanoparticles and *n*-C_7 asphaltenes [30, 139-141]. In agreement with those, Figure 23 shows that adsorption capacity for bimetallic and PdO supported nanoparticles followed the order SiNi5Pd5 > SiNi3.3Pd3.3 > SiPd10 > SiPd5. On the other hand, nickel

monometallic-based nanoparticles show type III isotherms [172]. This behavior can be attributed to the sizes of the metal oxide diameter, blocking some of the adsorption active available sites and reducing the surface area [134]. This situation propitiates the self-association process of *n*-C_7 asphaltenes and the presence of multilayer adsorption. Similar results were observed by Franco and colleagues [148]. They found that increasing the dosage of NiO over alumina nanoparticles could reduce the superficial area leading to porosity blockage, reducing the potential benefit of functionalization processes with metal oxide with large dosages. Other reasons contributing to obtaining type III isotherms for NiO supported nanoparticles can be found in their hydrodynamic diameter, significantly bigger than those observed for PdO and bimetallic nanoparticles. This situation propitiates more nanoparticle-nanoparticle interaction, reducing the available active sites for adsorption, even related to some limitation of the mass transfer disadvantaging adsorptive process [193]. All these situations could explain the formation of multiple layers of *n*-C_7 asphaltenes onto the adsorbent surface [143].

Additionally, these explanations are supported by the obtained parameters of the SLE model presented in Table 14. The observed values of the *K* parameter show that can be expected increasing *n*-C_7 asphaltene multiple layers as NiO dosage grows for monometallic nanoparticles [154]. The formation of multiple layers of adsorbant on their surface is expected to be bigger for bimetallic than PdO monometallic nanoparticles and Si7 support. The maximum adsorption capacity (q_m), decrease in the order SiNi10 > SiNi5 > SiNi5Pd5 > SiNi3.3Pd3.3 > SiPd10 > SiPd5. As abovementioned, this parameter is closely related to DAO yield and quality. However, there wasn't found a lineal proportion as previously due to the obtained type III isotherm for NiO monometallic nanoparticles. Finally, related to the *H* parameter obtained values, the bimetallic nanoparticles presented the lowest value and the highest affinity for *n*-C_7 asphaltenes [30, 139, 154].

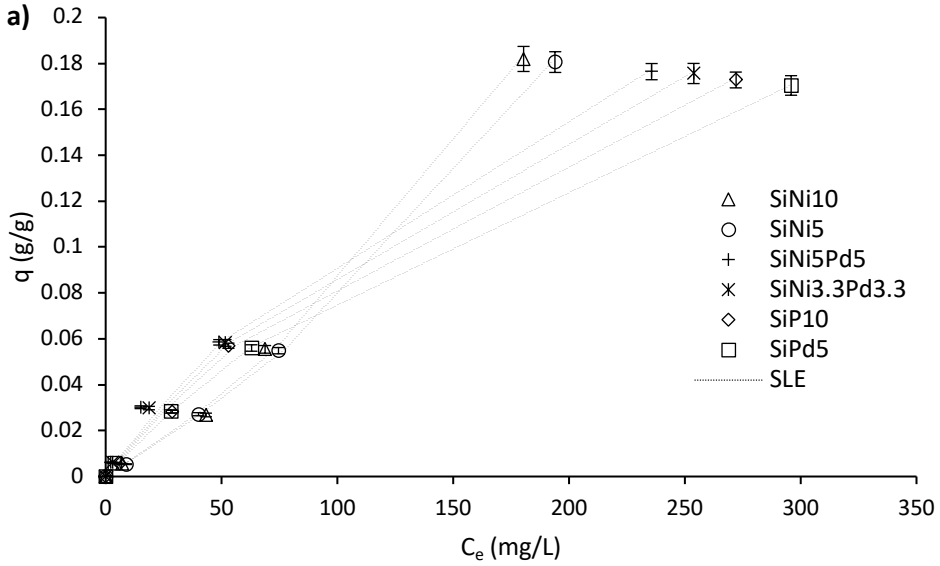

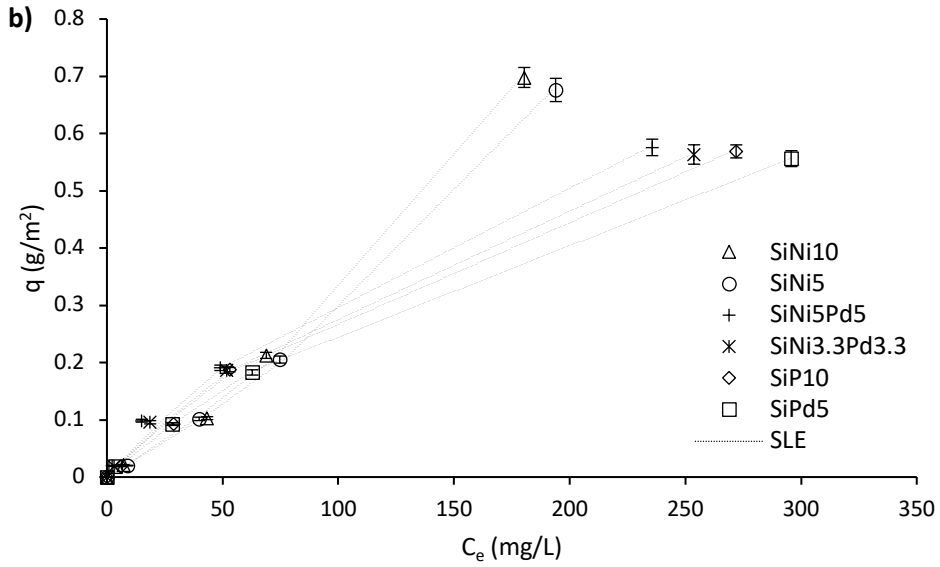

Figure 23. Adsorption isotherms of *n*-C_7 asphaltenes onto SiNi5, SiNi10, SiPd5, SiPd10, SiNi3.3Pd3.3 and SiNi5Pd5 nanoparticles at 25 °C expressed in (a) g/g and (b) mg/m^2.

Table 14. Estimated values of the SLE model parameters for the adsorption isotherms of *n*-C_7 asphaltenes onto functionalized nanoparticles.

Nanomaterial	***H*** **± 0.02 (mg/g)**	***K*** **± 0.06 (g/g)**	q_m **± 0.01 (g/g)**	R^2	RSME
SiNi5	1.84	1.69	4.77×10^{3}	0.999	0.002
SiPd5	1.08	0.12	0.63	0.999	0.001
SiNi10	1.91	1.91	5.93×10^{3}	0.998	0.004
SiPd10	0.94	0.56×10^{-2}	0.66	0.999	0.003
SiNi3.3Pd3.3	0.89	0.02×10^{-2}	0.69	0.999	0.003
SiNi5Pd5	0.83	0.02×10^{-2}	0.71	0.998	0.005

3.3.3. DAO yield and quality

Figure 24 present the DAO and pitch yields for the *e*-SDA process using *n*-heptane with a SOR of 8 for monometallic and bimetallic functionalized nanoparticles at a dosage of 5 wt% at 25°C. It can be noticed for the *e*-SDA process that DAO yield decreased in the order SiPd5 ≈ SiPd10 > SiNi5Pd5 ≈ SiNi3.3Pd3.3 > SiNi5 ≈ SiNi10, which is the same order for the increasing of pitch yield. As previously noticed for commercial nanoparticles, these results can be explained by the q_m parameter values of the adsorption isotherms. Again, there was evidenced the inverse relationship between this parameter and DAO yield. Additionally, it can be seen that both NiO monometallic nanoparticles presented similar DAO and pitch yields, the same as the PdO and the bimetallic-ones.

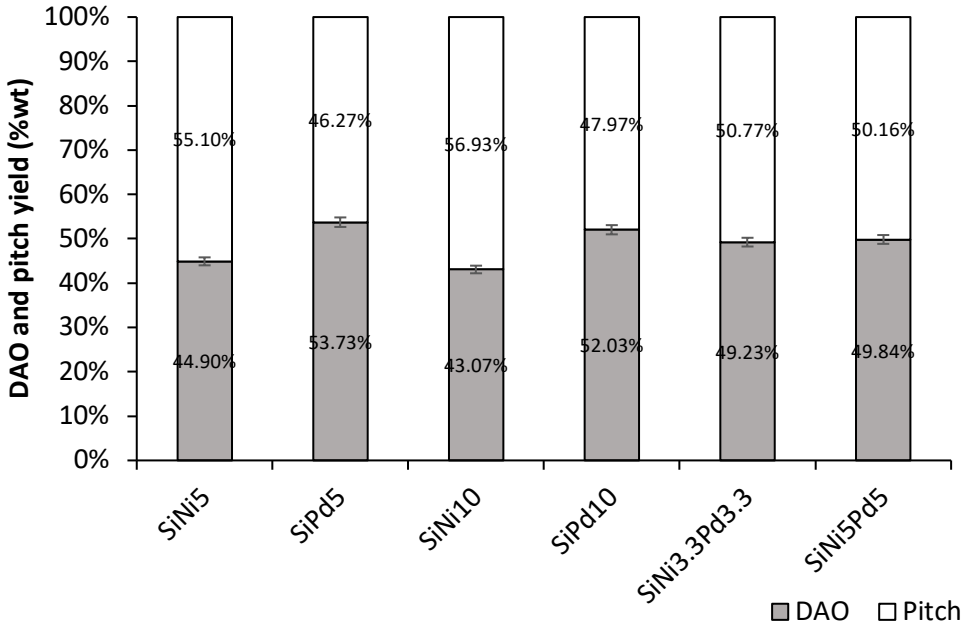

Figure 24. DAO and pitch yields for the *e*-SDA process for SiNi5, SiPd5, SiNi10, SiPd10, SiNi3.3Pd3.3 and SiNi5Pd5 at dosages of 5 wt% and *n*-heptane as the solvent with a SOR of 8 at 25°C.

The obtained DAO quality was determined through their SARA fractions, API gravity, sulfur content, rheological behavior, and simulated distillation to determine the percentage of distillable fraction and the Conradson carbon residue. Figure 25 presents the SARA fractions for the *e*-SDA process with the functionalized nanoparticles with metal oxides. It can be noticed that the wt% of saturates and aromatic compounds are approximately constant for all samples. The same results were obtained for resins that constituted about 64 wt% of evaluated DAO samples, with a slightly higher value for SiPd10. This situation was previously explained for commercial nanoparticles. It is related to the presence and the quantity of used solvent that propitiates the separation of the resins, inhibiting its peptizing effect and favoring *n*-C_7 asphaltene aggregation and precipitation [70, 74, 124-127]. The obtained DAO asphaltene content decrease in order SiPd5 ≈ SiPd10 > SiNi5Pd5 ≈ SiNi3.3Pd3.3 > SiNi5 ≈ SiNi10, in agreement with the observed relationship with q_m parameter and DAO yield. For SiNi10, the reduction of *n*-C_7 asphaltene wt% was 26.2%, 45.0% and 68.8% compared to Si7, SDA process and the crude oil *n*-C_7 asphaltene wt%, respectively. The sulfur content presented the same trend, explained by the relationship between this and asphaltene content [70, 75]. Finally, the same behavior observed for DAO yield for the couples of NiO, PdO and bimetallic nanoparticles can be seen for DAO quality.

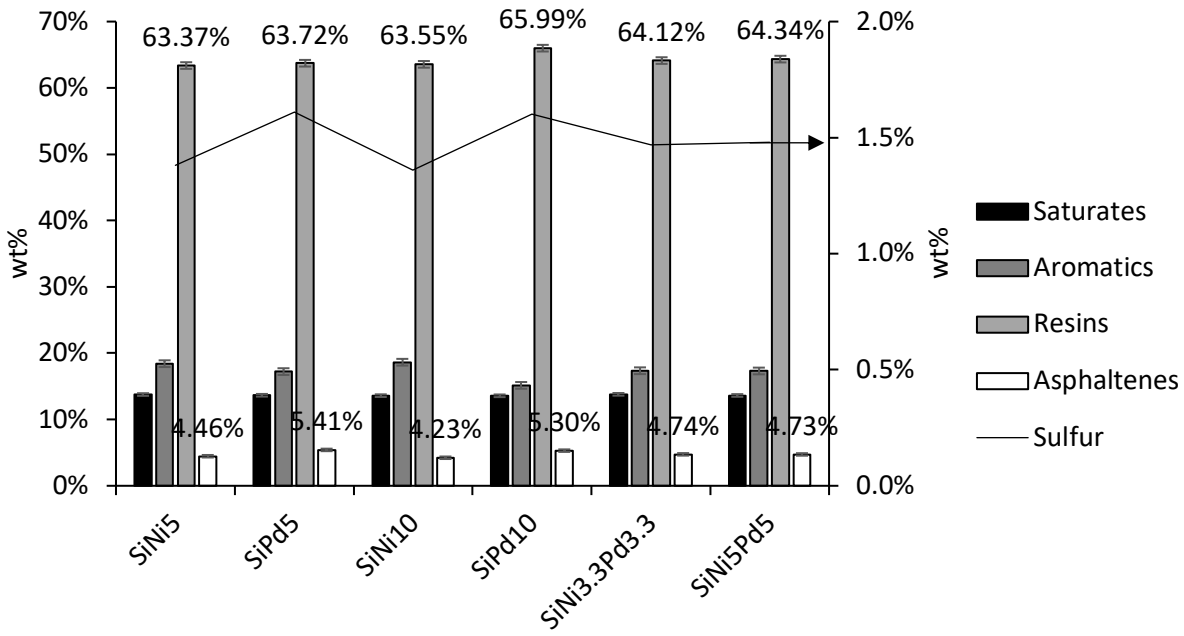

Figure 25. SARA fractions and sulfur content for the *e*-SDA process using SiNi5, SiPd5, SiNi10, SiPd10, SiNi3.3Pd3.3 and SiNi5Pd5 at dosages of 5 wt% and *n*-heptane as the solvent with a SOR of 8 at 25°C.

Figure 26 presents the behavior of API gravity and Conradson carbon residue for the DAO samples. The °API obtained for NiO monometallic nanoparticles showed a higher value and improved this property by 25.6%. These results agree with the previously obtained for commercial nanoparticles and those reported in the literature [70]. Figure 26 also shows that the Conradson carbon content of DAO samples has the same inverse order of q_m parameter exhibited by the asphaltene wt%. These results make sense as the asphaltenes are one of the biggest causes for this residue [173].

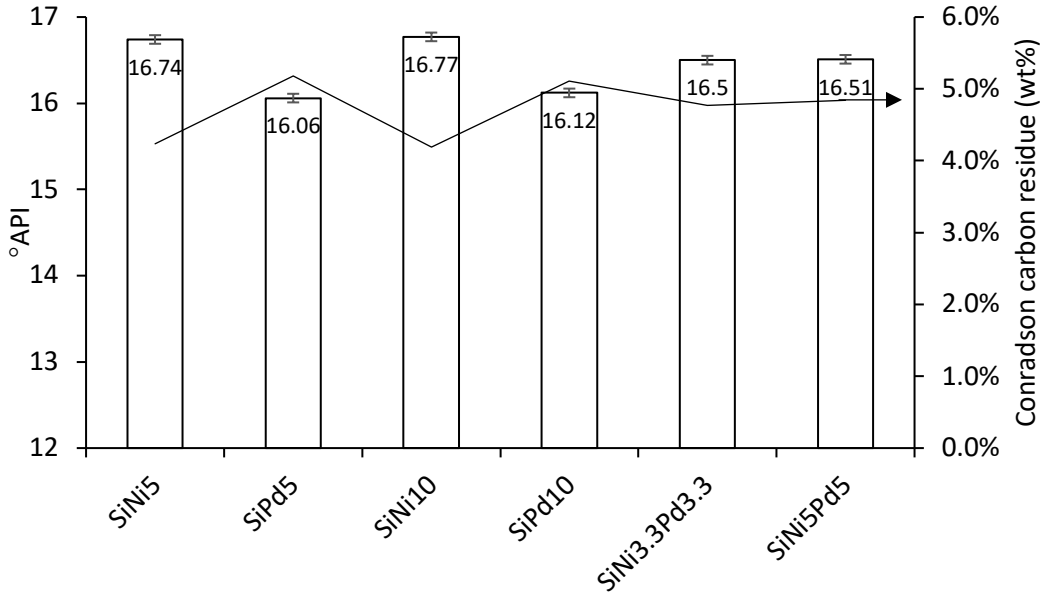

Figure 26. DAO API gravity and carbon Conradson residue the *e*-SDA process using SiNi5, SiPd5, SiNi10, SiPd10, SiNi3.3Pd3.3 and SiNi5Pd5 at dosages of 5 wt% and *n*-heptane as the solvent with a SOR of 8 at 25°C.

The DAO rheological behavior is the last property evaluated for determining its quality. The viscosity measurements and the fitting with the Oswald-de-Waele model for different shear rates are presented in Figure 27. Additionally, Table 15 shows the estimated parameters of the mentioned model. The value of the *n* parameter is close to 1 for all samples, which allows concluding that all present a nearly Newtonian behavior [121, 122]. This behavior of the viscosity non-depending on the shear rate makes that the value of the parameter *K* can be considered the expected viscosity. In this sense, this *e*-SDA process generates viscosity values considerably smaller than previously observed for crude oil and the process carried out without nanoparticles. The expected viscosity values decrease following the order SiPd5 ≈ SiPd10 > SiNi5Pd5 ≈ SiNi3.3Pd3.3 > SiNi5 ≈ SiNi10. The minimum viscosity value was obtained for SiNi10 and reduced 79.0% of the viscosity observed for the SDA process. Just as noticed for commercial nanoparticles, the behavior of the obtained viscosities for all samples is coherent with their asphaltene and sulfur content [17, 18, 23, 24, 174], which also exhibits a behavior similar to the q_m parameter.

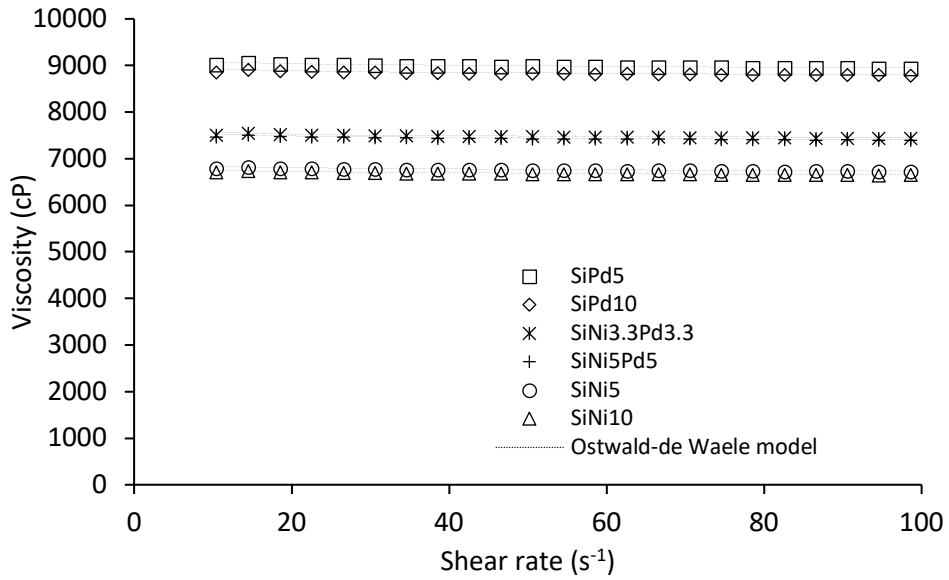

Figure 27. Viscosity as a function of shear rate for the *e*-SDA process using SiNi5, SiPd5, SiNi10, SiPd10, SiNi3.3Pd3.3 and SiNi5Pd5 at dosages of 5 wt% and *n*-heptane as the solvent with a SOR of 8 at 25°C.

Table 15. Oswald-de Waele estimated parameters for rheological experiments for the *e*-SDA process using SiNi5, SiPd5, SiNi10, SiPd10, SiNi3.3Pd3.3 and SiNi5Pd5 at dosages of 5 wt% and *n*-heptane as the solvent with a SOR of 8 at 25°C.

Nanomaterial	$K \pm 8$ (cP·s^{n-1})	$n \pm 0.001$ (dimensionless)	R^2	RSME
SiNi5	6923	0.994	0.991	0.007
SiPd5	9195	0.993	0.987	0.009
SiNi10	6834	0.994	0.993	0.006
SiPd10	9026	0.993	0.984	0.012
SiNi3.3Pd3.3	7657	0.994	0.992	0.007
SiNi5Pd5	7616	0.994	0.992	0.008

The functionalization processes were carried on following the proposed SMCD for optimizing the catalytic oxidation of *n*-C_7 asphaltenes. However, the presence of NiO and PdO onto Si7 nanoparticles improves their adsorption properties, which was reflected in the observed results for DAO quality and yield. For example, the value of °API for the SiNi10 sample was 80 % of the previously reported for *c*-DAO. Something similar was observed for the rest of the variables related to DAO quality, especially for expected viscosity. The minimum value reachable for a DAO is 4 315 cP, corresponding to the c-DAO without *n*-C_7 asphaltene. The lowest measure for viscosity was observed for SiNi10 with 6 834 cP.

3.3.4. *n*-C_7 asphaltenes and pitch catalytic oxidation

Figure 28 presents the rate of mass loss and conversion for *n*-C_7 asphaltenes as a function of temperature in the presence of SiNi5, SiNi10, SiPd5, SiPd10, SiNi3.3Pd3.3 and SiNi5Pd5 nanoparticles with the airflow rate of 100 mL/min, the heating rate of 10°C/min and *n*-C_7 asphaltene loading 0.2 mg/m^2. All monometallic functionalized nanoparticles showed two main peaks in the mass loss rate. Those based on the nickel metal oxide had the first peak in the MTR, at 292 °C for SiNi5 and 275 °C for SiNi10. The second peaks were located in the HTR at 460 °C and 453 °C for SiNi5 and SiNi10. For the PdO supported nanoparticles, a similar situation was observed with one peak in the LTR and the other in the HTR. The first one is located approximately at 220 °C and 240 °C and the second at 510 °C and 535 °C, for SiPd10 and SiPd5. These results show that the presence of palladium on the nanoparticle surfaces makes them better catalysts than those synthesized from only nickel oxide. Similar behaviors were previously reported in the literature for silica functionalized with NiO or PdO when can be noticed for both metal oxides the presence of two peaks in the same regions as observed in Figure 28 [30, 139]. However, in this figure can also be noticed two main differences from the obtained results by Franco et al. [30, 139]. The first was the presence of only two peaks for PdO supported nanoparticles. This situation can be related to the high dosage of this metal of a minimum of 5 wt%; hence their increase doesn't cause the same proportional response in reducing the temperature of oxidation reactions. The third difference was noticed for NiO supported nanoparticles. The first reaction peak, located in the MTR, was found at lower temperatures for the higher oxide metal dosage.

According to the SCMD, there were used SiNi3.3Pd3.3 and SiNi5Pd5 to evaluate the effect of using a bimetallic catalyst in *n*-C_7 asphaltene oxidation. From Figure 28 can be noticed for both samples the presence of two peaks of mass loss ratio. One of these was situated in the LTR for the two samples at approximately 197 °C. The second peak was presented at the MTR for the SiNi5Pd5 at around 410 °C, while for the SiNi3.3Pd3.3 was seen at 475 °C at the HTR. These results reveal a synergetic effect between NiO and PdO when functionalized in the Si7 nanoparticles. This behavior can be attributed to the presence of both metals over the silica surface, reducing even the lowest temperature of the first peak of the mass loss ratio presented in the LTR for monometallic palladium nanoparticles. Panel b from Figure 28 also remarks on the synergistic effect of NiO and PdO. This analysis reveals that conversion for bimetallic nanoparticles is the biggest, except for the section between 320 °C and 380 °C in the MTR. This catalytic behavior of bimetallic nanoparticles is explained by the selectivity of the different compounds of *n*-C_7 asphaltenes and their selectivity to NiO or PdO [30, 139]. Precisely, this type of structure that combines a non-noble metal like nickel and a noble one as the palladium propitiates a more efficient conversion in catalytic processes due to better surface electronegativity [30].

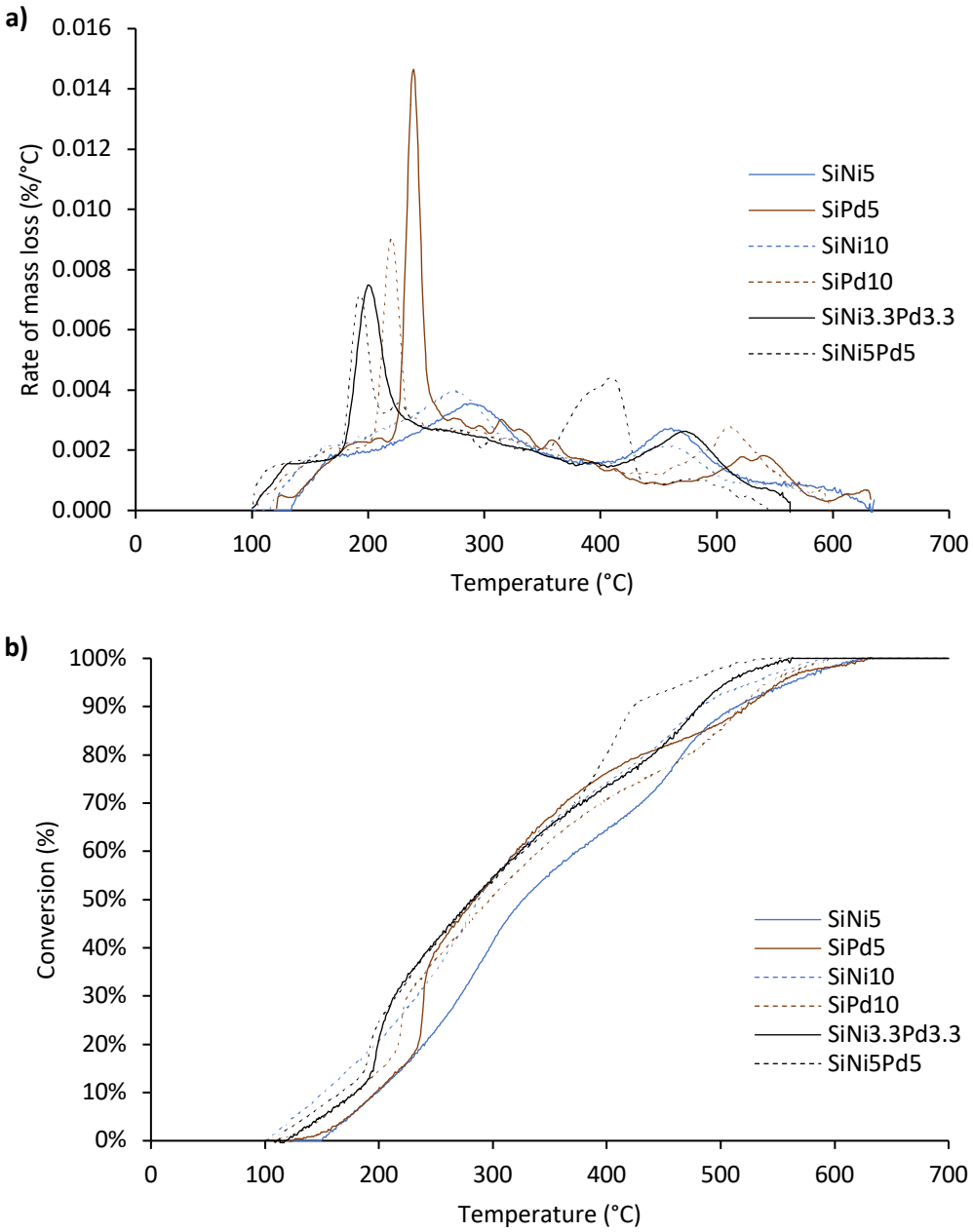

Figure 28. (a) Rate of mass loss and (b) conversion for *n*-C_7 asphaltenes as a function of temperature in the presence of SiNi5, SiNi10, SiPd5, SiPd10, SiNi3.3Pd3.3 and SiNi5Pd5 nanoparticles with the airflow rate of 100 mL/min, the heating rate of 10°C/min and *n*-C_7 asphaltene loading 0.2 mg/m^2.

Figure 29 presents the activation energies at different conversions for SiO and/or PdO functionalized nanoparticles. In general terms, it can be noticed that the lowest $E_{\alpha OFW}$ values correspond to bimetallic nanoparticles. In the same way, monometallic NiO nanoparticles present the highest activation energy values for all conversion percentages. At fixed conversion percentages of 30 and 70, the $E_{\alpha OFW}$ follow the order SiNi5 > SiNi10 > SiPd5 > SiPd10 > SiNi3.3Pd3.3 > SiNi5Pd5. These

results agree with the reported in the literature, where NiO monometallic functionalized nanoparticles usually present bigger $E_{\alpha OFW}$ values than those of monometallic PdO based at similar dosages. The last also presented higher activation energies than bimetallic nanoparticles functionalized with both metal oxides [30, 139, 140]. For conversion between 40 and 50% can be noticed a change in the previously mentioned order with the activation energy value of SiPd5 being bigger than the reported for SiNi10. For these conversion values, SiPd5 has already oxidated the smaller asphaltene aggregates and requires a higher $E_{\alpha OFW}$ to begin with the catalytic decomposition of larger aggregates, while SiNi10 is still oxidating the smaller compounds [30].

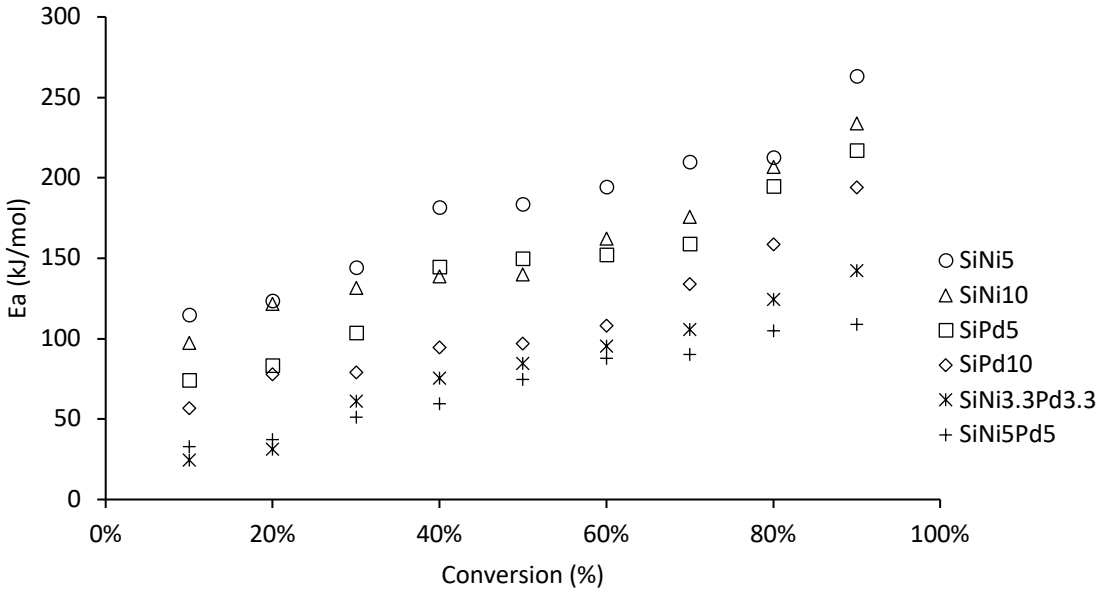

Figure 29. Activation energies evaluated for thermal cracking of *n*-C_7 asphaltenes in the absence and presence of SiNi5, SiNi10, SiPd5, SiPd10, SiNi3.3Pd3.3 and SiNi5Pd5.

The oxidative decomposition of the pitch there was also evaluated for all synthesized nanoparticles. Figure 30 presents the results of the mass loss rate and conversion with temperature changes. For all samples can be noticed some catalytic oxidation in the LTR. However, for monometallic functionalized nanoparticles, two different peaks were observed. The NiO based nanoparticles presented one of their peaks at the highest temperatures in the HTR. On the other hand, the SiPd10 showed two consecutive peaks of similar magnitude just before the beginning of the HTR. SiPd5 presented one of these in the upper limit of the MTR and the other in the lower limit of the HTR. The bimetallic synthesized nanoparticles also showed two main peaks in the MTR. However, a third peak of less magnitude can be seen before 300°C in the MTR and can be associated with the catalytic decomposition of the resins [157]. The temperature of the begging of the catalytic oxidation of pitch follow the order SiNi5Pd5 < SiNi3.3Pd3.3 < SiPd10 < SiPd5 < SiNi10 <SiNi5. Despite the previously detailed limitations of this analysis concerning the high pitch to nanoparticle mass proportion, this is the same order shown in Figure 28 regarding *n*-C_7 asphaltenes oxidation decomposition. Finally, Figure 31 presents the activation energy calculated for all functionalized nanoparticles. It is worth mentioning that for all conversion values, the bimetallic nanoparticles presented the smallest $E_{\alpha OFW,}$

and their behavior is coherent with the previously discussed for a mixture of *n*-C_7 asphaltenes and resins [157].

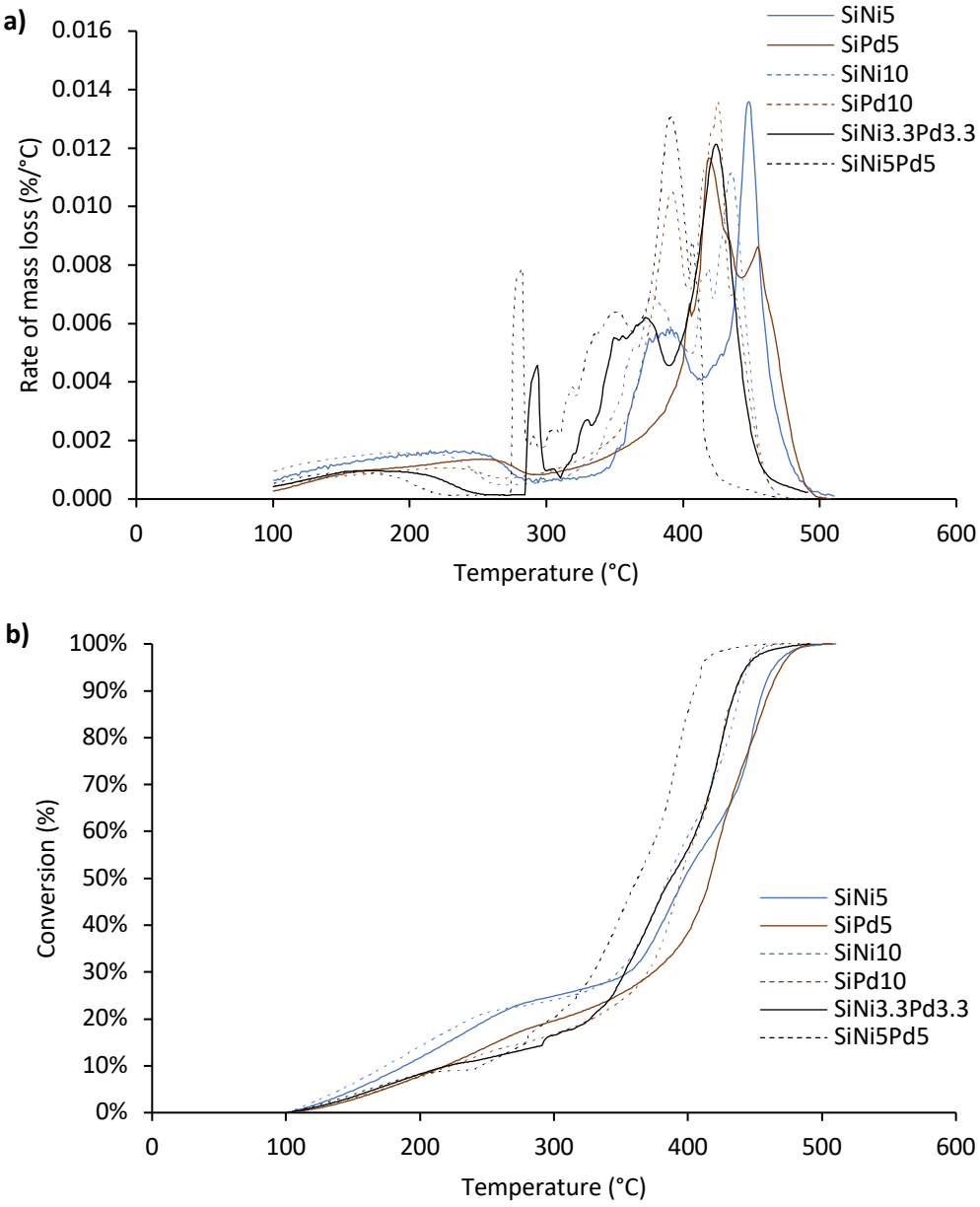

Figure 30. (a) Rate of mass loss and (b) pitch conversion for *e*-SDA process carried out with SiNi5, SiPd5, SiNi10, SiPd10, SiNi3.3Pd3.3 and SiNi5Pd5 nanoparticles with the airflow rate of 100 mL/min and the heating rate of 10°C/min.

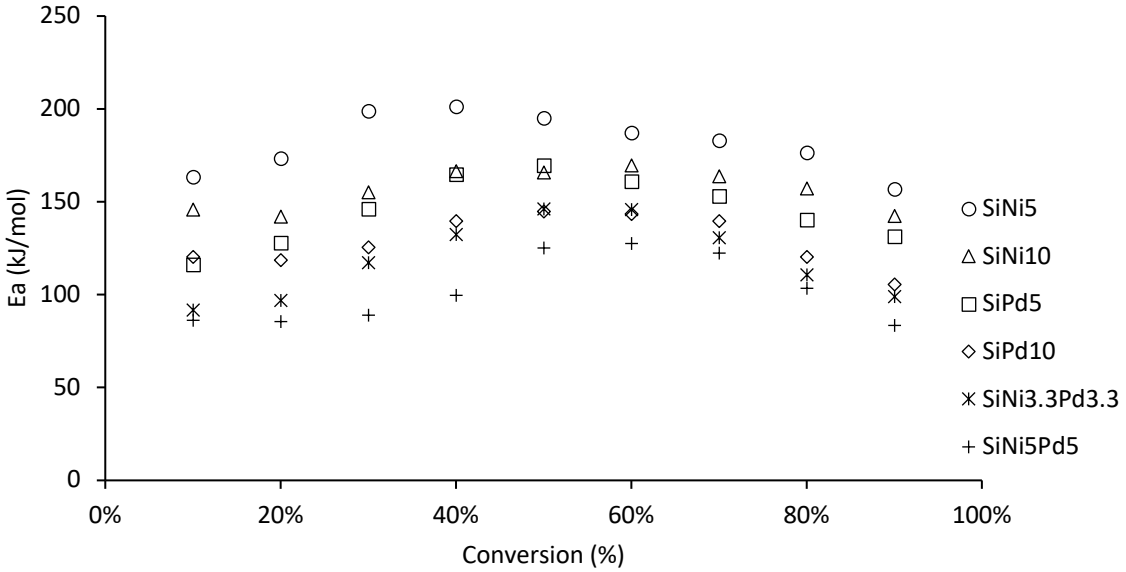

Figure 31. Activation energies estimated for thermal cracking of the pitch for SDA and *e*-SDA process carried out with SiNi5, SiNi10, SiPd5, SiPd10, SiNi3.3Pd3.3 and SiNi5Pd5 nanoparticles.

3.3.5. Optimization of NiO and PdO dosage

In chapter 2, the Si7 nanoparticles presented the highest capacity to improve DAO quality above the other evaluated chemical natures (Al and Ce) and size (silica of 200 nm). However, there also found that they weren´t the ones that showed the best properties as catalysts in the oxidations process. Considering the reported benefits of using NiO and PdO and their synergetic effect on *n*-C_7 asphaltene catalyst [30, 139, 152], there was carried on the SCMD described presented in Figure 22. The purpose was to enhance the catalytic properties of Si7 through the functionalization process with NiO and/or PdO. The statistical analysis was made using the Minitab software (version 19, Minitab, LLC, PA, USA), resulting in Equation 16. This mathematical expression relates the amount of nickel and palladium metal oxide functionalized onto Si7 nanoparticles and their impact on the temperature of the oxidation process beginning for *n*-C_7 asphaltenes.

Equation 16. $$OT_{asp} = 403.2 \cdot Si_{mf} + 274.1 \cdot Ni_{mf} + 220.5 \cdot Pd_{mf} - 195.8 \cdot Si_{mf} \cdot Ni_{mf} - 290.6 \cdot Si_{mf} \cdot Pd_{mf} - 221.6 \cdot Ni_{mf} \cdot Pd_{mf} - 540.0 \cdot Si_{mf} \cdot Ni_{mf} \cdot Pd_{mf}$$

where, Si_{mf}, Ni_{mf} and Pd_{mf} are the mass fraction of Si7, NiO and PdO expressed as decimals, respectively, with $Si_{mf} + Ni_{mf} + Pd_{mf} = 1$. OT_{asp} is the expected oxidation temperature of *n*-C_7 asphaltenes. The special cubic model described by Equation 16 validates the experimental data with $R^2 = 0.98$. With this expression and carrying on an optimization process, there was found that 3.20 wt% of nickel and 5.45 wt% of palladium on the Si7 surface (SiNi3.2Pd5.5) minimizes the *n*-C_7 asphaltene oxidation process beginning. For this metal oxide load, the statistical analysis of the SCMD predicted a minimal temperature for the start of catalytic oxidation of 181.1 °C. Precisely, Figure 32 shows the contour plot for the expected value of the temperature when the oxidation

process begins and shows a tendency to obtain minimal values for bimetallic mixtures made with higher wt% of Pd than Ni.

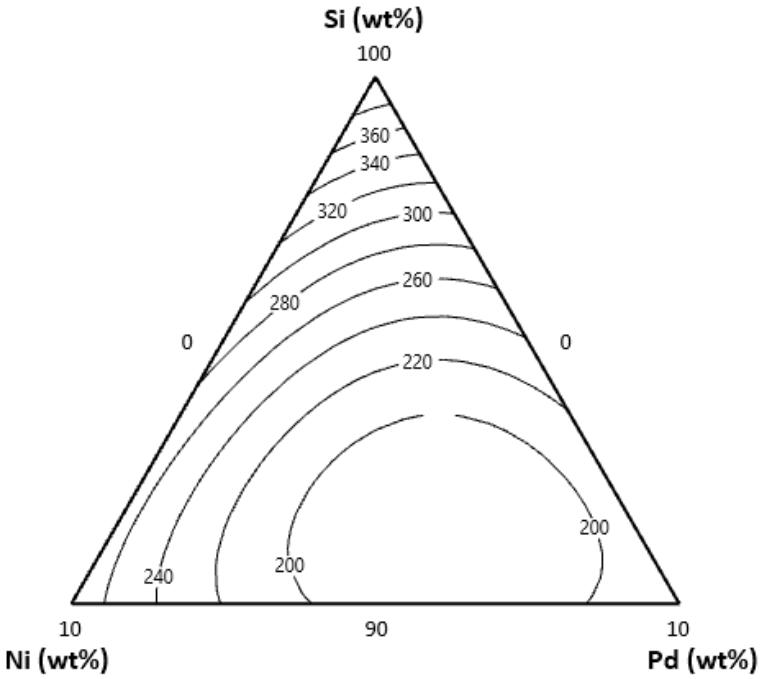

Figure 32. Contour plot for the expected temperature values at the beginning of the oxidation process.

3.4. Partial conclusions

There was successfully proposed, executed and analyzed a simplex-centroid mixture design (SCMD) to optimize the NiO and PdO load onto the Si7 surface. Three groups of results in the *n*-C_7 asphaltene adsorption properties and the qualities of DAO samples can be noticed. The monometallic Pd nanoparticles and the bimetallic nanoparticles presented adsorption isotherms type Ib [172] with the highest adsorption affinity for the bimetallic ones. For the NiO monometallic nanoparticles, adsorption isotherms type III were obtained, which can be attributed to the mayor crystal size of nickel oxide and their higher hydrodynamic diameter. These results confirmed the relationship between the parameter q_m for the maximum adsorption capacity of nanoparticles and the quality of the obtained DAO samples.

According to the proposed SCMD, all the synthesized nanoparticles presented a reduction in the temperature of the catalytic oxidation of *n*-C_7 asphaltenes. The best results correspond to the bimetallic nanoparticles, especially to SiNi5Pd5. With all those obtained temperatures as the response variable, a statistical analysis was carried out to predict SiNi3.2Pd5.5 as the nanoparticles that minimize the temperature for the beginning of asphaltene catalytic oxidation. This temperature was estimated at 181.1 °C.

4. Optimized nanoparticles and their impact on DAO quality and catalytic decomposition of the pitch under isothermal conditions

In chapter 1, it was evaluated the role of adding nanoparticles to a typical SDA. A new *e*-SDA process was proposed that improved DAO quality for all operation conditions like the solvent to oil ratio, type of solvent, temperature and nanoparticle dosage. However, the role of the chemical nature of the used nanoparticle and the relationships between the asphaltene adsorption properties and the quality of DAO samples remained unknown. In this sense, chapter 2 assessed those matters and evaluated the pitch catalytic oxidation process. Precisely, the importance of pitch as a product of low value for the traditional SDA process [69, 75, 155] leads to the improvement of its catalytic oxidation through a SCMD accompanied by statistical analysis. The result obtained in chapter 3 showed that NiO and PdO bimetallic functionalization over Si7 could reduce the temperature of oxidative decomposition of *n*-C_7 asphaltenes by more than half, considering the sample without nanoparticles. These results also allowed for predicting the minimum temperature for the oxidation of the *n*-C_7 asphaltene oxidation process for the combination SiNi3.2Pd5.5.

In this sense, this chapter presented the results of the synthesizing process for SiNi3.2Pd5.5 nanoparticles. These were subjected to adsorption-catalytic oxidation cycles for the adsorption of *n*-C_7 asphaltenes and their thermal decomposition. The same for the *e*-SDA process and the DAO quality evaluation and pitch catalytic oxidation process. In addition to the thermal oxidative process carried out on all samples and depending on temperature, an isothermal process was carried out. This assessment was proposed according to the pitch's catalytic oxidation process on a pilot or industrial scale, likely at a fixed temperature. In these tests, there was also evaluated gas production, and the benefits of using nanomaterials can be seen.

4.1. Materials and methods

4.1.1. Materials

All the materials and methods described in chapters 2 and 3 were used and applied in this chapter. There were used Si7 nanoparticles, selected as the support for the functionalization. SiNi5Pd5 was evaluated for being the one with the best performance related to catalytic oxidation of *n*-C_7 asphaltenes of the all synthesized nanomaterials used for the SCMD. The optimized nanoparticles (SiNi3.2Pd5.5) were functionalized following the procedures described in section 3.1.2.1. The same EHO was used for *n*-C_7 asphaltene extraction and the different deasphalting processes. In the same way, previously described methods were employed related to nanoparticle characterization and those once used to evaluate n-C7 asphaltene adsorption and catalytic oxidation, just as DAO quality and pitch oxidative thermal decomposition. For these reasons, there are only detailed materials and methods used in this chapter and not yet described.

4.1.2. Methods

4.1.2.1. *n*-C_7 asphaltene and pitch isothermal oxidation in the absence and presence of nanoparticles

Chapter 2 described the method used to evaluate the catalytic oxidation of *n*-C_7 asphaltenes and pitch with and without nanoparticles as a function of the temperature. However, for the *e*-SDA process schematized in Figure 1, it would have more sense that the catalytic conversion will be carried out at a fixed temperature. For this reason, there was followed the procedure described by Medina et al. [152] for assessing isothermal catalytic oxidation using a Q50 TGA analyzer (TA Instruments, Inc., New Castle, DE, USA) with a constant airflow of 100 mL/min. According to observed results in the previous chapters for virgin *n*-C_7 asphaltenes and SDA pitch, the temperatures were set at 380 °C, 390 °C and 400 °C. The refractory nature of these compounds and the impact on this behavior in the presence of resins was also considered, as seen in the different obtained pitch samples [139, 157]. 180 °C, 190 °C and 200 °C were selected as temperatures for evaluating the impact of nanomaterials in the catalytic oxidation of *n*-C_7 asphaltenes. The same relation of both was used for all experiments with 0.2 mg/m^2. There were used for *e*-SDA pitch samples 330 °C, 340 °C and 350 °C attending to obtained results of section 3.3.4. As previously explained, the ratio between nanomaterials and pitch can't be fixed for these samples. The sample mass in the TGA analyzer was set at 5 mg to avoid diffusion limitations [112].

4.1.2.2. Evaluation of the produced gases in the catalytic oxidation process

The analysis of the gaseous products involved in the catalytic oxidation experiments was made using an IR-Affinity-1 FTIR device (Shimadzu, Kyoto, Japan) with a gas cell. This device was operated in transmission mode from 4000 cm-1 to 100 cm-1 at a resolution of 2 cm-1 and ran ten scans per minute. CH4, CO, light hydrocarbon, and CO2 were the followed gases, corresponding to those associated with the asphaltenes catalytic decomposition [156, 157].

4.1.2.3. Nanoparticles regeneration

SiNi5Pd5 and SiNi3.2Pd5.5 were evaluated in five different cycles of *n*-C_7 asphaltene adsorption and catalytic oxidation. DAO quality and yield were also assessed for these samples, as their performance related to pitch oxidative decomposition. The regeneration of the nanoparticles contained in the *e*-SDA pitch was performed in a tubular furnace (Thermo Scientific Lindberg/Blue, Waltham, MA, USA) at 400 °C for 2 h with a constant airflow of 100 mL/min. A sample of each *e*-SDA pitch was taken in each cycle to perform the thermogravimetric evaluation with gaseous products assessment.

4.2. Modeling. Estimation of isothermal activation energy

Following the isothermal procedure described by Nassar et al. [194], the effective activation energy (EαISO) can be found according to the following expressions.

Equation 17. $$\frac{d\alpha}{dt} = K_\alpha e^{\left(-\frac{E_{\alpha ISO}}{RT}\right)} f(\alpha)$$

Equation 18. $$\alpha = \frac{m_0 - m_t}{m_0 - m_f}$$

Where, α is the conversion degree described by Equation 18 with m_t the current mass of the sample at a determined time *t*, while the rest of the components stands as abovementioned. K_α (s^{-1}) is the pre-exponential factor, $E_{\alpha ISO}$ (kJ/mol) is the effective activation energy for a constant degree of conversion, *R* is the ideal gas constant and was defined previously just like *T*, *f(α)* is the reaction mechanism function, and *dα/dt* is the reaction rate. Under the isothermal conditions under which this analysis was performed. The separation of variables and the integration of Equation 17 takes the form of Equation 19.

Equation 19. $$g(\alpha) = \int_0^\alpha \frac{d\alpha}{f(\alpha)} = \int_0^t K_\alpha e^{\left(\frac{-E_\alpha}{RT}\right)} dt = K_\alpha \, e^{\left(\frac{-E_\alpha}{RT}\right)} t$$

The upper equation can be written as Equation 20 after assuming the value of $E_{\alpha ISO}$ constant and taking the natural logarithm for both sides.

Equation 20. $$ln\left(t_{a,i}\right) = ln\left(\frac{g(\alpha)}{K_\alpha}\right) + \frac{E_{\alpha ISO}}{RT_i}$$

Plotting $\ln(t_{a,i})$ vs. $1/T_i$ allows calculating $E_{\alpha ISO}$ from the slope of the obtained plot.

4.3. Results

4.3.1. Optimized nanoparticles characterization

SiNi3.2Pd5.5 were synthesized and characterized according to the proposed SCMD. The statistical analysis results lead to synthesizing this nanoparticle with 3.20 wt% of nickel and 5.45 wt% of palladium. All this is to obtain the minimal temperature from *n*-C_7 asphaltene catalytic oxidation, considering that the predicted was 181.1 °C. The followed process for the functionalization was detailed in section 3.1.2.1. The SiNi3.2Pd5.5 showed a hydrodynamic diameter (dp_{50DLS}) of 25 nm and a S_{BET} of 316.3 m^2/g. The last shows a deviation of 2.7% respected with the expected S_{BET} shown in Figure 33, which relates the expected surface area values with the proposed SCMD.

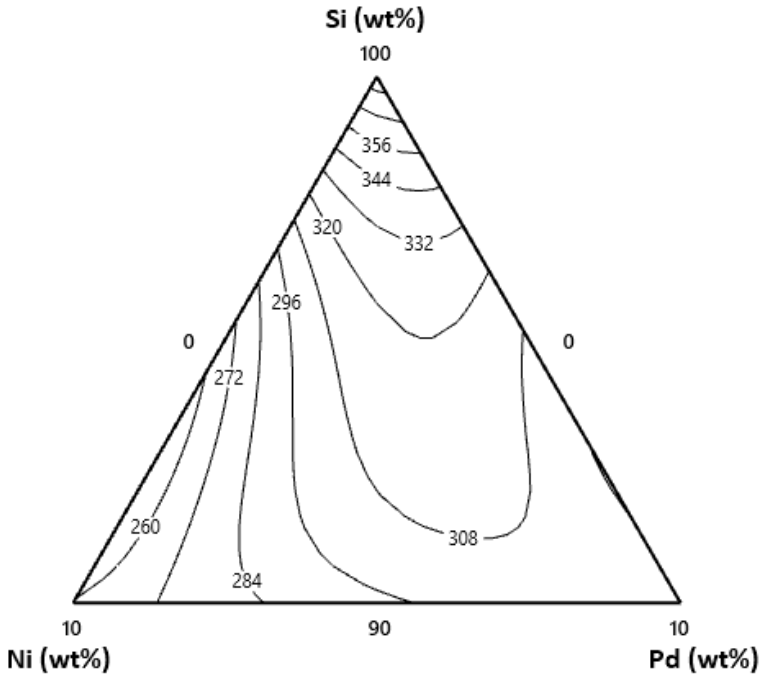

Figure 33. Contour plot for the expected values of S_{BET} according to the proposed SCMD.

4.3.2. *n*-C_7 asphaltenes adsorption and DAO yield and quality

The performance of optimized nanoparticles (SiNi3.2N5.5) was evaluated through *n*-C_7 asphaltene adsorption and catalytic oxidation. Its impact on the DAO yield and quality and catalytic decomposition of the *e*-SDA pitch was also quantified. All these processes were carried out through 5 cycles in which these nanoparticles were regenerated and retested consecutively. Figure 34 presented adsorption isotherms. A change in the adsorption isotherm for the second cycle can be noticed. For C_e of 50 mg/L and below, the adsorbed *n*-C_7 asphaltenes remain approximately constant. Above 250 mg/L, the adsorption falls around 3% versus observed for the first cycle. The adsorption isotherms for cycles 3, 4 and 5 follow the same form for cycle 2. Sintering phenomena can explain the observed slight reduction in SiNi3.2Pd5.5 adsorption capacity after the first regeneration. After the first regeneration of used nanoparticles by catalytic oxidation of adsorbed Quinolin-65, Nassar et al. [195] reported a rise in NiO crystal size. However, for the next regenerations, this size remains the same. Other authors found a reduction of 30 % in the S_{BET} for NiO supported nanoparticles with tree cycles [196]. However, this reduction is inhibited by adding PdO. Hence, the first catalytic regeneration of SiNi3.2Pd5.5 could cause some growth in NiO crystal size and remains stable for the rest of the cycles, even for the size controlling effect associated with PdO.

Table 16 presents the fitted parameters *H*, *K* and q_m of the SLE model in which the previously described behavior can be noticed. *H* showed a small rise after the first cycle, implying a little reduction in the affinity of the couple adsorbent-adsorbant [154]. *K* and q_m parameters fall after the first regeneration, explaining the observed adsorption isotherms. Thus, a reduction of the *n*-C_7

asphaltenes tendency to form aggregates after being adsorbed and a slight fall in the maximum adsorption capacity Campo [154] is expected.

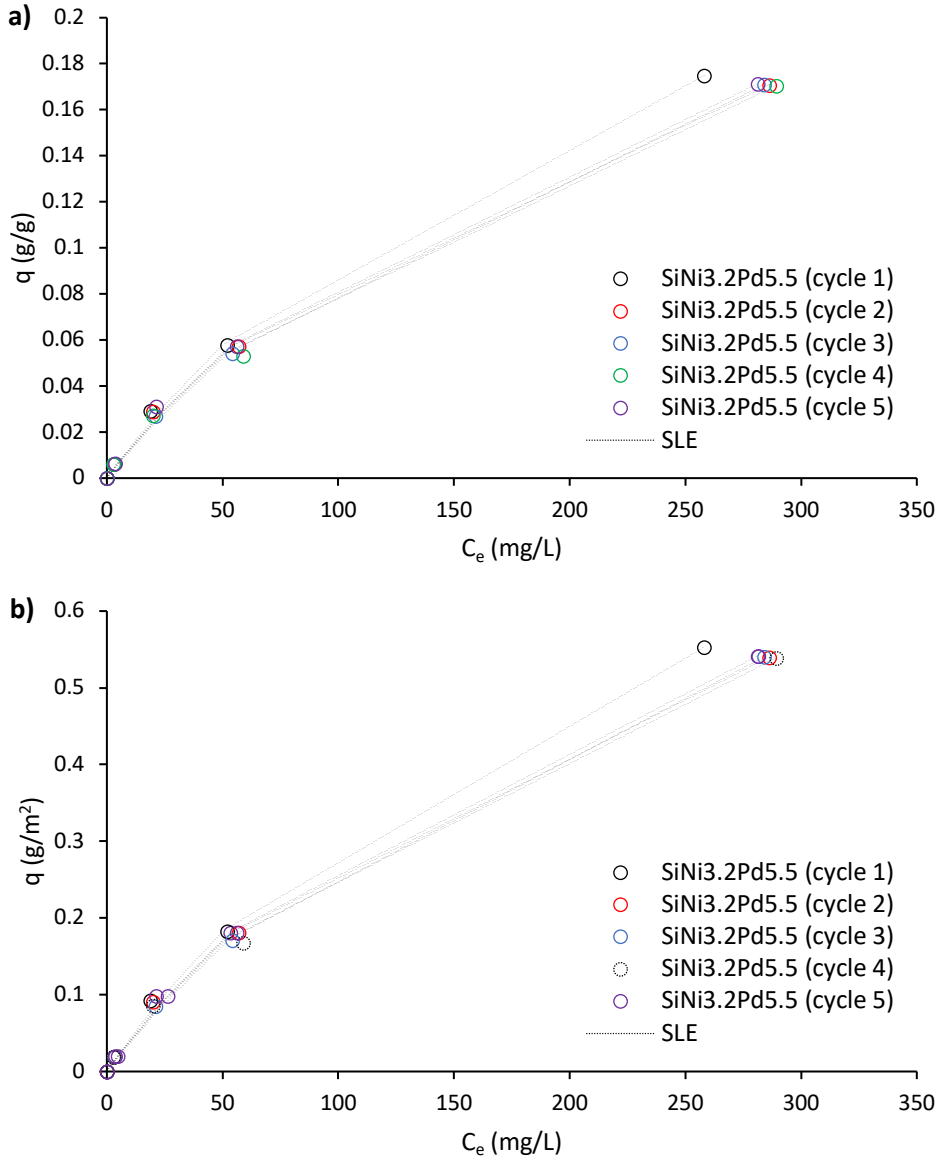

Figure 34. Adsorption isotherms of *n*-C_7 asphaltenes in SiNi3.2Pd5.5 expressed in (a) g/g and (b) mg/m^2.

Table 16. Estimated values of the SLE model parameters for the adsorption isotherms of *n*-C_7 asphaltenes onto SiNi3.2Pd5.5.

Nanomaterial	***H*** **± 0.01 (mg/g)**	***K*** **± 0.05 (g/g) x 10^{-4}**	***q_m*** **± 0.01 (g/g)**	**R^2**	**RSME%**
SiNi3.2Pd5.5 Cycle 1	0.81	0.97	0.61	0.996	0.4
SiNi3.2Pd5.5 Cycle 2	0.89	0.34	0.57	0.998	0.3
SiNi3.2Pd5.5 Cycle 3	0.92	0.31	0.55	0.999	0.2

SiNi3.2Pd5.5 Cycle 4	0.87	0.35	0.56	0.998	0.3
SiNi3.2Pd5.5 Cycle 5	0.86	0.36	0.57	0.997	0.3

Previously, the relationship between the *n*-C_7 asphaltene adsorption and the DAO yield and quality was analyzed. Table 17 summarizes the result of the *e*-SDA process DAO yield and quality for optimized nanoparticles along 5 cycles. It can be noticed that DAO yields for SiNi3.2Pd5.5 are approximately 50.6%, a closely lower value than observed for the SiNi3.3Pd3.3 and SiNi5Pd5 nanoparticles. The same situation was presented by *n*-C_7 asphaltene content, °API and viscosity related to DAO quality. Regarding the value of the sulfur content and Conradson carbon content for these samples, those were approximately the same as that previously presented for the non-optimized bimetallic nanoparticles. Figure 35 shows the expected values for all these properties attending the proposed SCMD. It can be easily seen that all measured values are close to the expected.

Table 17. DAO yield and quality of DAO obtained by *e*-SDA process with SiNi3.2Pd5.5 nanoparticles on 5 consecutive cycles of regeneration.

Nanomaterial	DAO yield (%)	DAO quality		
		n-C_7 asphaltene (wt%)	°API	Viscosity (cP)
SiNi3.2Pd5.5 Cycle 1	50.52	4.59	16.40	7 861
SiNi3.2Pd5.5 Cycle 2	50.68	4.84	16.37	7 853
SiNi3.2Pd5.5 Cycle 3	50.72	4.76	16.39	7 881
SiNi3.2Pd5.5 Cycle 4	50.93	4.95	16.45	7 894
SiNi3.2Pd5.5 Cycle 5	50.81	4.66	16.32	7 879

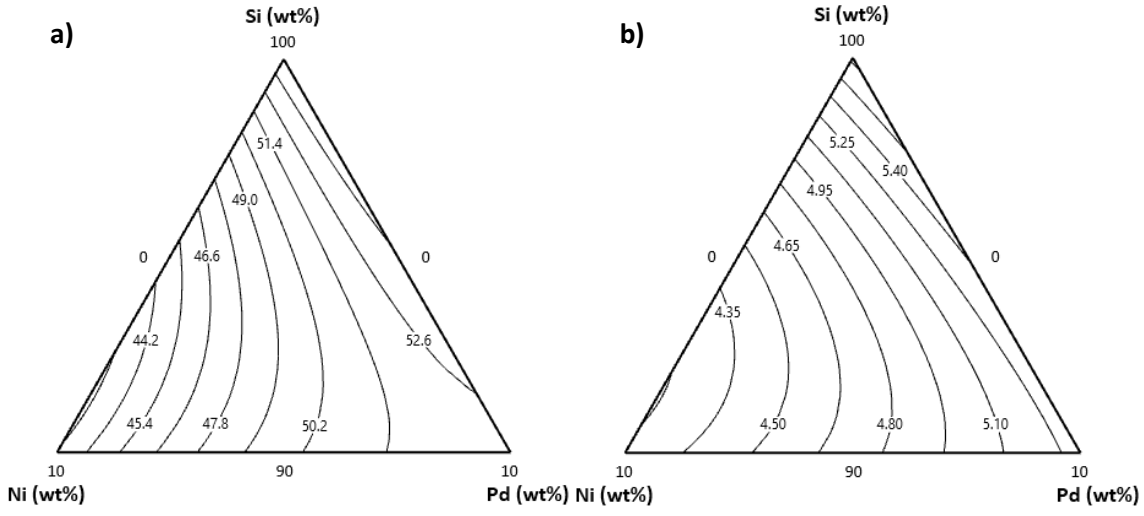

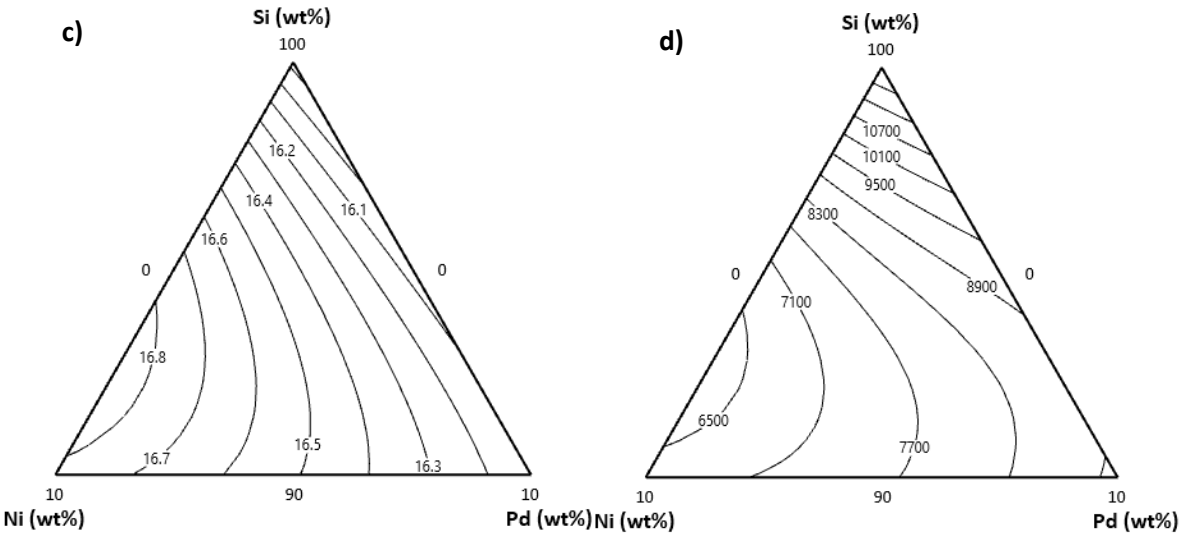

Figure 35. Contour plot for the expected values of (a) DAO yield (%) and DAO quality determined through (b) asphaltene content (%), (c) API gravity and (d) viscosity (cP).

4.3.3. *n*-C_7 asphaltenes and pitch catalytic decomposition

The optimization of NiO and PdO dosage carried out with the proposed SCMD was made with the primary objective of improving the catalytic properties of Si7 nanoparticles through functionalization. There was found that SiNi3.2Pd5.5 is expected to be the mixture that minimizes the initial temperature for the *n*-C_7 asphaltenes oxidation process. Figure 36 presents the *n*-C_7 asphaltene conversion and the mass loss rate for these nanoparticles in their first cycle. One main peak in the LTR can be noticed, as observed for SiNi3.3Pd3.3 and SiNi5Pd5. The temperature at the beginning of the oxidation process is approximately 185.0°C. This value is the minimal reported for all the evaluated samples and is near the predicted value by the SCMD of 181.1°C. Precisely, Figure 32 shows the contour plot for the expected temperature value when the oxidation process begins and shows that the minimal values can be obtained for mixtures made with a higher wt% of Pd than Ni. These results agree with those reported by the literature for silica and cerium supported nanoparticles [30, 138, 139, 152]. It is worth mentioning that in the evaluated cycles from 2 to 5, the found temperature of the beginning of the catalytic process are approximately the same and were located at 192 °C. The possible growth of NiO crystal after the first regeneration can explain these results because smaller sizes can be associated with a better catalytic oxidation performance [195].

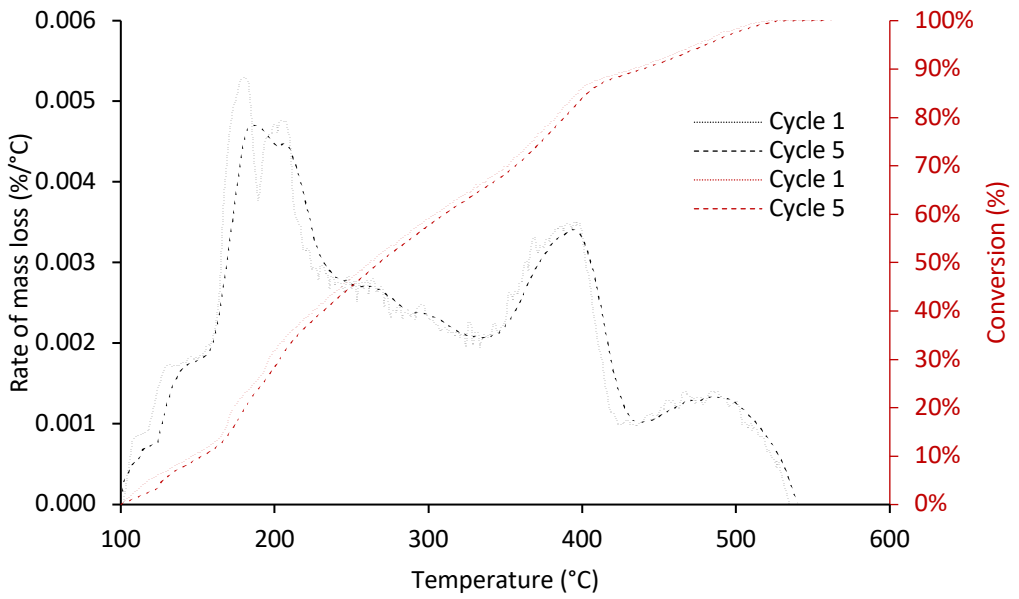

Figure 36. Mass loss and conversion rate for *n*-C_7 asphaltenes as a function of temperature in the presence of SiNi3.2Pd5.5 nanoparticles with the airflow rate of 100 mL/min, the heating rate of 10°C/min and *n*-C_7 asphaltene loading 0.2 mg/m^2.

Figure 37 presents the pitch oxidative decomposition process for the first cycle of SiNi3.2Pd5.5 optimized nanoparticles. The mass loss rate showed similar behavior to that observed in Figure 30 for the other bimetallic synthesized nanoparticles. However, the beginning of the oxidation process is 7% inferior to the observed for SiNi5Pd5. The optimized nanoparticles presented some catalytic activity in the LTR and three peaks in the MTR. Similar behaviors are reported in the literature for the oxidation process of asphaltene and resin mixtures [157]. There was a rise in 6 °C for the temperature of the catalytic oxidation beginning, passing from 328 °C at cycle 1 to 334 °C in the following. Figure 38 shows the activation energies for catalytic decomposition of *n*C_7 asphaltenes and pitch carried out with SiNi3.2Pd5.5 from cycles 1 to 5. Regarding *n*-C_7 asphaltene, the $E_{\alpha OFW}$ follows the same behavior described by the other bimetallic functionalized nanoparticles. For the pitch oxidation process, this behavior was also noticed. However, the activation energies showed the same trend that those presented by Lozano et al. [157] for mixtures of *n*-C_7 asphaltenes and resins.

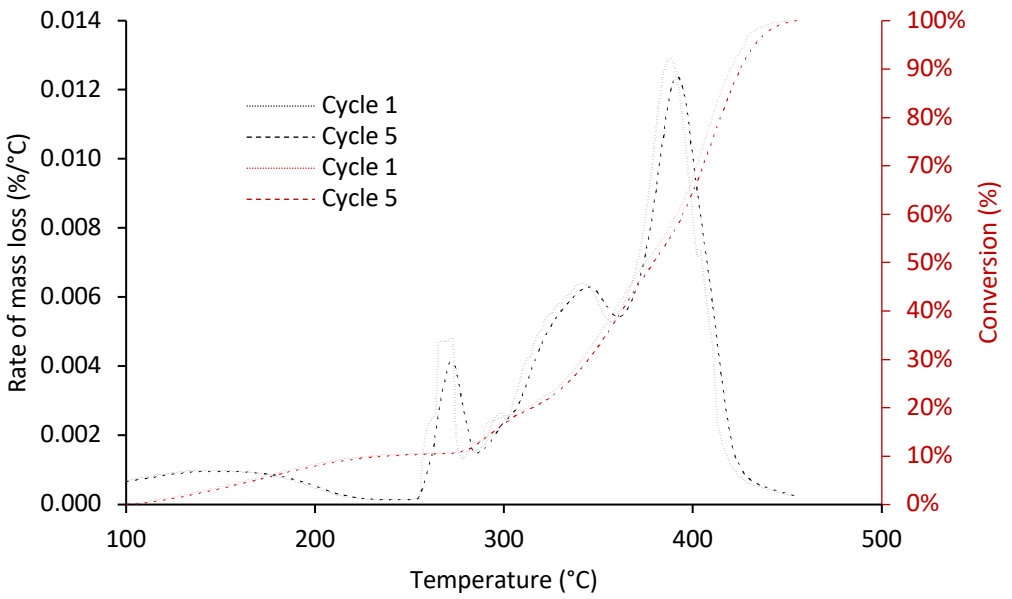

Figure 37. Rate of mass loss and conversion of the pitch for *e*-SDA process as a function of temperature in the presence of SiNi3.2Pd5.5 nanoparticles with the airflow rate of 100 mL/min, the heating rate of 10°C/min and *n*-C_7 asphaltene loading 0.2 mg/m^2.

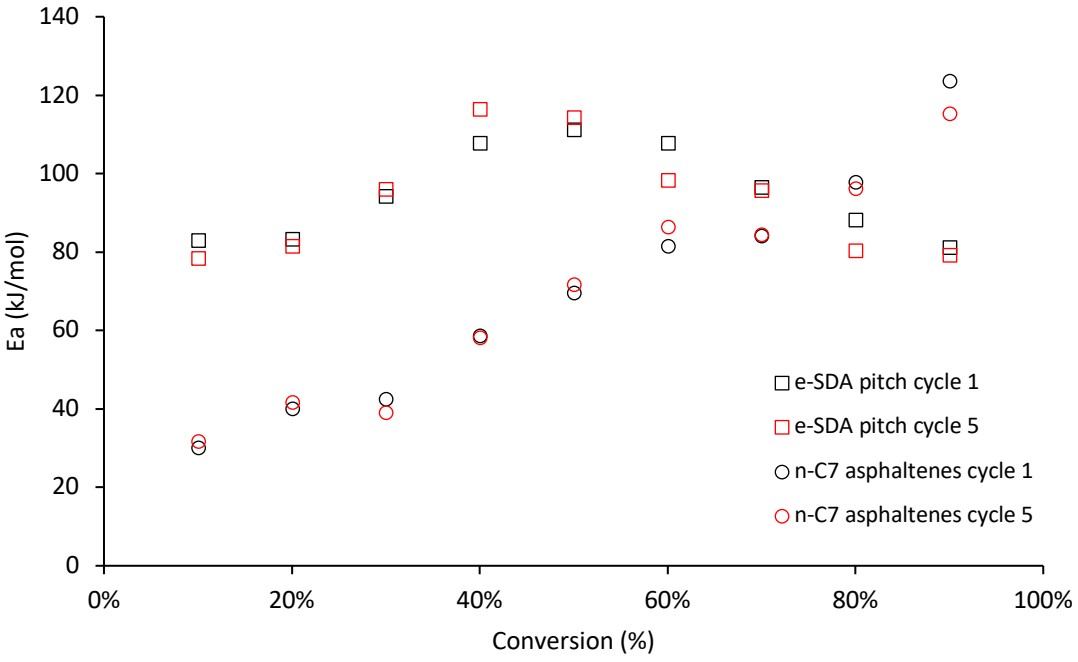

Figure 38. Activation energies evaluated for thermal cracking of *n*-C_7 asphaltenes and pitch for *e*-SDA process carried out with SiNi3.2Pd5.5 nanoparticles in cycles from 1 and 5.

4.3.4. *n*-C_7 asphaltenes and pitch isothermal catalytic decomposition and gaseous products

The nature of the proposed *e*-SDA process and its schematic design were presented at the beginning of chapter 1. The catalytical oxidation of pitch for this technology will be carried out at a fixed temperature. Thus, the isothermal oxidative decomposition process was assessed for *n*-C_7 asphaltene and the pitch in the presence and absence of nanomaterials. Figure 39 illustrates virgin *n*-C_7 asphaltenes conversion and for those adsorbed onto Si7, SiNi5Pd5 and SiNi3.2Pd5.5. The first was evaluated to analyze the support behavior without the NiO and PdO. The bimetallic nanoparticle with a dosage of 5 wt% of each metal was assessed as the second with the best catalytic properties. The results presented in Figure 39 show that bimetallic functionalized nanoparticles generate a catalytic effect noticed in the decomposition time. The lowest was obtained for SiN3.2Pd5.5 in their cycle 1 and 5. These results obtained at 190 °C imply a significant change concerning *n*-C_7 asphaltenes, which were evaluated at 390 °C. Precisely, this temperature setting for nanoparticle evaluation could be responsible for the low performance of Si7, which showed catalytic behavior at 400 °C, according to Figure 18. For SiNi5Pd5 and SiNi3.2Pd5.5, these results agree with those presented in Figure 28 and Figure 36, which showed the oxidative decomposition depending on temperature.

SiNi3.2Pd5.5 presented the best catalytic effect achieving a 90 % *n*-C_7 asphaltene conversion in around 120 min at 190 °C. SiNi3.2Pd5.5 was the only nanomaterial that led to the total decomposition of asphaltenes for both evaluated cycles. It can be noticed for SiNi5Pd5 nanoparticles a remarkable performance, with a conversion of 96.1 %. Catalytic decomposition for Si7 at 190 °C was inferior to 25 %, while for *n*-C_7 asphaltenes was 45.7 % at 390 °C. All these differences in catalytic activity can be attributed to the different interactions between the last and nanoparticles [30, 138, 139, 152]. For all the bimetallic nanoparticles, the best catalytic results could be due to the inhibition of the growth of Pd and Ni crystals by their synergetic effect [140, 196].

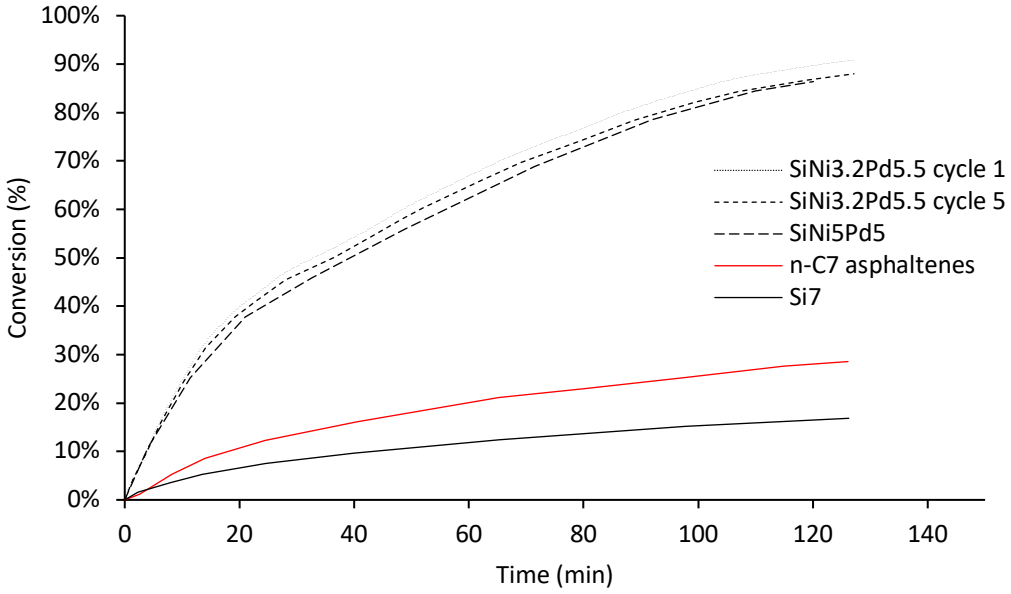

Figure 39. Isothermal conversion for catalytic oxidation of *n*-C_7 asphaltenes in the absence (390 °C) and presence (190 °C) of Si7, SiNi5Pd5 and SiNi3.2Pd5.5 at cycles 1 and 5. Airflow rate = 100 mL/min and *n*-C_7 loading 0.2 mg/m^2.

Figure 40 presents the evolution of gaseous products during the catalytic oxidation process of *n*-C_7 asphaltenes without and with Si7, SiNi5Pd5 and SiNi3.2Pd5.5 nanoparticles. The measurements were made with an FTIR device coupled to the TGA for isothermic conditions. Each panel presents the result for a different product: CH4, CO, light hydrocarbon (LHC) and CO_2. For each one, the measures were normalized concerning their higher value to compare. SiNi3.2Pd5.5 presented the highest values for all gaseous products at its first cycle, closely followed by itself at cycle 5 and SiNi5Pd5. Also, for all gaseous products, their production followed the same trend. All these results are coherent with those previously reported in this chapter and chapter 3. Precisely an insight into this situation can be found in the SCMD and the contour plot in Figure 32. It can be seen a similar expected result for SiNi3.2Pd5.5 and SiNi5Pd5, with slightly better performance for optimized nanoparticles. When comparing the gases between them, CO_2 presented the higher values due to oxygen in the airflow favoring its formation [139].

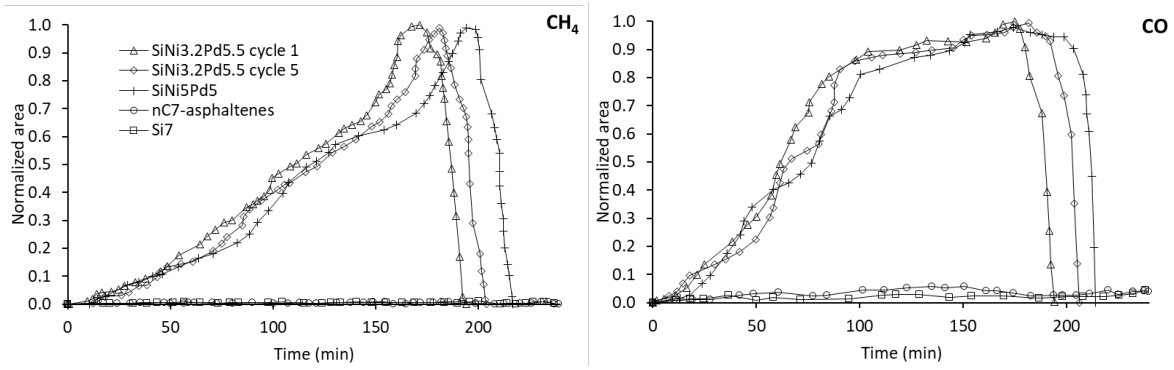

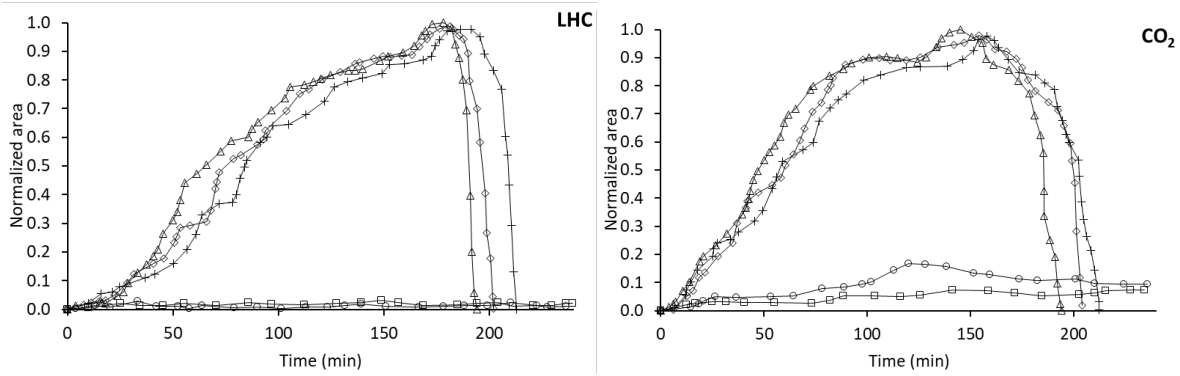

Figure 40. Evolution profiles of gaseous products during catalytic oxidation under isothermal conditions of *n*-C_7 asphaltenes in the absence (390 °C) and presence (190 °C) of Si7, SiNi5Pd5 and SiNi3.2Pd5.5 at cycle 1 and 5. Airflow rate = 100 mL/min and *n*-C_7 loading 0.2 mg/m^2.

Figure 41 presents the result of SDA pitch catalytic oxidation carried out at 390 °C and 340 °C for Si7, SiNi5Pd5 and SiNi3.2Pd5.5 (cycles 1 and 5). The SDA sample, obtained without nanoparticles, only achieved a conversion of 56.7 %, a higher value than the obtained for virgin *n*-C_7 asphaltenes. Considering that pitch is mainly a mixture of these and resins, this behavior agrees with those observed by Lozano and coworkers [157]. Although they use different methods, they found that the conversion depends on the wt% of the mixture of these two compounds. There was also observed that catalytic oxidation in the presence of resins was lower than reported for virgin *n*-C_7 asphaltene at 390 °C. At higher temperatures, this situation may change.

As previously explained, the temperature set for the evaluating nanomaterials was selected according to Figure 37. There can be seen that the catalytic oxidation process for SiNi3.2Pd5.5 begins at 340 °C. This difference with the observed for *n*-C_7 asphaltene oxidation obeys the enormous pitch load in nanoparticles, reaching 24 mg/m^2 in the case of Si7. Thus, in this scenario, Si3.2NiPd presented the best catalytic performance achieving 70 % conversion in 120 min at 340 °C and being the only sample to reach the total conversion in both cycles. SiNi5Pd5 showed a similar trend and reached 92.5 % of conversion. Finally, Si7 showed a higher catalyst than for *n*-C_7 asphaltenes but is related to the rising of the experiment temperature.

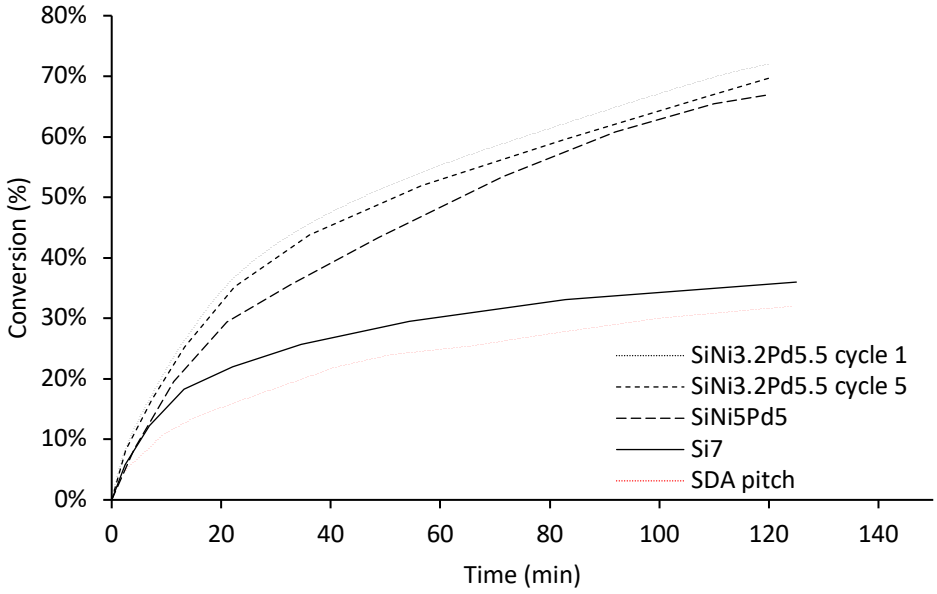

Figure 41. Isothermal conversion for catalytic oxidation of pitch in the absence (390 °C) and presence (340 °C) of Si7, SiNi5Pd5 and SiNi3.2Pd5.5 at cycles 1 and 5. Airflow rate = 100 mL/min.

The evolution of gaseous products in isothermal conditions was assessed for SDA and *e*-SDA pitch obtained with Si7, SiNi3.2Pd5.5 and SiNi5Pd5. These results are presented in Figure 42. Summarizing, these results show the same trend found described for *n*-C_7 asphaltenes. However, a change was observed at the beginning of the production of all gases. The slope is higher due to the catalytic decomposition of the pitch. The reason is the presence of resins in all pitch samples. These mixtures showed a more significant catalytic decomposition than *n*-C_7 asphaltene at temperatures below 400 °C [157]. Thus, there are the highest gaseous production rates at the beginning of catalytic oxidation of pitch. Also, can be noticed a bigger production of all analyzed gases for SDA and Si7, attributable to the highest isothermal temperature of 340 °C that was used for evaluating *n*-C_7 asphaltenes.

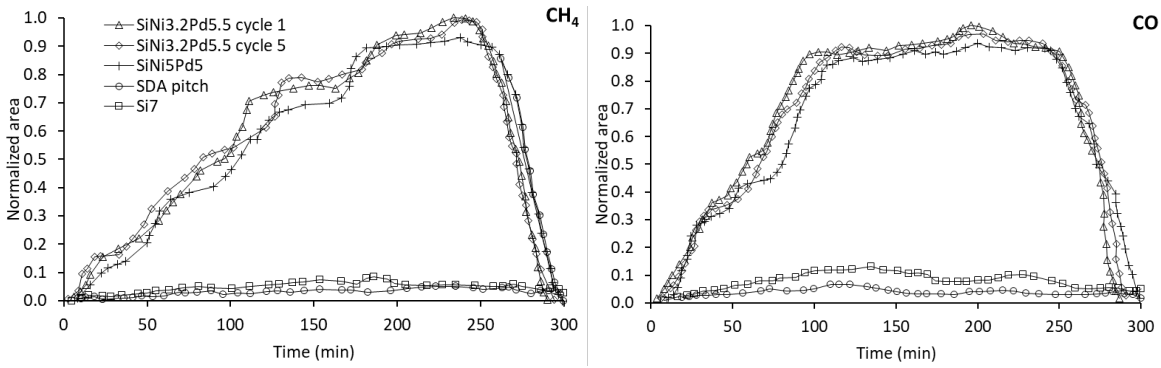

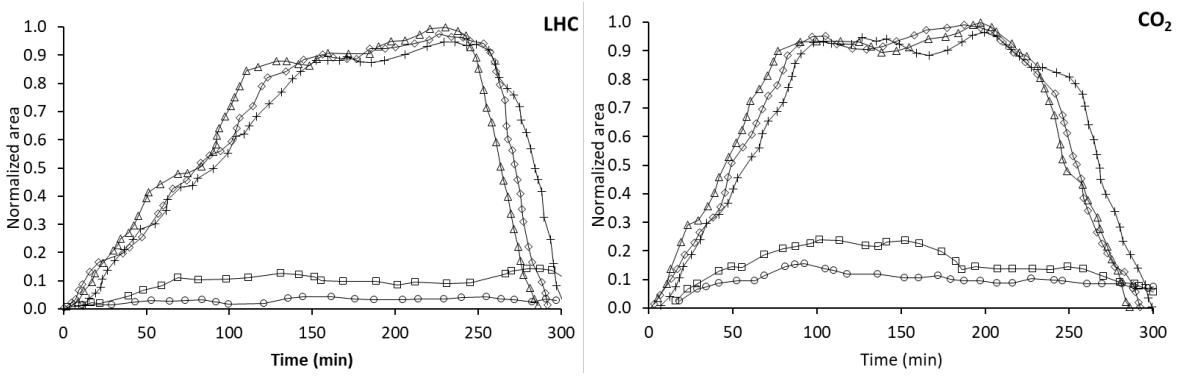

Figure 42. Evolution profiles of gaseous products during catalytic oxidation under isothermal conditions of SDA pitch in the absence (390 °C) and presence (340 °C) of Si7, SiNi5Pd5 and SiNi3.2Pd5.5 at cycles 1 and 5. Airflow rate = 100 mL/min.

As previously mentioned, for *n*-C_7 asphaltene and pitch, the only material that achieved the total conversion was the optimized nanoparticles SiNi3.2Pd5.5. Despite the good results observed for SiNi5Pd5, the lack of a complete catalytic conversion reaffirms the success of the optimization process. The isothermal measures made to the Si7 sample clarify the benefits of adding NiO and PdO to its surface, related to the obtained gaseous products that were higher for the SiNi3.3Pd3.2 sample. Finally, Figure 43 presented the plot of $\ln(t_{\alpha,i})$ vs. $1/T$ and from its slope, the effective isothermal activation energies ($E_{\alpha.isoT}$) was calculated. Table 18 summarizes these results. As can be seen, the $E_{\alpha.isoT}$ value follows the order SiNi3.2Pd5.5 < SiNi5Pd5 < Si7 < *n*-C_7 asphaltenes or pitch. It's worth mentioning that these results agree with the previously reported for the activation energy calculated through the OFW isoconversional method, for conversion percentages of 40 % or below.

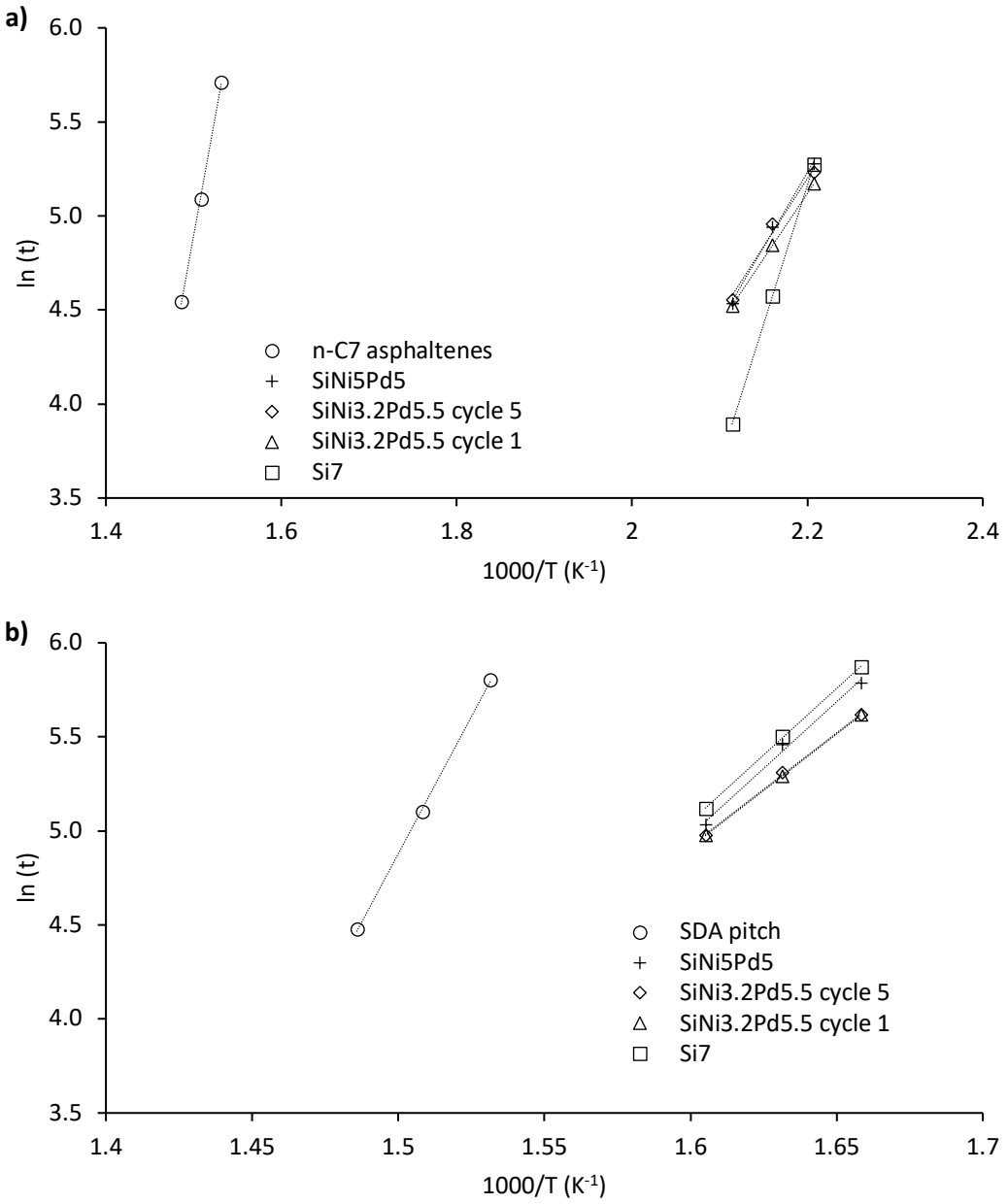

Figure 43. Arrhenius plot for the isothermal model of catalytic and thermal oxidation of a) *n*-C_7 asphaltene and b) pitch. All in the presence and absence of Si7, SiNi5Pd5 and SiNi3.2Pd5.5 (cycles 1 and 5).

Table 18. Estimated effective isothermal energy ($E_{\alpha.isoT}$) for catalytic oxidation of *n*-C_7 asphaltene and pitch. All in the presence and absence of Si7, SiNi5Pd5 and SiNi3.2Pd5.5 (cycles 1 and 5).

Sample		Temperature (°C)	$E_{\alpha.isoT}$ (kJ)
n-C_7 asphaltenes	Virgin	380 390 400	213.3

		180	
	Si7	190	123.0
		200	
		180	
	SiNi5Pd5	190	66.3
		200	
		180	
	SiNi3.2Pd5.5 cycle 1	190	57.8
		200	
		180	
	SiNi3.2Pd5.5 cycle 5	190	60.2
		200	
		380	
	Virgin	390	242.1
		400	
		330	
	Si7	340	167.2
		350	
		330	
Pitch	SiNi5Pd5	340	118.0
		350	
		330	
	SiNi3.2Pd5.5 cycle 1	340	99.8
		350	
		330	
	SiNi3.2Pd5.5 cycle 5	340	105.2
		350	

4.4. Partial conclusions

There was executed the proposed SCMD and the statistical analysis of the obtained data. Hence, a mathematical expression could be found that relates the *n*-C_7 asphaltene expected catalytic oxidation temperature with the dosage of NiO and PdO over Si7. The optimized nanoparticle SiNi3.2Pd5.5 there was synthesized and characterized. Their behavior related to n-C7 asphaltene adsorption and DAO quality was like the other bimetallic nanoparticle observed, especially SiNi5Pd5. Related to the evaluated cycles, there was a slight change in adsorption behavior between the first and second cycles. From cycles 2 to 5, the results remain the same. A similar trend was observed for the catalytic oxidation test carried on depending on temperature.

According to the previous results, the isothermal catalytic decomposition tests were carried on at different temperatures. There was found that optimized nanoparticles allowed the complete

decomposition of *n*-C_7 asphaltenes at 190 °C and for the pitch at 340 °C. These results are remarkable, considering the decompositions for the samples without nanoparticles at 390 °C were 45.7 % and 56.7%, respectively. The evaluation of gaseous products also showed an increment for bimetallic functionalized nanoparticles compared to Si7 and those without nanoparticles. The most produced gas in all samples was CO_2.

5. Conclusions and recommendations

5.1. Conclusions

An enhanced solvent de-asphalting process (*e*-SDA) was proposed that shows the role of nanoparticles in obtaining DAO samples of better quality than those produced by the traditional process. Despite the solvent to oil ratio, type of solvent, temperature and nanoparticle dosage, the SiO2 nanoparticles proved to generate DAO with higher °API, lowest asphaltene content and expected viscosities than those observed for the SDA process. In this sense, other commercial nanoparticles of different chemical nature were tested, assessing their *n*-C_7 asphaltene adsorption properties and catalytic oxidation behavior. Si7 was selected as the nanomaterial with the best conditions to generate the DAO samples with the highest quality. There was a relationship between the q_m parameter of the SLE model, related to maximum adsorption capacity, and the DAO measures associated with their quality. In this scenario, a simplex-centroid mixture design was carried out to optimize the NiO and PdO load onto the Si7 surface, minimizing the oxidation decomposition temperature. There was found that SiNi3.2Pd5.5 reduces this temperature to 185 °C, considering the predicted statistical analysis of 185 °C. This material was evaluated for 5 cycles of regeneration, founding a minimal change in its adsorption isotherm of *n*-C_7 asphaltene after the first regeneration. From cycles 2 to 5, significant changes there weren't observed. These results were reflected in DAO quality that follows the same behavior. Finally, for the *e*-SDA pitch obtained with the optimized nanoparticles, its isothermal catalytic conversion was evaluated. It can be noticed that at 340 °C, there was achieved a total conversion of the pitch, while for the virgin pitch can be reached less than 60 % of conversion at 390 °C. The *e*-SDA process carried out with bimetallic nanoparticles also produced a higher proportion of gases than those observed for the Si7 nanoparticles and the traditional SDA process.

5.2. Recommendations

According to the obtained results, further recommendations are proposed:

- Carry on the crude oil elemental analysis and for the different obtained pitch and DAO samples to know the mass balance between the carbon, hydrogen, oxygen, nitrogen and sulfur content along the process.
- Including in the proposed simplex-centroid mixture design (SCMD) other operation variables like SOR, temperature, type of solvent, and nanoparticles dosage to better understand how they are related and their impact in expected DAO quality and pitch catalytic decomposition.
- Evaluate through isothermal decomposition all the obtained pitch from the *e*-SDA process carried out inside the SCMD.
- Characterize the optimized nanoparticles at the different regeneration cycles to follow any possible change using SEM, TEM, XPS, XRD, among others.

6. Publications and awards

6.1. Scientific papers

- Guzmán, J. D., Franco, C. A., & Cortés, F. B. (2017). An enhanced-solvent deasphalting process: effect of inclusion of SiO2 nanoparticles in the quality of deasphalted oil. *Journal of Nanomaterials*, *2017*.

6.2. Oral presentations and posters

- **III Workshop on adsorption, Catalysis and Porous Materials.** Universidad de lo Andes, Bogotá D.C. (August 2016). "A new process of enhanced-solvent deasphalting (*e*-SDA) based on nanotechnology" (poster).
- **XVII Congreso Colombiano de Petróleo y Gas 2017.** Acipet, G12 Convention Center, Bogotá D. C. (October 2017). "An Enhanced-Solvent De-Asphalting Process (e-SDA): Effect of Inclusion of Nanoparticles in the Quality of De-Asphalted Oil and in the Catalytic Conversion of Pitch" (oral presentation).
- **Escuela de Verano. New Technologies in productivity and enhanced recovery of oil and gas VII Edition.** Universidad Nacional de Colombia, Sede Medellín – Hotel Dann Carlton Medellín (May 2019). "DEVELOPMENT OF AN ENHANCED SOLVENT DE-ASPHALTING PROCESS BASED ON THE NANOTECHNOLOGY (E-SDA): IMPROVE OF THE QUALITY OF THE DEASPHALTED OIL (DAO) AND THE CATALYTIC CONVERSION OF THE PITCH" (oral presentation).
- **XVIII Congreso Colombiano de Petróleo y Gas.** Acipet, Centro de Convenciones, Bogotá D. C. (November 2019). "Desarrollo de un método de desasfaltado por solventes basado en nanotecnología (*e*-SDA): Mejoramiento de la calidad del crudo desasfaltado (DAO)" (poster).

6.3. Awards

- II Francisco Rodríguez Reinoso Award for the best poster in the III Workshop on Adsorption, Catalysis and Porous Materials 29-31. Universidad de los Andes, Bogotá D. C. August 2016.

Bibliography

[1] L. Capuano, "International energy outlook 2018 (IEO2018)," *US Energy Information Administration (EIA): Washington, DC, USA,* vol. 2018, p. 21, 2018.

[2] I. O. W. Outlook, "World Energy Outlook Series," *Paris, France: International Energy Agency,* 2018.

[3] A. Demirbas, A. Bafail, and A.-S. Nizami, "Heavy oil upgrading: Unlocking the future fuel supply," *Petroleum Science and Technology,* vol. 34, pp. 303-308, 2016.

[4] Z. LIU, H. WANG, G. Blackbourn, F. MA, Z. HE, Z. WEN*, et al.*, "Heavy oils and oil sands: global distribution and resource assessment," *Acta Geologica Sinica-English Edition,* vol. 93, pp. 199-212, 2019.

[5] UPME. (2012, 2016/02/22). *Escenarios de Oferta y Demanda de Hidrocarburos en Colombia*. Available: http://www.upme.gov.co/Docs/Publicaciones/2012/Escenarios_Oferta_Demanda_Hidrocarburos.pdf

[6] Campetrol. (2015, 2016/02/21). *Crudos pesados: el reto para Colombia*. Available: http://campetrol.org/crudos-pesados-el-reto-para-colombia/

[7] J. G. Speight, *Heavy and extra-heavy oil upgrading technologies*: Gulf Professional Publishing, 2013.

[8] J. G. Speight, *The chemistry and technology of petroleum*, Fourth ed.: CRC press, 2006.

[9] A.-Y. Huc, *Heavy crude oils: from geology to upgrading: an overview*: Editions Technip, 2010.

[10] A. Hinkle and M. Batzle, "Heavy oils: A worldwide overview," *The Leading Edge,* vol. 25, pp. 742-749, 2006.

[11] R. Martínez-Palou, M. de Lourdes Mosqueira, B. Zapata-Rendón, E. Mar-Juárez, C. Bernal-Huicochea, J. de la Cruz Clavel-López*, et al.*, "Transportation of heavy and extra-heavy crude oil by pipeline: A review," *Journal of Petroleum Science and Engineering,* vol. 75, pp. 274-282, 2011.

[12] M. Ghanavati, M.-J. Shojaei, and A. Ramazani, "Effects of asphaltene content and temperature on viscosity of Iranian heavy crude oil: experimental and modeling study," *Energy & Fuels,* vol. 27, pp. 7217-7232, 2013.

[13] K. Leontaritis, J. Amaefule, and R. Charles, "A systematic approach for the prevention and treatment of formation damage caused by asphaltene deposition," *SPE Production & Facilities,* vol. 9, pp. 157-164, 1994.

[14] E. Y. Sheu and O. C. Mullins, *Fundamentals and applications*: Springer, 1995.

[15] J. Woods, J. Kung, D. Kingston, L. Kotlyar, B. Sparks, and T. McCracken, "Canadian crudes: A comparative study of SARA fractions from a modified HPLC separation technique," *Oil & Gas Science and Technology-Revue de l'IFP,* vol. 63, pp. 151-163, 2008.

[16] K. Akbarzadeh, H. Alboudwarej, W. Y. Svrcek, and H. W. Yarranton, "A generalized regular solution model for asphaltene precipitation from n-alkane diluted heavy oils and bitumens," *Fluid Phase Equilibria,* vol. 232, pp. 159-170, 2005.

[17] P. Luo and Y. Gu, "Effects of asphaltene content on the heavy oil viscosity at different temperatures," *Fuel,* vol. 86, pp. 1069-1078, 2007.

[18] I. Hénaut, L. Barré, J. Argillier, F. Brucy, and R. Bouchard, "Rheological and structural properties of heavy crude oils in relation with their asphaltenes content," in *SPE International Symposium on Oilfield Chemistry*, 2001.

[19] A. H. Kamran Akbarzadeh, Abdel Kharrat, Dan Zhang, Stephan Allenson, Jefferson Creek, Shah Kabir, A. Jamaluddin, Alan G. Marshall, Ryan Rodgers, Oliver C. Mullins, Trond Solbakken, "Asphaltenes—Problematic but Rich in Potential," *Oil Field Review,* pp. 22-43, 2007.

[20] R. R. Chianelli, M. Siadati, A. Mehta, J. Pople, L. C. Ortega, and L. Y. Chiang, "Self-assembly of asphaltene aggregates: synchrotron, simulation and chemical modeling techniques applied to problems in the structure and reactivity of asphaltenes," in *Asphaltenes, Heavy Oils, and Petroleomics*, ed: Springer, 2007, pp. 375-400.

[21] E. A. Taborda, V. Alvarado, C. A. Franco, and F. B. Cortés, "Rheological demonstration of alteration in the heavy crude oil fluid structure upon addition of nanoparticles," *Fuel,* vol. 189, pp. 322-333, 2017.

[22] E. A. Taborda, C. A. Franco, S. H. Lopera, V. Alvarado, and F. B. Cortes, "Effect of nanoparticles/nanofluids on the rheology of heavy crude oil and its mobility on porous media at reservoir conditions," *Fuel,* vol. 184, pp. 222-232, 2016.

[23] W. Chuan, L. Guang-Lun, C.-j. YAO, K.-j. SUN, P.-y. Gai, and Y.-b. CAO, "Mechanism for reducing the viscosity of extra-heavy oil by aquathermolysis with an amphiphilic catalyst," *Journal of Fuel Chemistry and Technology,* vol. 38, pp. 684-690, 2010.

[24] S. Chavan, H. Kini, and R. Ghosal, "Process for sulfur reduction from high viscosity petroleum oils," *International Journal of Environmental Science and Development,* vol. 3, p. 228, 2012.

[25] R. Moore, C. Laureshen, S. Mehta, M. Ursenbach, J. Belgrave, J. Weissman*, et al.*, "A downhole catalytic upgrading process for heavy oil using in situ combustion," *Journal of Canadian Petroleum Technology,* vol. 38, 1999.

[26] I. Gates, N. Chakrabarty, R. Moore, S. Mehta, E. Zalewski, and P. Pereira, "In situ upgrading of Llancanelo heavy oil using in situ combustion and a downhole catalyst bed," *Journal of Canadian Petroleum Technology,* vol. 47, 2008.

[27] W. R. Shu, "In-situ combustion method for recovery of heavy oil utilizing oxygen and carbon dioxide as initial oxidant," ed: Google Patents, 1983.

[28] R. Hashemi, N. N. Nassar, and P. P. Almao, "Nanoparticle technology for heavy oil in-situ upgrading and recovery enhancement: Opportunities and challenges," *Applied Energy,* vol. 133, pp. 374-387, 2014.

[29] K. Guo, H. Li, and Z. Yu, "Metallic Nanoparticles for Enhanced Heavy Oil Recovery: Promises and Challenges," *Energy Procedia,* vol. 75, pp. 2068-2073, 2015.

[30] C. A. Franco, T. Montoya, N. N. Nassar, P. Pereira-Almao, and F. B. Cortés, "Adsorption and Subsequent Oxidation of Colombian Asphaltenes onto Nickel and/or Palladium Oxide Supported on Fumed Silica Nanoparticles," *Energy & Fuels,* vol. 27, pp. 7336-7347, 2013.

[31] C. Franco, L. Cardona, S. Lopera, J. Mejía, and F. Cortés, "Heavy oil upgrading and enhanced recovery in a continuous steam injection process assisted by nanoparticulated catalysts," in *SPE improved oil recovery conference*, 2016.

[32] G. Wichert, N. Okazawa, R. Moore, and J. Belgrave, "In-situ upgrading of heavy oils by low-temperature oxidation in the presence of caustic additives," in *SPE International Heavy Oil Symposium*, 1995.

[33] L. Wei, J.-H. Zhu, and J.-H. Qi, "Application of nano-nickel catalyst in the viscosity reduction of Liaohe extra-heavy oil by aqua-thermolysis," *Journal of Fuel Chemistry and Technology,* vol. 35, pp. 176-180, 2007.

[34] P. Clark and J. Hyne, "Steam-oil chemical reactions: mechanisms for the aquathermolysis of heavy oils," *Aostra J Res,* vol. 1, pp. 15-20, 1984.

[35] A. Ambalae, N. Mahinpey, and N. Freitag, "Thermogravimetric studies on pyrolysis and combustion behavior of a heavy oil and its asphaltenes," *Energy & fuels,* vol. 20, pp. 560-565, 2006.
[36] H. N. Woebcke, S. Narayanan, and A. R. Johnson, "Integrated heavy oil pyrolysis process," ed: Google Patents, 1986.
[37] A. Davletbaev, L. Kovaleva, and T. Babadagli, "Heavy oil production by electromagnetic heating in hydraulically fractured wells," *Energy & Fuels,* vol. 28, pp. 5737-5744, 2014.
[38] O. A. Alomair and A. S. Almusallam, "Heavy crude oil viscosity reduction and the impact of asphaltene precipitation," *Energy & Fuels,* vol. 27, pp. 7267-7276, 2013.
[39] J. L. García Zapata and A. de Klerk, "Viscosity changes during mild oxidation of oilsands-derived bitumen: Solvent effects and selectivity," *Energy & Fuels,* vol. 28, pp. 6242-6248, 2014.
[40] D. Nguyen and V. Balsamo, "Emulsification of heavy oil in aqueous solutions of poly (vinyl alcohol): A method for reducing apparent viscosity of production fluids," *Energy & Fuels,* vol. 27, pp. 1736-1747, 2013.
[41] I. Md. Saaid, S. Q. A. Mahat, B. Lal, M. I. A. Mutalib, and K. M. Sabil, "Experimental Investigation on the Effectiveness of 1-Butyl-3-methylimidazolium Perchlorate Ionic Liquid as a Reducing Agent for Heavy Oil Upgrading," *Industrial & Engineering Chemistry Research,* vol. 53, pp. 8279-8284, 2014.
[42] K. Sharma, V. Saxena, A. Kumar, H. Ghildiyal, A. Anuradha, N. Sharma*, et al.*, "Pipeline Transportation of Heavy/Viscous Crude Oil as Water Continuous Emulsion in," *SPE India Oil and Gas Conference and Exhibition,* 1998.
[43] H. L. Alfonso and Y. D. Drubey, "Propiedades reológicas de emulsiones de petróleo pesado en agua."
[44] J. Colyar, "Has the time for partial upgrading of heavy oil and bitumen arrived?," *Petroleum technology quarterly,* vol. 14, 2009.
[45] M. Motaghi, P. Saxena, and R. Ravi, "Partial upgrading of heavy oil reserves," *Petroleum technology quarterly,* vol. 15, 2010.
[46] R. Luhning, A. Anand, T. Blackmore, and D. Lawson, "Pipeline Transportation of Emerging Partially Upgraded Bitumen," *Canadian International Petroleum Conference,* 2002.
[47] R. Oliemans, G. Ooms, H. Wu, and A. Duijvestijn, "Core-annular oil/water flow: the turbulent-lubricating-film model and measurements in a 5 cm pipe loop," *International journal of multiphase flow,* vol. 13, pp. 23-31, 1987.
[48] P. Poesio and D. Strazza, "Experiments on Start-Up of an Oil-Water Core Annular Flow Through a Horizontal or Nearly Horizontal Pipe," *13th International Conference on Multiphase Production Technology,* 2007.
[49] S. Ghosh, T. Mandal, G. Das, and P. Das, "Review of oil water core annular flow," *Renewable and Sustainable Energy Reviews,* vol. 13, pp. 1957-1965, 2009.
[50] E. Bobok, D. Magyari, and G. Udvardi, "Heavy oil transport through lubricated pipeline," *European Petroleum Conference,* 1996.
[51] R. Tao and X. Xu, "Reducing the viscosity of crude oil by pulsed electric or magnetic field," *Energy & fuels,* vol. 20, pp. 2046-2051, 2006.
[52] J. J. Taber, F. D. Martin, and R. Seright, "EOR screening criteria revisited," in *Symposium on improved oil recovery*, 1996, pp. 387-415.
[53] J. Taber, F. Martin, and R. Seright, "EOR screening criteria revisited—part 2: applications and impact of oil prices," *SPE Reservoir Engineering,* vol. 12, pp. 199-206, 1997.

[54] J. J. Taber, F. Martin, and R. Seright, "EOR screening criteria revisited-Part 1: Introduction to screening criteria and enhanced recovery field projects," *SPE Reservoir Engineering,* vol. 12, pp. 189-198, 1997.
[55] T. Nasr, G. Beaulieu, H. Golbeck, and G. Heck, "Novel Expanding Solvent-SAGD Process" ES-SAGD"," *Journal of Canadian Petroleum Technology,* vol. 42, 2003.
[56] R. Butler, "SAGD comes of age!," *Journal of Canadian Petroleum Technology,* vol. 37, 1998.
[57] K. Kisman and K. Yeung, "Numerical study of the SAGD process in the Burnt Lake oil sands lease," in *SPE international heavy oil symposium*, 1995.
[58] S. Larter, J. Adams, I. Gates, B. Bennett, and H. Huang, "The origin, prediction and impact of oil viscosity heterogeneity on the production characteristics of tar sand and heavy oil reservoirs," *Journal of Canadian Petroleum Technology,* vol. 47, 2008.
[59] S. Thomas, "Enhanced oil recovery-an overview," *Oil & Gas Science and Technology-Revue de l'IFP,* vol. 63, pp. 9-19, 2008.
[60] T. Babadagli, "Evaluation of EOR methods for heavy-oil recovery in naturally fractured reservoirs," *Journal of Petroleum Science and Engineering,* vol. 37, pp. 25-37, 2003.
[61] M. S. Picha, "Enhanced oil recovery by hot CO2 flooding," in *SPE Middle East Oil and Gas Show and Conference*, 2007.
[62] M. Islam, B. Erno, and D. Davis, "Hot gas and waterflood equivalence of in situ combustion," *Journal of Canadian Petroleum Technology,* vol. 31, 1992.
[63] P. L. McGuire, R. Okuno, T. L. Gould, and L. W. Lake, "Ethane-Based EOR: An Innovative and Profitable EOR Opportunity for a Low Price Environment," in *SPE Improved Oil Recovery Conference*, 2016.
[64] S. Ghedan, "Global laboratory experience of CO2-EOR flooding," in *SPE/EAGE Reservoir Characterization & Simulation Conference*, 2009.
[65] F. Gozalpour, S. Ren, and B. Tohidi, "CO2 EOR and storage in oil reservoir," *Oil & gas science and technology,* vol. 60, pp. 537-546, 2005.
[66] G. Oskui, P. Reza, M. A. Jumaa, E. G. Folad, A. Rashed, and S. Patil, "Systematic Approach for Prevention and Remediation of Asphaltene Problems During CO2/Hydrocarbon Injection Project," in *The Twenty-first International Offshore and Polar Engineering Conference*, 2011.
[67] S. Gharfeh, A. Yen, S. Asomaning, and D. Blumer, "Asphaltene flocculation onset determinations for heavy crude oil and its implications," *Petroleum science and technology,* vol. 22, pp. 1055-1072, 2004.
[68] R. S. Al-Maamari and J. S. Buckley, "Asphaltene precipitation and alteration of wetting: the potential for wettability changes during oil production," *SPE Reservoir Evaluation & Engineering,* vol. 6, pp. 210-214, 2003.
[69] J. M. Lee, S. Shin, S. Ahn, J. H. Chun, K. B. Lee, S. Mun*, et al.*, "Separation of solvent and deasphalted oil for solvent deasphalting process," *Fuel Processing Technology,* vol. 119, pp. 204-210, 2014.
[70] J. D. Guzmán, C. A. Franco, and F. B. Cortés, "An enhanced-solvent deasphalting process: effect of inclusion of SiO2 nanoparticles in the quality of deasphalted oil," *Journal of Nanomaterials,* vol. 2017, 2017.
[71] G. Brons and J. M. Yu, "Solvent deasphalting effects on whole cold lake bitumen," *Energy & fuels,* vol. 9, pp. 641-647, 1995.
[72] E. Buenrostro-Gonzalez, C. Lira-Galeana, A. Gil-Villegas, and J. Wu, "Asphaltene precipitation in crude oils: Theory and experiments," *AIChE Journal,* vol. 50, pp. 2552-2570, 2004.

[73] D. Hartmann, H. E. Lopes, C. Teixeira, M. C. K. de Oliveira, G. Gonzalez, E. F. Lucas*, et al.*, "Alkanes Induced Asphaltene Precipitation Studies at High Pressure and Temperature in the Presence of Argon," *Energy & Fuels,* 2016.

[74] S. L. Kokal, J. Najman, S. G. Sayegh, and A. E. George, "Measurement and correlation of asphaltene precipitation from heavy oils by gas injection," *Journal of Canadian Petroleum Technology,* vol. 31, 1992.

[75] S. H. Ng, "Nonconventional residuum upgrading by solvent deasphalting and fluid catalytic cracking," *Energy & fuels,* vol. 11, pp. 1127-1136, 1997.

[76] L. M. Arciniegas and T. Babadagli, "Quantitative and visual characterization of asphaltenic components of heavy-oil after solvent interaction at different temperatures and pressures," *Fluid Phase Equilibria,* vol. 366, pp. 74-87, 2014.

[77] P. Luo, X. Wang, and Y. Gu, "Characterization of asphaltenes precipitated with three light alkanes under different experimental conditions," *Fluid Phase Equilibria,* vol. 291, pp. 103-110, 2010.

[78] S. Ng, "DEASPHALTING OF NON-CONVENTIONAL RESIDUES."

[79] F. Samedova, A. Kasumova, S. Y. Rashidova, and V. Alieva, "A new method for isolation of asphaltenes from petroleum and its heavy residues," *Petroleum Chemistry,* vol. 47, pp. 399-401, 2007.

[80] L. Lodi, V. C. Concha, R. Souza, L. Medina, R. Filho, and M. W. Maciel, "An Experimental Study of a Pilot Plant Deasphalting Process in Subcritical and Supercritical Conditions," *Petroleum Science and Technology,* vol. 32, pp. 2659-2665, 2014.

[81] L. Lodi, V. O. Cárdenas Concha, L. C. Medina, R. Maciel Filho, and M. R. Wolf Maciel, "An Experimental Study of a Pilot Plant Deasphalting Process in CO2 Supercritical," *Petroleum Science and Technology,* vol. 33, pp. 481-486, 2015.

[82] Z. Liu, G. Yang, Y. Lu, B. Han, and H. Yan, "Phase equilibria of the CO 2–Jiangsu crude oil system and precipitation of heavy components induced by supercritical CO 2," *The Journal of supercritical fluids,* vol. 16, pp. 27-31, 1999.

[83] H. Edward J. and M. Michael J., "When solvent deasphalting is the most appropriate technology for upgrading residue," presented at the IDTC Conference, London, England, 2006.

[84] F. Cao, D. Jiang, W. Li, P. a. Du, G. Yang, and W. Ying, "Process analysis of the extract unit of vacuum residue through mixed C4 solvent for deasphalting," *Chemical Engineering and Processing: Process Intensification,* vol. 49, pp. 91-96, 2010.

[85] A. Hirschberg, L. DeJong, B. Schipper, and J. Meijer, "Influence of temperature and pressure on asphaltene flocculation," *Society of Petroleum Engineers Journal,* vol. 24, pp. 283-293, 1984.

[86] F. Chung, P. Sarathi, and R. Jones, "Modeling of asphaltene and wax precipitation," National Inst. for Petroleum and Energy Research, Bartlesville, OK (USA)1991.

[87] H. Rassamdana, B. Dabir, M. Nematy, M. Farhani, and M. Sahimi, "Asphalt flocculation and deposition: I. The onset of precipitation," *AIChE Journal,* vol. 42, pp. 10-22, 1996.

[88] D. L. Mitchell and J. G. Speight, "The solubility of asphaltenes in hydrocarbon solvents," *Fuel,* vol. 52, pp. 149-152, 1973.

[89] J. Long, B.-X. Shen, H. Ling, J.-G. Zhao, and J.-C. Lu, "Improving the Solvent Deasphalting Process by the Co-treating of Residue and Coal," *Energy Sources, Part A: Recovery, Utilization, and Environmental Effects,* vol. 35, pp. 1956-1963, 2013.

[90] J. Long, B. Shen, H. Ling, J. Zhao, and J. Lu, "Novel solvent deasphalting process by vacuum residue blending with coal tar," *Industrial & Engineering Chemistry Research,* vol. 50, pp. 11259-11269, 2011.

[91] M. Ikematsu, I. Honzyo, and K. Sakai, "Process for the solvent deasphalting of asphaltene-containing hydrocarbons," ed: Google Patents, 1985.
[92] O. R. Koseoglu, "Enhanced solvent deasphalting process for heavy hydrocarbon feedstocks utilizing solid adsorbent," ed: Google Patents, 2009.
[93] O. R. Koseoglu, "Process for upgrading hydrocarbon feedstocks using solid adsorbent and membrane separation of treated product stream," ed: Google Patents, 2012.
[94] OPEC, *2015 World Oil Outlook*. Vienna, Austria: OPEC Secretariat, 2015.
[95] H. Alboudwarej, J. J. Felix, S. Taylor, R. Badry, C. Bremner, B. Brough*, et al.*, "La importancia del petróleo pesado," *Oilfield review,* vol. 18, pp. 38-59, 2006.
[96] IEA, *World energy outlook 2012*. Paris, France: International Energy Agency, 2012.
[97] J. G. Speight, *The desulfurization of heavy oils and residua*: CRC Press, 1999.
[98] S. Acevedo, A. Castro, J. G. Negrin, A. Fernández, G. Escobar, V. Piscitelli*, et al.*, "Relations between asphaltene structures and their physical and chemical properties: The rosary-type structure," *Energy & fuels,* vol. 21, pp. 2165-2175, 2007.
[99] H. Groenzin and O. C. Mullins, "Asphaltene molecular size and structure," *The Journal of Physical Chemistry A,* vol. 103, pp. 11237-11245, 1999.
[100] O. C. Mullins, "The asphaltenes," *Annual Review of Analytical Chemistry,* vol. 4, pp. 393-418, 2011.
[101] O. C. Mullins, H. Sabbah, J. l. Eyssautier, A. E. Pomerantz, L. Barré, A. B. Andrews*, et al.*, "Advances in asphaltene science and the Yen–Mullins model," *Energy & Fuels,* vol. 26, pp. 3986-4003, 2012.
[102] W. H. Richard, "Process of distilling petroleum oil," ed: Google Patents, 1928.
[103] R. R. Rosenbaum, "Process for separating hydrocarbons," ed: Google Patents, 1918.
[104] C. S. Hsu and P. Robinson, *Practical advances in petroleum processing* vol. 1: Springer Science & Business Media, 2007.
[105] G. Gester Jr, "Solvent Extraction in the Petroleum Industry," ed: ACS Publications, 1951.
[106] G. H. Weber, "Modern Petroleum Processes," in *3rd World Petroleum Congress*, 1951.
[107] E. W. Funk, "Behavior of tar sand bitumen with paraffinic solvents and its application to separations for Athabasca tar sands," *The Canadian Journal of Chemical Engineering,* vol. 57, pp. 333-341, 1979.
[108] L. S. Moreno and T. Babadagli, "Quantitative and visual characterization of asphaltenic components of heavy-oil and bitumen samples after solvent interaction at different temperatures and pressures," in *SPE International Symposium on Oilfield Chemistry*, 2013.
[109] P. Luo and Y. Gu, "Characterization of a heavy oil–propane system in the presence or absence of asphaltene precipitation," *Fluid Phase Equilibria,* vol. 277, pp. 1-8, 2009.
[110] N. N. Nassar, A. Hassan, L. Carbognani, F. Lopez-Linares, and P. Pereira-Almao, "Iron oxide nanoparticles for rapid adsorption and enhanced catalytic oxidation of thermally cracked asphaltenes," *Fuel,* vol. 95, pp. 257–262, 2012.
[111] N. N. Nassar, A. Hassan, and P. Pereira-Almao, "Comparative oxidation of adsorbed asphaltenes onto transition metal oxide nanoparticles," *Colloids and Surfaces A: Physicochemical and Engineering Aspects,* vol. 384, pp. 145-149, 2011.
[112] N. N. Nassar, A. Hassan, and P. Pereira-Almao, "Metal Oxide Nanoparticles for Asphaltene Adsorption and Oxidation," *Energy & Fuels,* vol. 25, pp. 1017-1023, 2011.
[113] N. N. Nassar, "Asphaltene adsorption onto alumina nanoparticles: kinetics and thermodynamic studies," *Energy & Fuels,* vol. 24, pp. 4116-4122, 2010.
[114] F. B. Cortés, J. M. Mejía, M. A. Ruiz, P. Benjumea, and D. B. Riffel, "Sorption of asphaltenes onto nanoparticles of nickel oxide supported on nanoparticulated silica gel," *Energy & Fuels,* vol. 26, pp. 1725-1730, 2012.

[115] C. A. Franco, N. N. Nassar, M. A. Ruiz, P. Pereira-Almao, and F. B. Cortés, "Nanoparticles for inhibition of asphaltenes damage: adsorption study and displacement test on porous media," *Energy & Fuels,* vol. 27, pp. 2899-2907, 2013.
[116] N. N. Nassar, A. Hassan, and G. Vitale, "Comparing kinetics and mechanism of adsorption and thermo-oxidative decomposition of Athabasca asphaltenes onto TiO 2, ZrO 2, and CeO 2 nanoparticles," *Applied Catalysis A: General,* vol. 484, pp. 161-171, 2014.
[117] C. A. Franco, M. M. Lozano, S. Acevedo, N. N. Nassar, and F. B. Cortés, "Effects of Resin I on Asphaltene Adsorption onto Nanoparticles: A Novel Method for Obtaining Asphaltenes/Resin Isotherms," *Energy & Fuels,* vol. 30, pp. 264-272, 2015.
[118] ASTM, "D7220-12 Standard Test Method for Sulfur in Automotive, Heating, and Jet Fuels by Monochromatic Energy Dispersive X-ray Fluorescence Spectrometry," ed, 2012.
[119] ASTM, "D1298-12b Standard Test Method for Density, Relative Density, or API Gravity of Crude Petroleum and Liquid Petroleum Products by Hydrometer Method," ed, 2012.
[120] ASTM, "D7169-11 Standard Test Method for Boiling Point Distribution of Samples with Residues Such as Crude Oils and Atmospheric and Vacuum Residues by High Temperature Gas Chromatography," ed, 2011.
[121] H. A. Barnes, J. F. Hutton, and K. Walters, *An introduction to rheology* vol. 3: Elsevier, 1989.
[122] M. A. Rao, "Flow and functional models for rheological properties of fluid foods," in *Rheology of Fluid, Semisolid, and Solid Foods*, ed: Springer, 2014, pp. 27-61.
[123] D. C. Montgomery and G. C. Runger, *Applied statistics and probability for engineers*: John Wiley & Sons, 2010.
[124] J. Murgich, J. Rodríguez, and Y. Aray, "Molecular recognition and molecular mechanics of micelles of some model asphaltenes and resins," *Energy & Fuels,* vol. 10, pp. 68-76, 1996.
[125] S. I. Andersen and J. G. Speight, "Petroleum resins: separation, character, and role in petroleum," *Petroleum science and technology,* vol. 19, pp. 1-34, 2001.
[126] J. Speight, "Petroleum Asphaltenes-Part 1: Asphaltenes, resins and the structure of petroleum," *Oil & gas science and technology,* vol. 59, pp. 467-477, 2004.
[127] J. J. Adams, "Asphaltene adsorption, a literature review," *Energy & Fuels,* vol. 28, pp. 2831-2856, 2014.
[128] N. N. Nassar, T. Tatiana Montoya, C. A. Franco, F. B. Cortés, and P. R. Pereira-Almao, "A New Model for Describing the Adsorption of Asphaltenes on Porous Media at a High Pressure and Temperature under Flow Conditions," *Energy & Fuels,* 2015.
[129] S. Betancur, J. C. Carmona, N. N. Nassar, C. A. Franco, and F. B. Cortés, "Role of Particle Size and Surface Acidity of Silica Gel Nanoparticles in Inhibition of Formation Damage by Asphaltene in Oil Reservoirs," *Industrial & Engineering Chemistry Research,* 2016.
[130] C. A. Franco, N. N. Nassar, T. Montoya, M. A. Ruíz, and F. B. Cortés, "Influence of asphaltene aggregation on the adsorption and catalytic behavior of nanoparticles," *Energy & Fuels,* vol. 29, pp. 1610-1621, 2015.
[131] R. Zabala, C. Franco, and F. Cortés, "Application of Nanofluids for Improving Oil Mobility in Heavy Oil and Extra-Heavy Oil: A Field Test," in *SPE Improved Oil Recovery Conference*, 2016.
[132] S.-Y. Yang, G. Hirasaki, S. Basu, and R. Vaidya, "Statistical analysis on parameters that affect wetting for the crude oil/brine/mica system," *Journal of Petroleum Science and Engineering,* vol. 33, pp. 203-215, 2002.
[133] T. Montoya, D. Coral, C. A. Franco, N. N. Nassar, and F. B. Cortés, "A Novel Solid–Liquid Equilibrium Model for Describing the Adsorption of Associating Asphaltene Molecules onto Solid Surfaces Based on the “Chemical Theory”," *Energy & Fuels,* vol. 28, pp. 4963-4975, 2014.

[134] N. N. Nassar, T. Montoya, C. A. Franco, F. B. Cortés, and P. Pereira-Almao, "A new model for describing the adsorption of asphaltenes on porous media at a high pressure and temperature under flow conditions," *Energy & Fuels,* vol. 29, pp. 4210-4221, 2015.
[135] N. N. Nassar, S. Betancur, S. c. Acevedo, C. A. Franco, and F. B. Cortés, "Development of a Population Balance Model to Describe the Influence of Shear and Nanoparticles on the Aggregation and Fragmentation of Asphaltene Aggregates," *Industrial & Engineering Chemistry Research,* vol. 54, pp. 8201-8211, 2015.
[136] T. Montoya, B. L. Argel, N. N. Nassar, C. A. Franco, and F. B. Cortés, "Kinetics and mechanisms of the catalytic thermal cracking of asphaltenes adsorbed on supported nanoparticles," *Petroleum Science,* pp. 1-11, 2016.
[137] J. D. Guzmán, S. Betancur, F. Carrasco-Marín, C. A. Franco, N. N. Nassar, and F. B. Cortés, "Importance of the Adsorption Method Used for Obtaining the Nanoparticle Dosage for Asphaltene-Related Treatments," *Energy & Fuels,* vol. 30, pp. 2052-2059, 2016.
[138] C. A. Franco, T. Montoya, N. N. Nassar, and F. B. Cortés, "Nioand pdo supported on fumed silica nanoparticles for adsorption and catalytic steam gasification of colombian c7asphaltenes," *Handbook on Oil Production Research; Nova Science Publishers: Hauppauge, NY, USA,* pp. 101-145, 2014.
[139] C. Franco and C. Franco, "Synthesis and application of supported metallic and multi-metallic oxides nanoparticles for in-situ upgrading and inhibition of formation damage," *Universidad Nacional de Colombia-Sede Medellín: Medellín, Antioquia, Colombia,* 2015.
[140] N. N. Nassar, C. A. Franco, T. Montoya, F. B. Cortés, and A. Hassan, "Effect of oxide support on Ni–Pd bimetallic nanocatalysts for steam gasification of n-C7 asphaltenes," *Fuel,* vol. 156, pp. 110-120, 2015.
[141] T. Montoya, B. L. Argel, N. N. Nassar, C. A. Franco, and F. B. Cortés, "Kinetics and mechanisms of the catalytic thermal cracking of asphaltenes adsorbed on supported nanoparticles," *Petroleum Science,* vol. 13, pp. 561-571, 2016.
[142] C. A. Franco-Ariza, J. D. Guzmán-Calle, and F. B. Cortés-Correa, "Adsorption and catalytic oxidation of asphaltenes in fumed silica nanoparticles: Effect of the surface acidity," *Dyna,* vol. 83, pp. 171-179, 2016.
[143] J. D. Guzmán, S. Betancur, F. Carrasco-Marín, C. A. Franco, N. N. Nassar, and F. B. Cortés, "Importance of the adsorption method used for obtaining the nanoparticle dosage for asphaltene-related treatments," *Energy & Fuels,* vol. 30, pp. 2052-2059, 2016.
[144] S. Betancur, J. C. Carmona, N. N. Nassar, C. A. Franco, and F. B. Cortés, "Role of particle size and surface acidity of silica gel nanoparticles in inhibition of formation damage by asphaltene in oil reservoirs," *Industrial & Engineering Chemistry Research,* vol. 55, pp. 6122-6132, 2016.
[145] F. B. Cortés, T. Montoya, S. Acevedo, N. N. Nassar, and C. A. Franco, "Adsorption-desorption of nc 7 asphaltenes over micro-and nanoparticles of silica and its impact on wettability alteration," *CT&F-Ciencia, Tecnología y Futuro,* vol. 6, pp. 89-106, 2016.
[146] M. Madhi, A. Bemani, A. Daryasafar, and M. R. Khosravi Nikou, "Experimental and modeling studies of the effects of different nanoparticles on asphaltene adsorption," *Petroleum Science and Technology,* vol. 35, pp. 242-248, 2017.
[147] V. Vargas, J. Castillo, R. Ocampo-Torres, C.-P. Lienemann, and B. Bouyssiere, "Surface modification of SiO2 nanoparticles to increase asphaltene adsorption," *Petroleum Science and Technology,* vol. 36, pp. 618-624, 2018.
[148] C. Franco, E. Patiño, P. Benjumea, M. A. Ruiz, and F. B. Cortés, "Kinetic and thermodynamic equilibrium of asphaltenes sorption onto nanoparticles of nickel oxide supported on nanoparticulated alumina," *Fuel,* vol. 105, pp. 408-414, 2013.

[149] N. N. Nassar, A. Hassan, and P. Pereira-Almao, "Effect of surface acidity and basicity of aluminas on asphaltene adsorption and oxidation," *Journal of colloid and interface science,* vol. 360, pp. 233-238, 2011.
[150] N. N. Nassar, A. Hassan, and P. Pereira-Almao, "Effect of the particle size on asphaltene adsorption and catalytic oxidation onto alumina particles," *Energy & Fuels,* vol. 25, pp. 3961-3965, 2011.
[151] N. N. Nassar, A. Hassan, and G. Vitale, "Comparing kinetics and mechanism of adsorption and thermo-oxidative decomposition of Athabasca asphaltenes onto TiO2, ZrO2, and CeO2 nanoparticles," *Applied Catalysis A: General,* vol. 484, pp. 161-171, 2014.
[152] O. E. Medina, J. Gallego, D. Arias-Madrid, F. B. Cortés, and C. A. Franco, "Optimization of the load of transition metal oxides (Fe2O3, Co3O4, NiO and/or PdO) onto CeO2 nanoparticles in catalytic steam decomposition of n-C7 asphaltenes at low temperatures," *Nanomaterials,* vol. 9, p. 401, 2019.
[153] O. E. Medina, J. Gallego, L. G. Restrepo, F. B. Cortés, and C. A. Franco, "Influence of the Ce4+/Ce3+ Redox-couple on the cyclic regeneration for adsorptive and catalytic performance of NiO-PdO/CeO2±δ nanoparticles for n-C7 asphaltene steam gasification," *Nanomaterials,* vol. 9, p. 734, 2019.
[154] T. Montoya, D. Coral, C. A. Franco, N. N. Nassar, and F. B. Cortés, "A novel solid–liquid equilibrium model for describing the adsorption of associating asphaltene molecules onto solid surfaces based on the “chemical theory”," *Energy & Fuels,* vol. 28, pp. 4963-4975, 2014.
[155] W. Pang, J.-K. Lee, S.-H. Yoon, I. Mochida, T. Ida, and M. Ushio, "Compositional analysis of deasphalted oils from Arabian crude and their hydrocracked products," *Fuel Processing Technology,* vol. 91, pp. 1517-1524, 2010.
[156] N. N. Nassar, A. Hassan, and P. Pereira-Almao, "Application of nanotechnology for heavy oil upgrading: Catalytic steam gasification/cracking of asphaltenes," *Energy & Fuels,* vol. 25, pp. 1566-1570, 2011.
[157] M. M. Lozano, C. A. Franco, S. A. Acevedo, N. N. Nassar, and F. B. Cortés, "Effects of resin I on the catalytic oxidation of n-C 7 asphaltenes in the presence of silica-based nanoparticles," *RSC advances,* vol. 6, pp. 74630-74642, 2016.
[158] B. J. Berne and R. Pecora, *Dynamic light scattering: with applications to chemistry, biology, and physics*: Courier Corporation, 2000.
[159] J. Stetefeld, S. A. McKenna, and T. R. Patel, "Dynamic light scattering: a practical guide and applications in biomedical sciences," *Biophysical reviews,* vol. 8, pp. 409-427, 2016.
[160] J. Rouquerol, F. Rouquerol, P. Llewellyn, G. Maurin, and K. S. Sing, *Adsorption by powders and porous solids: principles, methodology and applications*: Academic press, 2013.
[161] S. Brunauer, P. H. Emmett, and E. Teller, "Adsorption of gases in multimolecular layers," *Journal of the American chemical society,* vol. 60, pp. 309-319, 1938.
[162] E. IP 469, "Determination of saturated, aromatic and polar compounds in petroleum products by thin layer chromatography and flame ionization detection," ed: Energy Institute London, 2001.
[163] O. Talu and F. Meunier, "Adsorption of associating molecules in micropores and application to water on carbon," *AIChE journal,* vol. 42, pp. 809-819, 1996.
[164] N. N. Nassar, S. Betancur, S. c. Acevedo, C. A. Franco, and F. B. Cortés, "Development of a population balance model to describe the influence of shear and nanoparticles on the aggregation and fragmentation of asphaltene aggregates," *Industrial & Engineering Chemistry Research,* vol. 54, pp. 8201-8211, 2015.
[165] D. C. Montgomery, *Design and analysis of experiments*: John wiley & sons, 2017.

[166] T. Ozawa, "A new method of analyzing thermogravimetric data," *Bulletin of the chemical society of Japan,* vol. 38, pp. 1881-1886, 1965.
[167] J. H. Flynn and L. A. Wall, "A quick, direct method for the determination of activation energy from thermogravimetric data," *Journal of Polymer Science Part B: Polymer Letters,* vol. 4, pp. 323-328, 1966.
[168] C. Doyle, "Synthesis and evaluation of thermally stable polymers. II," *Polymer evaluation. Appl Polym Sci,* vol. 5, pp. 285-292, 1961.
[169] N. N. Nassar, A. Hassan, G. Luna, and P. Pereira-Almao, "Comparative study on thermal cracking of Athabasca bitumen," *Journal of thermal analysis and calorimetry,* vol. 114, pp. 465-472, 2013.
[170] J. A. Koots and J. G. Speight, "Relation of petroleum resins to asphaltenes," *Fuel,* vol. 54, pp. 179-184, 1975.
[171] S. Akmaz, O. Iscan, M. Gurkaynak, and M. Yasar, "The structural characterization of saturate, aromatic, resin, and asphaltene fractions of Batiraman crude oil," *Petroleum Science and Technology,* vol. 29, pp. 160-171, 2011.
[172] M. Thommes, K. Kaneko, A. V. Neimark, J. P. Olivier, F. Rodriguez-Reinoso, J. Rouquerol*, et al.*, "Physisorption of gases, with special reference to the evaluation of surface area and pore size distribution (IUPAC Technical Report)," *Pure and Applied Chemistry,* vol. 87, pp. 1051-1069, 2015.
[173] D. Stratiev, I. Shishkova, T. Tsaneva, M. Mitkova, and D. Yordanov, "Investigation of relations between properties of vacuum residual oils from different origin, and of their deasphalted and asphaltene fractions," *Fuel,* vol. 170, pp. 115-129, 2016.
[174] M. Shojaei, M. Ghanavati, and A. R. SA, "Effects of Asphaltene content and Temperature on Viscosity of Iranian Heavy Crude Oil: Experimental Study," 2014.
[175] O. E. Medina, C. Olmos, S. H. Lopera, F. B. Cortés, and C. A. Franco, "Nanotechnology Applied to Thermal Enhanced Oil Recovery Processes: A Review," *Energies,* vol. 12, p. 4671, 2019.
[176] E. Byambajav and Y. Ohtsuka, "Hydrocracking of asphaltene with metal catalysts supported on SBA-15," *Applied Catalysis A: General,* vol. 252, pp. 193-204, 2003.
[177] H. Purón, J. L. Pinilla, J. Montoya de la Fuente, and M. Millán, "Effect of metal loading in NiMo/Al2O3 catalysts on Maya vacuum residue hydrocracking," *Energy & Fuels,* vol. 31, pp. 4843-4850, 2017.
[178] G. Cui, J. Wang, H. Fan, X. Sun, Y. Jiang, S. Wang*, et al.*, "Towards understanding the microstructures and hydrocracking performance of sulfided Ni–W catalysts: Effect of metal loading," *Fuel processing technology,* vol. 92, pp. 2320-2327, 2011.
[179] S. Suganuma and N. Katada, "Innovation of catalytic technology for upgrading of crude oil in petroleum refinery," *Fuel Processing Technology,* vol. 208, p. 106518, 2020.
[180] J. Ancheyta-Juarez, S. Maity, G. Betancourt-Rivera, G. Centeno-Nolasco, P. Rayo-Mayoral, and M. T. Gómez-Pérez, "Comparison of different Ni-Mo/alumina catalysts on hydrodemetallization of Maya crude oil," *Applied Catalysis A: General,* vol. 216, pp. 195-208, 2001.
[181] S. T. Oyama, "Novel catalysts for advanced hydroprocessing: transition metal phosphides," *Journal of catalysis,* vol. 216, pp. 343-352, 2003.
[182] E. Furimsky, "Selection of catalysts and reactors for hydroprocessing," *Applied Catalysis A: General,* vol. 171, pp. 177-206, 1998.
[183] P. E. Boahene, K. K. Soni, A. K. Dalai, and J. Adjaye, "Hydroprocessing of heavy gas oils using FeW/SBA-15 catalysts: Experimentals, optimization of metals loading, and kinetics study," *Catalysis today,* vol. 207, pp. 101-111, 2013.

[184] A. Ardiyanti, S. Khromova, R. Venderbosch, V. Yakovlev, and H. Heeres, "Catalytic hydrotreatment of fast-pyrolysis oil using non-sulfided bimetallic Ni-Cu catalysts on a δ-Al2O3 support," *Applied Catalysis B: Environmental,* vol. 117, pp. 105-117, 2012.
[185] H. Scheffe, "The simplex-centroid design for experiments with mixtures," *Journal of the Royal Statistical Society: Series B (Methodological),* vol. 25, pp. 235-251, 1963.
[186] L. Cardona, D. Arias-Madrid, F. B. Cortés, S. H. Lopera, and C. A. Franco, "Heavy oil upgrading and enhanced recovery in a steam injection process assisted by NiO-and PdO-Functionalized SiO2 nanoparticulated catalysts," *Catalysts,* vol. 8, p. 132, 2018.
[187] R. Chen, Z. Zhang, C. Feng, K. Hu, M. Li, Y. Li*, et al.*, "Application of simplex-centroid mixture design in developing and optimizing ceramic adsorbent for As (V) removal from water solution," *Microporous and Mesoporous Materials,* vol. 131, pp. 115-121, 2010.
[188] J. Sopousek, J. Vrestal, J. Pinkas, P. Broz, J. Bursik, A. Styskalik*, et al.*, "Cu–Ni nanoalloy phase diagram–Prediction and experiment," *Calphad,* vol. 45, pp. 33-39, 2014.
[189] J. Sopoušek, A. Kryštofová, M. Premović, O. Zobač, S. Polsterová, P. Brož*, et al.*, "Au-Ni nanoparticles: Phase diagram prediction, synthesis, characterization, and thermal stability," *Calphad,* vol. 58, pp. 25-33, 2017.
[190] N. Dumala, B. Mangalampalli, S. Chinde, S. I. Kumari, M. Mahoob, M. F. Rahman*, et al.*, "Genotoxicity study of nickel oxide nanoparticles in female Wistar rats after acute oral exposure," *Mutagenesis,* vol. 32, pp. 417-427, 2017.
[191] M. Ates, V. Demir, Z. Arslan, M. Camas, and F. Celik, "Toxicity of engineered nickel oxide and cobalt oxide nanoparticles to Artemia salina in seawater," *Water, Air, & Soil Pollution,* vol. 227, p. 70, 2016.
[192] A. Rostek, K. Loza, M. Heggen, and M. Epple, "X-ray powder diffraction to analyse bimetallic core–shell nanoparticles (gold and palladium; 7–8 nm)," *RSC advances,* vol. 9, pp. 26628-26636, 2019.
[193] M. S. Mazloom, A. Hemmati-Sarapardeh, M. M. Husein, H. S. Behbahani, and S. Zendehboudi, "Application of nanoparticles for asphaltenes adsorption and oxidation: A critical review of challenges and recent progress," *Fuel,* vol. 279, p. 117763, 2020.
[194] N. N. Nassar, A. Hassan, G. Luna, and P. Pereira-Almao, "Kinetics of the catalytic thermo-oxidation of asphaltenes at isothermal conditions on different metal oxide nanoparticle surfaces," *Catalysis today,* vol. 207, pp. 127-132, 2013.
[195] N. N. Marei, N. N. Nassar, G. Vitale, A. Hassan, and M. J. P. Zurita, "Effects of the size of NiO nanoparticles on the catalytic oxidation of Quinolin-65 as an asphaltene model compound," *Fuel,* vol. 207, pp. 423-437, 2017.
[196] J. Zhang, Y. Wang, R. Ma, and D. Wu, "Investigation of alumina-supported Ni and Ni-Pd catalysts by partial oxidation and steam reforming of n-octane," *Korean Journal of Chemical Engineering,* vol. 20, pp. 288-292, 2003.